FACULTY OF SCIENCE, TECHNOLOGY AND MEDICINE

PhD-FSTM 2021-086

The Faculty of Science, Technology and Medicine

Dissertation

Presented on 03/11/2021 in Luxembourg

to obtain the degree of

DOCTEUR DE L'UNIVERSITÉ DU LUXEMBOURG

EN PHYSIQUE

by

Claudius Moritz LEHR

Born on 07 September 1984 in Saarbrücken (Germany)

Analysis of flow induced texturing in complex fluids with Brillouin Rheology - a proof of concept

Dissertation defence committee

Dr. Jörg Baller, dissertation supervisor
University of Luxembourg

Dr. Roland Sanctuary
University of Luxembourg

Dr. Christian Wagner
University of Saarbrücken

Dr. Ralf Useldinger
Ceratizit Group Luxembourg

Dr. Rafael J. Jiménez Riobóo
Instituto de Ciencia de Materiales de Madrid

CML

To my family

for endless love and support.

CML

CML

Abstract

Analysis of flow induced texturing in complex fluids with Brillouin Rheology - a proof of concept

Claudius Moritz Lehr, M.Sc. (hons.)

University of Luxembourg, 2021

Supervisor: Dr. Jörg Baller

Dr. Roland Sanctuary

The aim of this work is to study the flow induced texturing of molecules (complex fluids) in a shear field. This is done by measuring phonons with photons [1] in a commercially available rotational rheometer. The optical experimental method of transferring momentum and energy between phonons and photons is generally known as Inelastic Light Scattering (ILS) [2]. Brillouin Light Scattering (BLS) [3] has a quite small energy transfer compared to Raman spectroscopy [4] but with a high performance multi-pass Vernier tandem Fabry-Perot interferometer [5] and a sophisticated optical set-up, it is possible to achieve information about the texture (like entanglement of molecules) of complex fluids inside a rheometer gap while shearing. This can be acquired for any position in the sample, in contrast to the rheological experiments were an average over a whole sample is used.

Here we successfully demonstrate an optical set-up that couples a BLS with rotational rheology in order to simultaneously measure the high-frequency longitudinal elastic modulus in a classical rheometer along with the zero-shear viscosity during the flow of complex fluids.

BLS gives the possibility for contactless determination of local elastic properties, while the designed optical set-up is introduced as boundary conditions to control temperature gradients in the sample, and the position and dimension of the scattering volume.

This method was tested for a range of temperatures, and well as for an applied shear field and different radial positions of the scattering volume in the sample using a plate-plate rheometer geometry. Measurements of a dilute polymer system suggest a homogeneous orientation of polymer molecules throughout the sample as soon as a critical shear rate has been reached at one spatial position.

CML

Table of Contents

Chapter 1: Introduction 9

Chapter 2: Experimental apparatus 11
- 2.1 Multi-pass Vernier tandem Fabry-Perot interferometry 11
  - 2.1.1 Fabry-Perot etalon 12
  - 2.1.2 Set-up of the Fabry-Perot interferometer 14
  - 2.1.3 Tandem interferometry 17
  - 2.1.4 Vibration isolation table 18
  - 2.1.5 Scanning stage 19
  - 2.1.6 Other optical elements in the system 21
  - 2.1.7 Initial operation, beam paths in the spectrometer and spectrum analysis 26
- 2.2 Rotational rheometry 31
- 2.3 Refractometry 40

Chapter 3: Material and Experimental methods 43
- 3.1 Material 43
- 3.2 Experimental methods 44
  - 3.2.1 Brillouin spectroscopy, scattering processes and scattering geometries 44
  - 3.2.2 Brillouin Rheology 49

Chapter 4: Development of a Brillouin Rheology Set-up 55
  - 4.0.1 First experimental approach of BR with 80 mm focusing optics 57
  - 4.0.2 A study with a 100 mm focusing optics 59
    - 4.0.2.1 Positioning of the scattering volume 61
  - 4.0.3 Rheological investigations of the PVP 2.5 mass percent PEG sample 63
  - 4.0.4 Final investigations with 60 mm focusing optics 66
- 4.1 First results from Brillouin Rheology using backscattering 71
  - 4.1.1 Shear rate dependency 71
  - 4.1.2 A study of shear rate and radial position dependency 75
  - 4.1.3 Comparison of Brillouin shifts over increased shear rate at different radial positions 81
  - 4.1.4 Brillouin Rheology and relaxation effects 83

Chapter 5: Brillouin Rheology - the proof of concept ... 89

5.0.1 Influence of plate diameter, material and surface to BR-spectrum and rheological results ... 92
5.0.2 Real temperature in the sample, its extrapolation and control ... 96
5.0.3 Dimension of the scattering volume, identification of the position of the scattering volume in x-y-z plane and influence of laser power to signal strength ... 100
5.0.4 Brillouin shifts for temperature change and applied shear field ... 107
5.0.5 Brillouin Rheology and its shear field sensitivity ... 109
5.0.6 Comparison of different radial positions of the scattering volume ... 110

Chapter 6: Conclusion and Outlook ... 113

Appendix ... 117

The Material 5CB ... 117
The $RI\Theta A$ scattering Set-up inside the rheometer ... 118
    Influence of applied laser power to the measurements ... 122
Rheology of 5CB for different gaps sizes ... 124
360° rotational Brillouin Rheology of 5CB ... 137

References ... 141

It’s about sound and vision.

- *Nada Brahma* -

- A Mazzalode -

CML

SYMBOLS AND VARIABLES

M'	Longitudinal stiffness modulus
n , n_1 , n_2	Refractive indices
d_{Et}	Thickness of FP etalon, mirror separation distance
α_{Et}	Angle of incidence (etalon)
m, k	Integer values
λ	Wavelength of light, middle wavelength
Δf_{FSR}	Free spectral range
$\Delta\lambda$	Linewidth wavelength
Δf	Linewidth frequency
c	Speed of light
δf	Spectral width
F	Finesse
R	Reflectance (of a surface)
$\lambda/(\Delta\lambda)$	Resolving power
Δ	Constructive interference maximum
α, β	Angle of incidence for FPI
I	Intensity (of light)
m_I	Orders of interference
N	Numbers of interfering rays
$\delta d_1, \delta d_2$	Increment wavelength scan distances
Θ_{FP}	Angle between to FP doublets
xc	Brillouin frequency shift value (from Origin fit)
L_0	Initial length (of a rectangular bar)
L	Elongated length
δL	Increased length
ε_c	Cauchy strain
ε_h	Hencky strain
γ_A	Deformation angle of shear
σ_{ij}	Shear, tensile or compressive stress
F_H	Applied force (Hooke's law)
k_H	Constant (e.g. spring constant)
x_H	Change in length (Hooke's law)
G	Shear modulus
γ	Shear strain
R_{0H}	Initial radius (Hookean material)
A	Area (of a cylindrical shaped form)
h_0	Initial height
δh	Change in height
E_Y	Modulus of elasticity, Young's modulus
ν_Y	Poisson's ratio
h_{PP}	Height of a gap (between two plates)
u_{PP}	Constant velocity (of one of two plates)

$\delta L_{PP}/\delta t$	Incremental change of position for a small period of time
$\dot{\gamma}$	Shear rate
τ	Shear stress
F_S	Shear force
A_S	Shear area
v_S	Velocity
H_S	Gap size, sample height
R_S	Radius of sample and rheological geometry
ω_S	Rotational speed, angular velocity
η	Shear viscosity
M	Torque (rheometer)
R	Radial position (between plate-plate geometry)
ν_k	Kinematic viscosity
n_{ROT}	Rotational speed (preset value)
C_{ij}	Stiffness tensor
ε	Strain tensor
ρ	Density
$\hat{s}$	Polarization
E_{Ph}	Energy of a photon
h_P	Planck’s constant
ν_P	Frequency of a photon
$h\nu_S$, $h\nu_A$	Energy of an anti-/stokes photon
$\vec{q}^{\pm}$	Wave vector (phonon)
$\Omega^{\pm}$	Angular frequency (phonon)
$\hbar$	Reduced Planck’s constant
$\omega_i^{\pm}$	Angular frequency (incoming light)
$\vec{k}_i^{\pm}$	Wave vector (incoming light)
θ_i	Incidence angle of scattering process
f_B	Brillouin shift frequency
v_B	Hyper sound velocity
Θ_s	Scattering angle
m_{lf}	Slope of linear fit
b_{lf}	Interception of y-axis (linear fit)
ω_0	Radius of focus spot
θ_0	Angle of beams’ edges to focus
k_{bq}	Beam quality factor (of laser)
ω_{ObjL}	Beam radius
f_{ObjL}	Focal length (objective lens)
$z_R = 2 * z_0$	Rayleigh length (for Gaussian beam)
r	Beam radius (before widening)
α_i	Angle of incidence (focusing optics)
a_i	Distance to middle ray (of a beam)
f_i	Focal distance
β_i , γ_i	Angles of refraction (different media)
P	Induced laser power into the sample

ABBREVIATIONS

ILS	Inelastic Light Scattering
BLS	Brillouin Light Scattering
PIV	Particle Image Velocimetry
PM	Polarizing Microscopy
DLS	Dynamic Light Scattering
POM	Polarized Optical Microscopy
SALS	Small Angle Light Scattering
SAXS	Small Angle X-ray Scattering
SANS	Small Angle Neutron Scattering
FP	Fabry-Perot
TTL	Transistor to Transistor Logic
FSR	Free Spectral Range
FPI	Pabry-Perot Interferometer
APD	Avalanche Photo Diode
SLM	Spatial Light Modulator
OPSL	Optically Pumped Semiconductor Laser
DHO	Damped Harmonic Oscillator
CSR	Controlled Shear Rate (test)
CSS	Controlled Shear Stress (test)
CMOS	Complementary Metal-Oxide-Semiconductor
CCD	Charged-Coupled Device
LED	Light-Emitting Diode
TA, LA	Transversal-, Longitudinal Acoustic (mode)
SNR	Signal to Noise Ratio
BS	Brillouin Spectroscopy
PVP	Polyvinylpyrrolidone
PEG	Polyethylene glycol
PP	Plate-Plate geometry
GP	Glass-Plate geometry
SIPLI	Shear-Induced Polarized Light Imaging
5CB	4-pentyl-4`cyanobiphenyl

Chapter 1: Introduction

When complex fluids are subject to shear flow, many different phenomena can occur, such as orientation of molecules or fillers, nucleation of crystals and shear banding. There exist optical techniques like Particle Image Velocimetry (PIV), Polarizing Microscopy (PM) or Dynamic Light Scattering (DLS) which give access to structural or dynamic information [6, 7]. It would be desirable to have a technique that can deliver information about mechanical properties on a microscopic scale during shearing of complex fluids. BLS is such a contactless, non-destructive technique to measure elastic moduli at high frequencies using an optical spectrometer, which can analyze the scattering of light by thermal phonons. The propagation velocity of thermally activated longitudinal or transversal sound waves delivers direct information about the effective spring constants for these types of propagating modes.

Obtaining information about interfacial effects between sample and sample stage or around the trim belly to air in common rotational rheology is quite hard. Knowing how molecules behave inside the sample stage while rotating is even more difficult to predict. There are models, which explain and predict outcomes, like shear thinning and thickening, or thixotropic behavior while shearing a sample with a rotational rheometer. To get a deeper insight into the effects of texturing/structuring of molecules with a *xyz* spatial resolution inside the sample is a goal of this work. A rotational rheometer measures mechanical properties averaged over the whole sample volume (inside the rheometer gap). This work aims at giving information about mechanic properties and orientation of the molecules with-in micrometer resolution.

As formulated by Smoluchowski in 1908 [8] and Einstein in 1910 [9], the scattering of light can be described by the effect of fluctuations in the local dielectric tensor. That fluctuations in dielectric tensor from thermal acoustic phonons result in light scattering effects was predicted by Brillouin in 1922 [10] and Madel’shtam in 1926 [11]. Furthermore, there should be a shift in frequency of the scattered light as the phonons are moving. This effect was then observed by Gross in quartz [12] and for several liquids [13] in 1930. Leontovich was first to calculate the spectrum due to scattering by damped phonons in 1931 [14] and 1936 [15]. Some experimental progress was made in the 50’s by Fabelinski [16] with Pesin [17] and Molachnov [18]. Brillouin Light Scattering (BLS) became a standard technique in experimental physics with the invention and use of lasers. In 1967 [19] Peticolas, Stoicheff and Stegeman first applied BLS to polymeric systems [20].

Using different experimental set-ups, it is, in principle, possible to derive the complete elastic stiffness tensor with a spatial resolution limited only by the optical set-up employed [21]. To investigate the influence of shear flow on complex fluids, rotational rheology is the state of the art technology [22]. It is a very common technique to macroscopically measure elastic susceptibilities, such as complex viscosities, shear moduli and study nonlinear behavior, such as shear thinning in complex fluids [23, 24]. Rotational rheology delivers indirect information about shear-induced alignment on different length scales (from fillers to molecular order) or shear induced crystallization. For more detailed studies of the influence of shearing on complex fluids, rheology has been coupled with Polarized Optical Microscopy (POM) and different small-angle scattering technologies (e.g. Small Angle Light Scattering (SALS), Small Angle X-ray Scattering (SAXS) and Small Angle Neutron Scattering (SANS)) [7, 25-33]. Some of these techniques are able to deliver spatially resolved information.

The main objective of this work is to develop an experimental set-up which allows the use of an optical method to locally record elastic moduli at high frequencies during the shear flow of complex fluids. A technique is presented to apply BLS inside the gap of a rotational rheometer. The longitudinal stiffness tensor, which is related [34, 35] to Young's modulus, is determined by BLS and compared to the zero-shear viscosity simultaneously measured by classical rotational rheology. The set-up described here in detail is limited to one single scattering geometry thus only delivering one component, the longitudinal modulus (M'), of the elastic stiffness tensor. This study aims to be the start for the development of more sophisticated set-ups allowing the recording of the complete stiffness tensor at hypersonic frequencies during the shearing of complex fluids.

Chapter 2: Experimental apparatus

Systems, set-ups and related equipment

This chapter introduces the main apparatus that is used in this work, namely the tandem Fabry-Perot spectrometer (from JRS [36]), the rotational rheometer MCR302 (from Anton Paar [37]) and the automatic refractometer (Abbemat HP/WR/HT/MW from Anton Paar [38]). The latter is used to gain information of the material parameters of the sample. The spectrometer is explained in more detail as it is the most crucial instrument for this study. Further, the optical set-up inside the spectrometer, the one to get it started, and the experimental beam path is introduced.

2.1 Multi-pass Vernier tandem Fabry-Perot interferometry

The TFP2-HC interferometer (from JRS, now Table stable, Figure 1) was developed by John Sandercock in the 1980`s [36, 39-44]. A tunable Fabry-Perot (FP, also called etalon) doublet is used as a filter and combined with a scanning stage and a shutter unit, so very fast scanning of a small bandwidth of frequency (or wavelength) can be achieved and very small shifts in a reference wavelength detected.

Figure 1: Picture of the tandem Fabry-Perot spectrometer (1) with corresponding electronics. (2) Control unit of the spectrometer, (3) Energy supply of the photon-counter, (4) control unit of the isolation stage, (5) mirror separation distance control unit and (6) the temperature controller for additional temperature measurements.

The principle is that of a FP interferometer that is set onto a vibration isolation table and a scanning stage, which is able to change the separation distance of the FP mirrors quickly and precisely. This combination allows a scan of narrow regimes of frequencies. In this work, an avalanche photo diode is used as a photon counter.

The block diagram (Figure 2) shows the main units and signal transfer of the spectrometer system. The spectrometer has an entrance aperture with a shutter and beam splitter included, so the main beam from the experiment as well as the reference beam can enter simultaneously.

The photon counter sends the Transistor-to-Transistor Logic (TTL) pulses to the control unit. The Ghost software (also from JRS) installed on a personal computer pictures the collected spectra on the PC-screen.

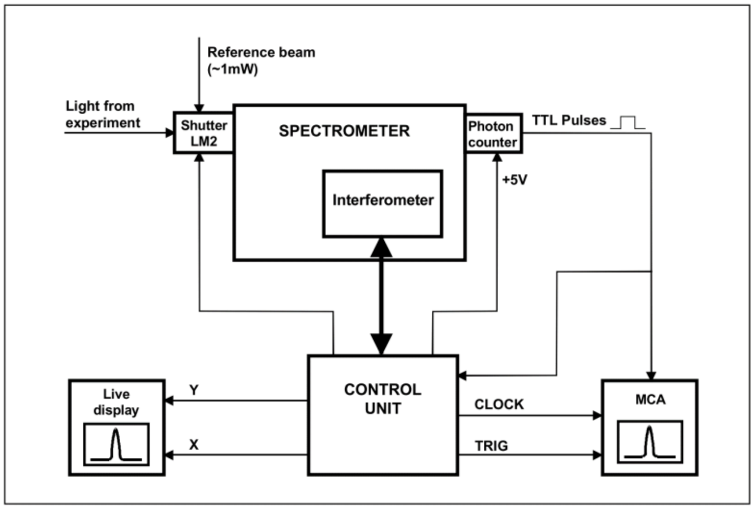

Figure 2: Block diagram of the TFP spectrometer with corresponding electronics for control and data evaluation [36].

In the following, crucial parts for the function of the interferometer are introduced and some techniques and theoretical knowledge presented.

2.1.1 Fabry-Perot etalon

The set-up of two parallel, partly transmitting mirrors, which e.g. are put onto a plan-parallel glass plate (with refractive index *n*) is called a Fabry-Perot etalon. To select distinct frequencies, the etalon is usually placed oblique to the optical axis (Figure 3).

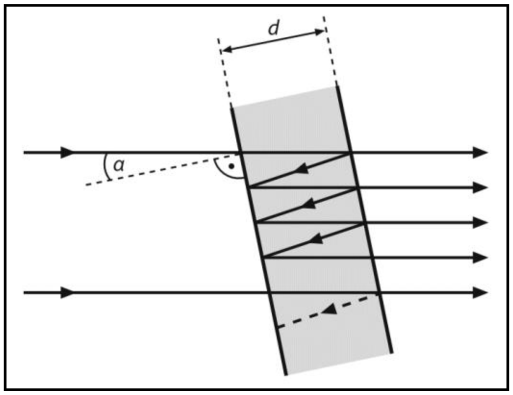

Figure 3: Illustration of a Fabry-Perot etalon with a thickness d_{Et} and a tilt in angle of incidence α_{Et} [45, 46].

The incoming laser beam (or light wave) leads to multiple reflections in between the mirror surfaces. If these reflected wave parts are in phase to each other, there is constructive interference, which amplifies this certain wavelength over time (multiple reflections), so the etalon will be only transparent for this selected wavelength. The constructive interference condition will appear for following circumstances (Eq. (1)), where m is an integer and λ the wavelength.

$$2\mathrm{d}_{\mathrm{Et}}\sqrt{\mathrm{n}^2-\sin^2(\alpha_{\mathrm{Et}})}=\mathrm{m}\lambda \tag{1}$$

So, for each wavelength, there is an angle of maximum transmission. The angular dispersion for n=1 produces following relation (Eq. (2)):

$$\frac{\mathrm{d}\alpha_{\mathrm{Et}}}{\mathrm{d}\lambda}=\frac{1}{\lambda\cdot\tan(\alpha_{\mathrm{Et}})} \tag{2}$$

Compared to other frequency selective optical instruments likes prisms or diffraction gratings, the Fabry-Perot etalon, for a small tilt angle α_{Et}, gives significantly higher values for the angular dispersion, so it has a higher quality in the task of selecting frequencies. Tuning the etalon can be handled diversely by tilting, changing of the mirror separation distance, or with the change of the refractive index n of the material in between the mirrors. In case of a fixed value for the mirror separation distance d_{Et}, the refractive index n and the tilt angle α_{Et}, the etalon will transmit several wavelengths (or spectral lines). This frequency distance or separation of these lines is called Free-Spectral-Range (FSR) and is denoted for α_{Et}=0 and n=1, being c the speed of light, as follows (Eq. (3)).

$$\Delta\mathrm{f}_{\mathrm{FSR}}=\frac{\mathrm{c}}{2\mathrm{nd}} \tag{3}$$

This also corresponds to the spacing between two adjacent longitudinal modes of a laser resonator [45]. Nevertheless, to get proper frequency selection of just one spectral line, the frequency bandwidth of the incoming light has to be smaller than the free spectral range Δf_{FSR}. Often, therefore, other etalons are installed to select the incoming bandwidth. For a plane wave and arbitrarily large diameter, the etalon is transparent in a linewidth wavelength $\Delta\lambda$ or frequency Δf whereas the middle wavelength $\boldsymbol{\lambda}$ is given by $\mathrm{c}=\lambda\cdot\mathrm{f}$. It is required that the so-called spectral width δf of the transmission peak of the etalon (Eq. (4)) is smaller than the laser mode spacing.

$$\delta\mathrm{f}=\frac{\Delta\lambda}{\lambda}=\frac{\Delta\mathrm{f}}{\mathrm{f}}=\frac{\Delta\mathrm{f}_{\mathrm{FSR}}}{\mathrm{F}} \tag{4}$$

The finesse F of the etalon (Eq. (5)) is a parameter that is defined by the reflectance R of the mirror surfaces.

$$\mathrm{F}=\frac{\pi\sqrt{\mathrm{R}}}{1-\mathrm{R}} \tag{5}$$

As an example for a reflectance of 10% to 97% it will give an F of 11 to 100. The resolving capacity $\frac{\lambda}{\Delta\lambda}$ for a large mirror separation distance d and a reflectivity R of the mirrors is much higher compared to a prism or diffraction grating. Nevertheless, the real resolving power or capacity can be much smaller, as there are divergent light waves and limiting apertures. With the variation of the thickness, one can select different linewidths $\Delta\lambda$ or Δf.

2.1.2 Set-up of the Fabry-Perot interferometer

The Fabry-Perot Interferometer (FPI) used here consists of two parallel, partly transmitting plates with a separation distance d usually in the range of mm to cm. As described previously, the incoming light is reflected multiple times and transmitted as parts of the wavelength spectrum. If the transmitted parts are in phase with each other (multiple integers of the wavelength λ) a constructive interference maximum is abound (Eq. (6)):

$$\Delta = 2d\sqrt{n^2 - \sin^2(\alpha)} = 2nd\cos(\beta) = k\lambda \qquad (6)$$

The parameter k also stands for an integer. The angle of the incoming beam (measured outside the interferometer) is α, β is the angle in between the mirrors (measured parallel the optical axis) and the refractive index in between the mirrors is denoted as n. Having a fixed separation distance d, several wavelengths are transmitted as introduced before. To acquire a spectrum, usually the light is sent a little divergent ($\alpha \neq 0$) through the doublet (Figure 4), else one would have laser resonator conditions.

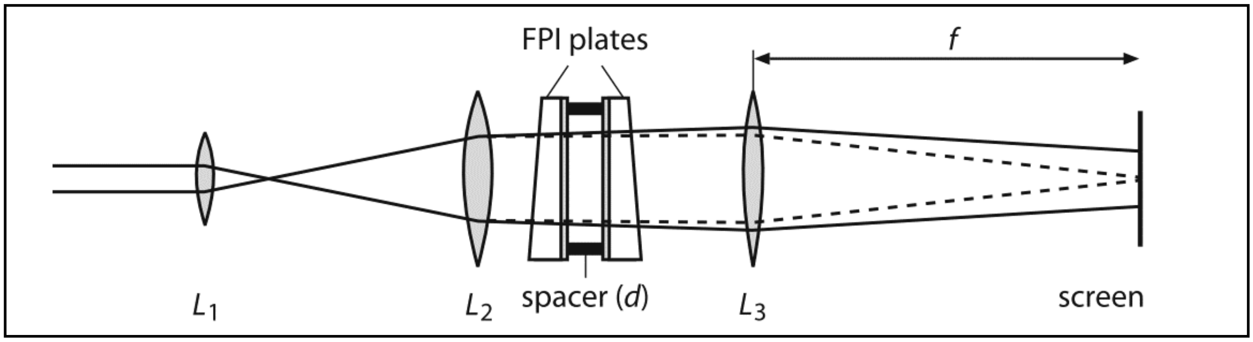

Figure 4: Illustration of a Fabry-Perot interferometer [45]. L1 is a positive lens for diverging the beam. L2 collimates the beam and sends it enlarged through the doublet, which has reflecting surfaces inside, with a separation distance d. L3 is imaging the fringe pattern onto a screen. The dotted and solid lines indicate different ring patterns.

The lenses L1 and L2 are used to set the divergence [47], in the middle of the two Fabry-Perot plates (etalon) with highly reflecting surfaces at their inner sides, having a separation distance d. L3 is used for focusing or imaging the light coming out of the Fabry-Perot doublet on a screen. Different angles of the light give different radii of rings (fringe patterns) that are imaged (e.g. on a screen) and the wavelength or frequency can be calculated back from thei diameters of those.

The solid line and dotted line in Figure 4 indicate diffraction rings of different orders that are illustrated in Figure 5.

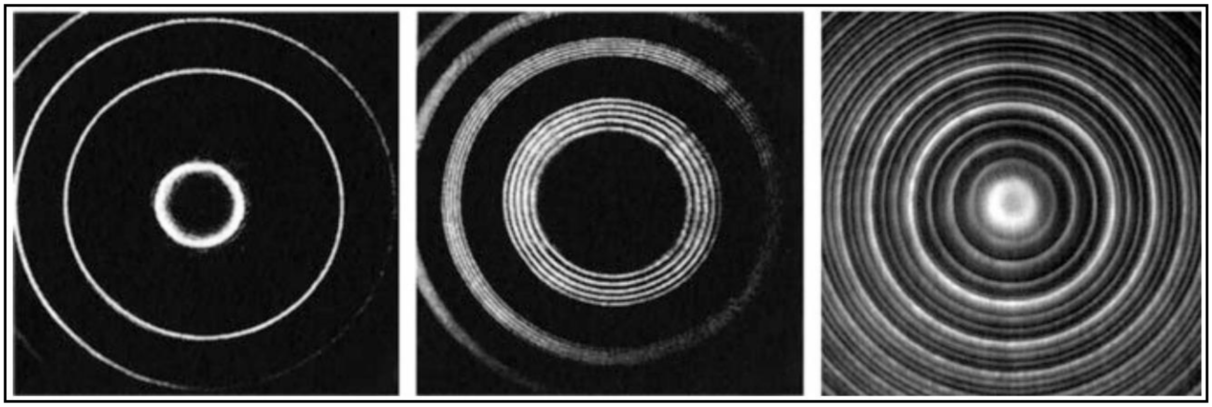

Figure 5: Interference ring patterns of a laser beam produced by a Fabry-Perot interferometer. Left: single mode, middle: five modes, right: the spectral bandwidth is larger than the free spectral range of the Fabry-Perot interferometer [45, 46].

Figure 5 represents three examples, left, the image on the screen while lasing onto the Fabry-Perot interferometer with one mode. The middle picture shows the same for five modes, and to the right, one can see that there are many rings. This is the case for having a spectral bandwidth of the laser that is wider than the spectral range of the Fabry-Perot interferometer.

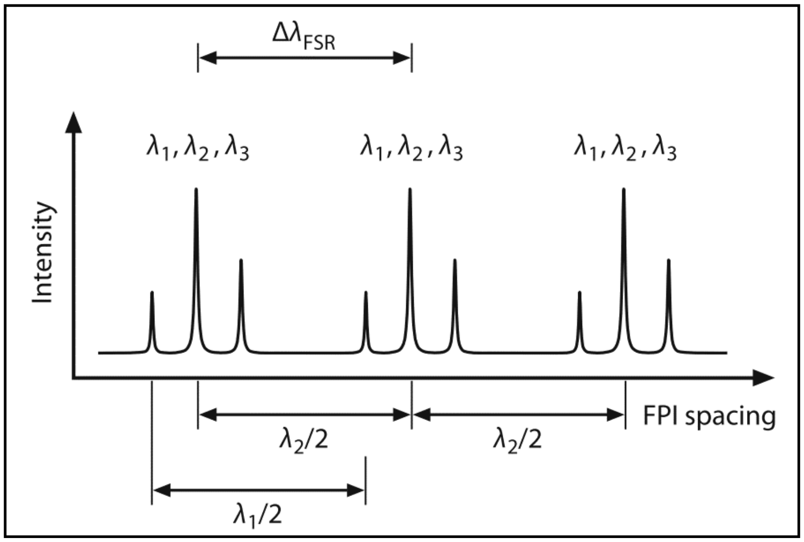

Figure 6: Illustration of an interference pattern produced by a scanning Fabry-Perot interferometer. The spacing of the FPI is varied so different wavelengths are transmitted. The free-spectral range is indicated.

The spectrum of the incoming radiation gives the intensity I of the spectrum as a function of the change of the separation distance d (illustrated in Figure 6).

As mentioned before, in case the mirror spacing d is equal to any integer multiple of the wavelength a high intensity I is following due to the constructive interference. Different wavelengths will have their maxima at other distances d. Out of this difference of the plate separation distance, the difference of wavelength or frequency can be calculated.

To summarize, the Fabry-Perot interferometer can get a very high resolution power of up to 10^8.

To give an overview and estimation about the common interferometers, Table 1 gives a picture of the very high resolution power [48] of the FPI.

Table 1: Overview of resolution power for different spectrometers at a wavelength of about 500 nm [46].

Spectrometer	**Parameters**	**Orders m_I**	**Number N of interfering rays**	**Resolution $\frac{\lambda}{\Delta\lambda}$**
Prism	$\frac{dn}{d\lambda} = 1730\ cm^2$, Basis t=10 cm	-	-	17.300
Grating	16.5 cm, 600 lines/mm	3	100.000	300.000
Fabry-Perot	R95 %, d=1 cm	40.000	60	2.400.000
	R95 %, d=10 cm	400.000	60	24.000.000

Further readings regarding these topics:

J.M. Vaughan, *The Fabry-Perot Interferometer* (Institute of Physics Publishing, 1989).

E.G. Loewen, E.Popov, *Diffraction Gratings and Applications* (Marcel Dekker, 1997).

T.W. Hänsch, *Passion for precision* (Nobel lecture). ChemPhysChem 7, 1170 (2006).

R. Paschotta, *Encyclopedia of Laser Physics and Technology* (Wiley-VCH, 2008).

W. Demtröder, *Laser Spectroscopy* (Springer 2008).

2.1.3 Tandem interferometry

To increase the free-spectral range (FSR) at a fixed resolution by using a second Fabry-Perot (FP) doublet in series ,a Vernier system [5], [49] is used so the mirror spacing of the second FP doublet is close to the separation distance of the first one. Having the mirror separation distances d_1 and d_2, the transmitted wavelengths from the FP doublets must simultaneously satisfy the following relations (Eq. (7)), namely being half of an integer of the wavelength:

$$\mathrm{d}_1 = \frac{1}{2}\mathrm{m}\cdot\lambda \qquad \mathrm{d}_2 = \frac{1}{2}\mathrm{n}\cdot\lambda \tag{7}$$

If the spacing is set so that a certain wavelength is transmitted through both FP doublets, Figure 7 gives an example of the transmission signal of both FP´s and the resulting tandem mode signal.

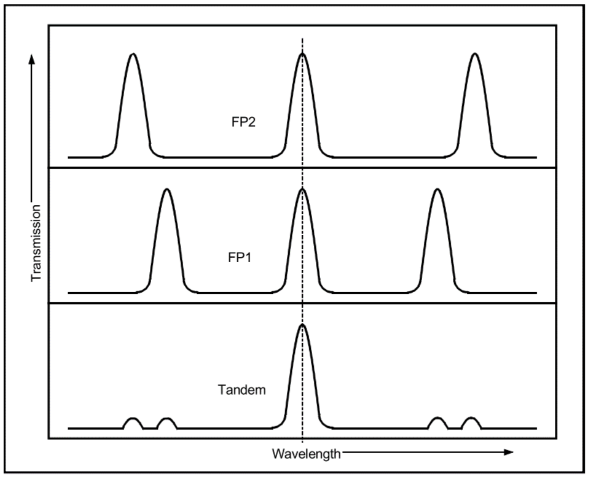

Figure 7: Illustration of transmission spectra of the two FP doublets, whose outer peaks are shifted to each other. The tandem signal, which is a superposition of both, shows the main middle peak and two side peaks (ghosts) resulting from the misalignment of the FP doublets [36].

Due to the fact, that the main transmission peak overlaps and the adjacent ones do not coincide, it results in small "ghosts" which appear at the tandem mode signal due to the interfering transmission peaks. Having this tandem mode combination, the resolution remains similar while the FSR is increased by a considerable factor compared to a single interferometer. 'For minimizing the "ghosts" one can choose the following relation (Eq. (8)) for the finesse F'[36]:

$$\mathrm{F} > \frac{\mathrm{d}_1}{(\mathrm{d}_1 - \mathrm{d}_2)} \tag{8}$$

To give an estimate or a good value for the relation d_2/d_1, it practically would be 0.95. The application of this tandem interferometer technique requires the scanning of the two interferometers simultaneously (change of separation distances d_1 and d_2), thus the increment wavelength scan δd_1 and δd_2 must satisfy the following relation (Eq. (9)), where the magnitudes of δd_1 and δd_1 are usually on the order of micrometers.

$$\frac{\delta d_1}{\delta d_2} = \frac{d_1}{d_2} \tag{9}$$

The principle of a tandem scan allows now to obtain both, statically[1] and dynamically[2] stable synchronization. This is illustrated in Figure 8.

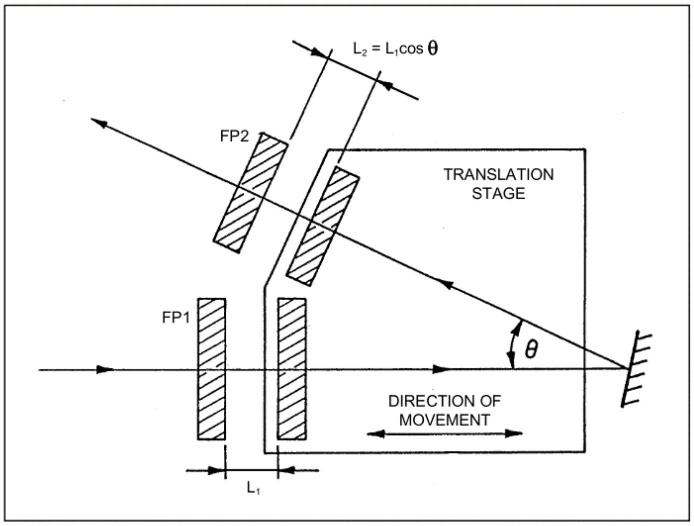

Figure 8: Schematic representation of two FP doublets in series, sitting on a translation scanning stage and being oriented in an angle Θ_{FP} at each other [36].

The FP1 doublet is set in the direction of the translation stage movement. One mirror is fixed on the translation stage, while the other is set in a separate angular orientation device. The FP2 is oriented with an angle Θ_{FP} to the scan direction. In close proximity to the mirror of FP1, one mirror is mounted on the translation stage and a second one on an angular orientation device to apply small translations for adjustment.

2.1.4 Vibration isolation table

To be able to change the distance of the mirror separation in a very short range, quickly and precisely, and further mitigate external influences like temperature and vibration, the optical system is dynamically isolated from vibrations.

A change in mirror spacing of about 25 Å has to be accomplished to scan a Fabry-Perot interferometer for a single transmission peak. An external influence just needs to distort the separations of the mirrors for a few angstroms to distort the spectrum, so the interferometer is actively isolated. Figure 9 shows a sketch of the tandem FPI mounted on two dynamic modulation mounts (AVI-35 LPR elements, actively isolation system). A dynamic feedback control is used

---

[1] Static synchronization means that the spacing of the two interferometers never depart from their corrected relative values more than 20 Å.

[2] Dynamic synchronization means that the relative spacing maintains over scans of several µm.

for the dynamic isolation system. The directional position stability is very strong as the system is stiff, compact and has comparable less drift over large movements. Only the Fabry-Perot etalons are isolated as the other optics are not extremely sensitive to vibration or sound.

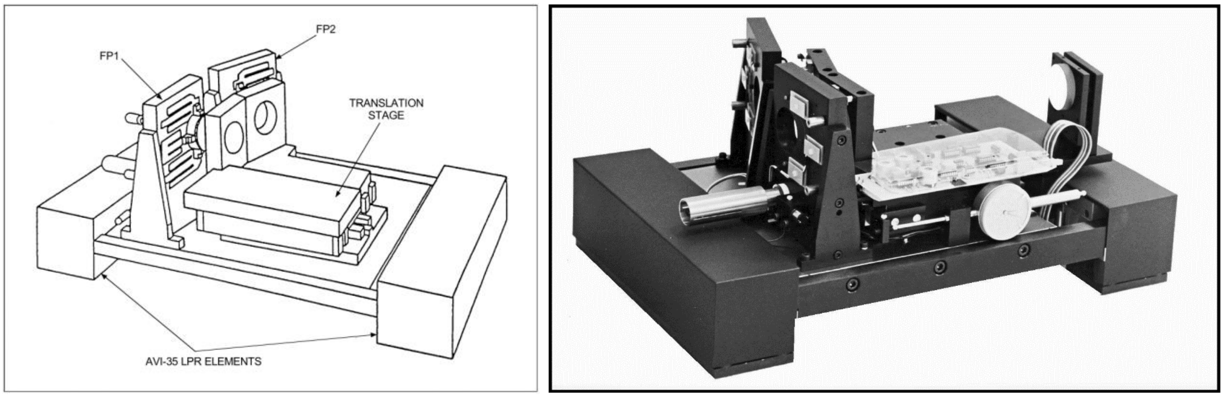

Figure 9: Left drawing; right picture of the vibration isolation table [36, 50] showing the FP1 and FP2 and the translation stage.

2.1.5 Scanning stage

The scanning stage [36, 51, 52] is used to change the mirror separation. Further, by scanning, the interferometer can reach very high contrast and resolution as previously described. Figure 10 shows a schema of the scanning stage.

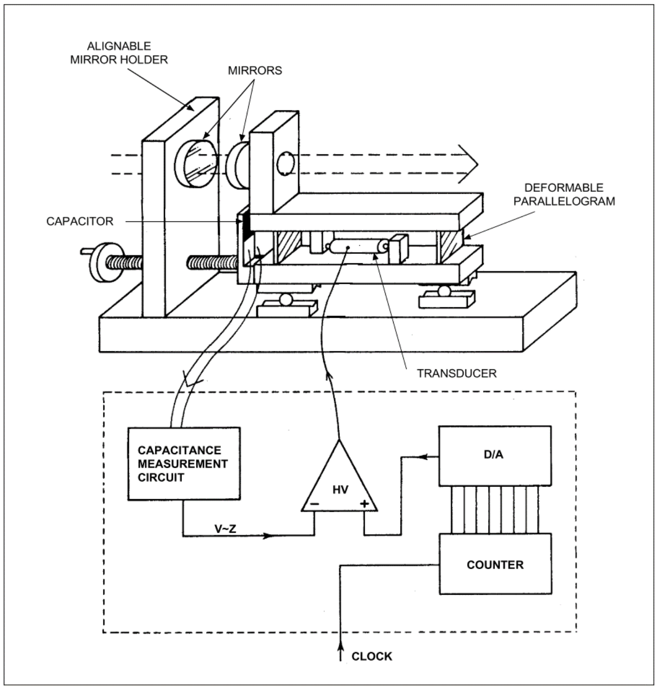

Figure 10: Simplified schema of the scanning stage [36], showing the mirrors as the most crucial parts of the system, which is explained in further detail in the text.

The mirrors are fixed on compound translation stages (for small displacements), attached to the cross roller translation stage (for large displacements) and they can be adjusted with a micrometer screw for coarse setting. While scanning the interferometer, a piezoelectric transducer acts on the deformable parallelogram (compound translation stage). The separation of the mirrors is sensed using a capacitive displacement transducer. This is used in a feedback loop to control the piezoelectric scanning transducer. Two conditions have to be fulfilled by the compound translation stage: on the one hand, during a scan (< 3 µm), the mirrors have to kept parallel, and after a large displacement (mm), the mirror alignment changes a little as well, so a small correction with the fine adjustment (piezoelectric alignment transducers) is sufficient. This high scan movement accuracy is achieved using a deformable parallelogram that is capable of movements of 100 µm and more, without a tilt, so a 3 µm scan can be achieved easily. The actuator for scanning is a piezoelectric crystal acting between the upper rolling stage plate and the deformable parallelograms. On a crossed roller translation stage sits the deformable parallelogram stage. As they are sufficient for achieving the required suitably tilt-free movement over a distance of several cm, precision ground steel flats are used as runners.

The mirror separation is measured by a capacitive displacement transducer whose output is accurately proportional to the distance between the capacitor plates. A scan can be achieved by comparing the scan voltage with the transducer output voltage, giving a correct voltage to drive the piezoelectric scanning transducer. The feedback scanning system has two goals, the linearity of the displacement transducer determines the linearity of the scan and it is independent of nonlinearities in the scanning transducer. Nevertheless, the most crucial parts regarding the main importance of thermal expansion lies in between the short distances between the mirror holders and the capacitor with the micrometer screw. Any thermal expansion in other parts of the interferometer is entirely compensated by the feedback system [36].

2.1.6 Other optical elements in the system

For a better understanding of the technique, polarization and polarizing optical elements are briefly introduced and literature references given. The optics inside the TFP2-HC spectrometer are presented in Figure 19 and Figure 20 and a drawing of the use of retardation plates (and prisms) in Figure 14. The beam steering with quarter-wave optics through the Fabry-Perot doublets for six passes is introduced and illustrated. Further, the detector and the laser light source for utilization of the spectrometer are presented.

The calculation of propagation of light waves and the corresponding polarization (Fresnel equations) can be achieved by using the Stokes parameters, the Jones matrix and Mueller matrix calculus. This is beyond the scope of this work, but detailed explanations can be found in works by [53, 54].

For the manipulation and use of the polarization, there are a variety of optical elements, but this work will look at a single element, a quarter-wave plate / phase retardation plate, which will be briefly described [55].

A retardation plate is a material that is transparent for light, but, due to its structure, has the property to lead to dispersion for the ordinary and extraordinary axis, as they just can travel with different speeds through it, because of the differing refractive indices along each of the directions. One ray (or orientation of the E-field) is retarded relative to the other, as their path difference can be described by $n\lambda$. A quarter-wave plate has then a retardance for one of the rays of $\frac{\lambda}{4}$. Figure 11 illustrates the ordinary and extraordinary ray axis. The faster moving ray (or its E-field vector) vibrates in the fast axis direction.

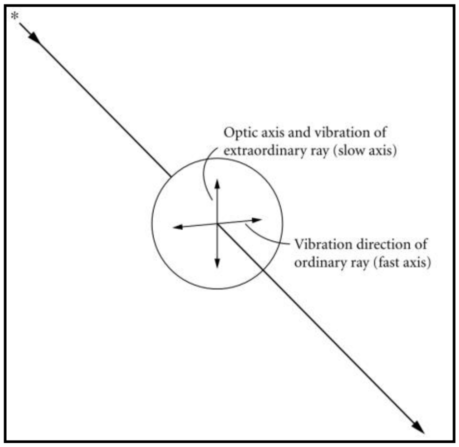

Figure 11: Light hits the surface of a retardation plate. The ordinary and extraordinary directions of vibrations are pictured [55].

To give an impression of the function and effect of the quarter-wave plate, Figure 12 shows coherent linear polarized light in certain orientations passing through a quarter-wave plate and the resulting polarization.

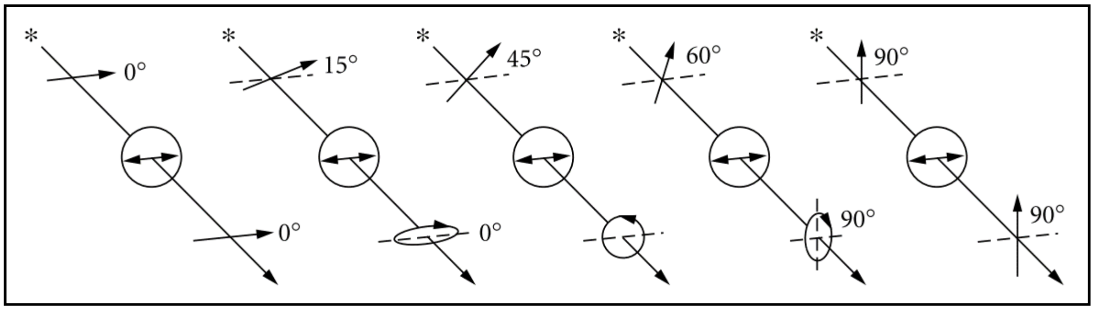

Figure 12: Illustration of the state of polarization after a light beam passes a quarter-wave plate. The incoming linearly polarized light is tilted in a certain angle before passing the plate that is oriented with the fast axis being horizontally [55].

Choosing one by example, the beam with a 45° tilted linear polarization, passing the quarter wave plate results in circular polarization (Figure 12).

The tandem Fabry-Perot interferometer needs vertically linearly, coherent, polarized light to enter, as the internal optical system is newly designed with polarization elements to steer the beam through the spectrometer and to decrease noise [50, 52, 56]. Entering the spectrometer through its aperture and being lead through the Fabry-Perot etalons, the linear polarized light enters a 90° prism. This acts as a quarter-wave plate or a Fresnel rhomb [54].

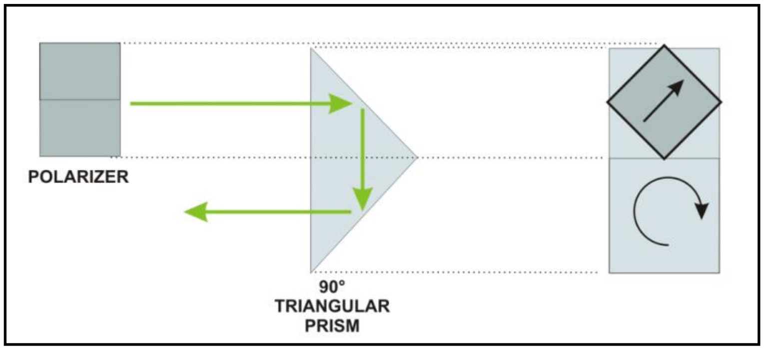

Figure 13: Illustration of the beam steering inside the TFP2-HC with 90° triangular prisms acting as polarization changer. Linear polarized light is entering the prism, which then is converted to circular polarized light and vice versa [36].

Figure 13 illustrates linearly polarized light coming from a polarizer, entering a 90° prism, aligned 45° tilted to the prism axis. This is due to the vertically linear polarization the light entering the spectrometer must have. The outgoing light beam is circular polarized and vice versa, so cross-talk and noise is reduced drastically.

Figure 14 is a schema of the interior optics of the TFP2-HC spectrometer from JRS [36]. The light entering has to be vertically polarized. After the light passes the aperture and shutter unit (explained in the latter), the light is lead over mirror M1 to mirror M2, where the polarization is converted to circular polarization. The light passes FP1 the first time and gets reflected by the first 90° prism, where the polarization is changed to linear polarization. As a result, passing the linear polarizer, it is not attenuated. A polarizer just lets one certain polarization pass, in this case, the linear polarized light in a certain orientation. After passing the FP1 the second time and another polarizer, the beam gets reflected and converted to circular polarization by the second 90° prism and passes the FP1 the third and last time. Further, the light goes through a spatial filter, then through another 90° prism and starts its 3 passes through the second FP doublet, till lastly, it is sent through an interference filter and is detected by the photon counter, finally.

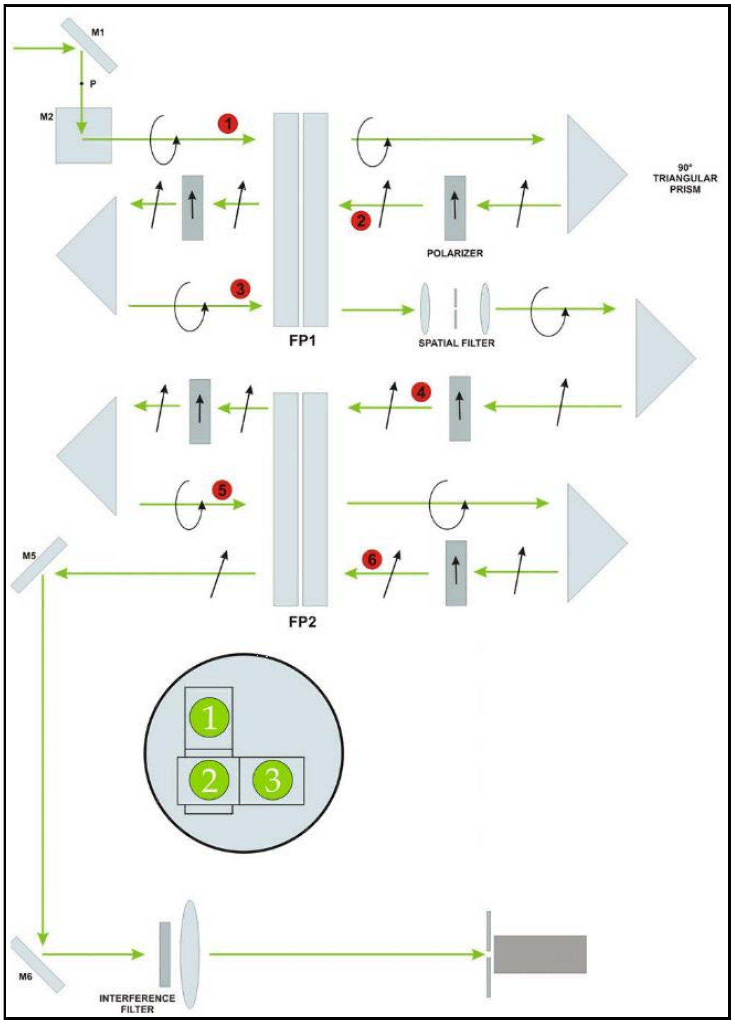

Figure 14: Schematics of the beam steering through the spectrometer with the use of 90° triangular prisms for switching the polarization in between the passes, which leads to less cross-talk and noise while measurements. 1, 2, 3 denotes the position of the beam spots on the FP`s [36]. The numbers in the red circles indicate the passes of the light through the FPI. M stands for mirror. The arrows indicate linear polarization, as the circles circular polarization. For a more detailed description see text above.

The **photon-counting module** SPCM-AQ from EG&G (nowadays Perkin Elmer) is a solid-state detector with a quantum efficiency of 60%-70% at a wavelength of 500nm (Figure 15).

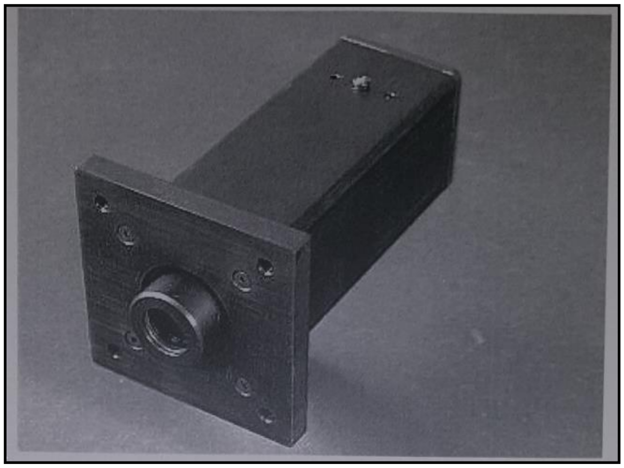

Figure 15: Picture of the photon counting module (avalanche photo diode) SPCM-AQ from EG.

Due to the high efficiency, the Avalanche Photo Diode (APD) allows very fast measurements compared to a photomultiplier tube. The output brings TTL pulses for further electronic evaluation of the detected signals. The lens of the system has a diameter of 18 mm (f/1.5 fully adjustable) with a simple shutter. The active area of the SPCM-PQ module is 200 µm in diameter and a dark count rate is selected for 25 cts/sec or better (typically 20 cts/sec). However this rate seems comparable high (as photomultiplier have about 1 cts/sec dark count), due to the high quantum efficiency, the "signal to noise ratio for all photon fluxes is considerably better than obtained with other photomultiplier tubes" explains the manufacturer of the spectrometer (JRS). Further, it is warned, that the detector can easily be damaged by excess to high intensities. Running it for periods of minutes at near maximum count rate of around 10 million counts/sec should be avoided as well.

The **laser light source** is a Verdi G2 [57, 58] spatial light modulated (SLM) Optically Pumped Semiconductor Laser (OPSL [59]) from Coherent, giving a vertically, linear polarized light beam of 532 nm wavelength [60]. A 808 nm laser diode excites the carriers in the quantum wells. The gain medium is an optically pumped semiconductor as depictured in Figure 16.

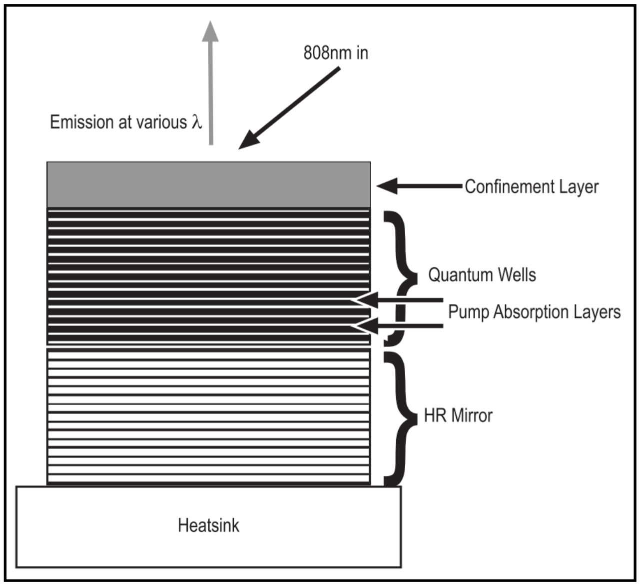

Figure 16: Illustration of the OPS chip, its different layers, the pumping and the laser process [57].

By engineering the composition and thickness of the gain medium, the wavelength can be tuned and set. As this research is implemented with rather small optical powers, the maximum laser light output of the Verdi G2 series of 2 W seems extraordinary high. However, very important parameters like a narrow bandwidth of the emitted laser light and stability are crucial for the experiments and this is complied by the laser [61].

Figure 16 illustrates the OPS chip from Coherent. The pump beam of the laser diode has a wavelength of 808 nm and is absorbed in between the quantum wells (stacks < 10 µm) by the absorption layers. Beneath, as rear surface, is a stack of dielectric layers, which act as high reflecting mirrors. An active cooling heat sink is attached to that rear side of the chip. Thermal lensing can so be neglected, as here the heat gradient still comes from the lasing operation. Nevertheless, the so very small structure leads to a minimal effect.

Figure 17 shows two common set-ups for an OPSL system. The laser diode pumps the OPS chip and is lead over a coupling (often telescope) optics onto it. The laser light from the OPS chip goes onto an output coupler, which is a concave dichroic mirror and builds one part of the laser cavity. As the emitted light of the OPS chip is 1064 nm, it further is frequency-doubled with a crystal in the beam path of the cavity and reflected by a second high-reflecting mirror. The out coupling mirrors' dichroic layer lets a small percentage (usually about 5 %) of the frequency-doubled laser light of 532 nm, leaving the cavity, continuously.

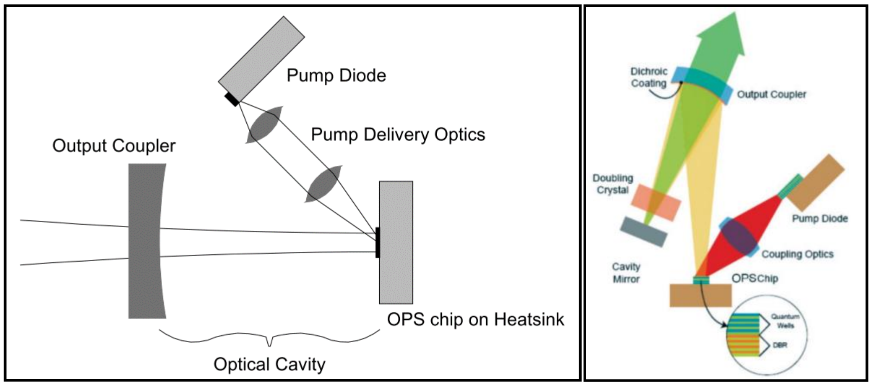

Figure 17: OPSL technology in a resonator, left simple scheme [59] and right more detailed [62] from Coherent. Description in the text above.

2.1.7 Initial operation, beam paths in the spectrometer and spectrum analysis

The outer beam paths for using the spectrometer, the alignment and tandem mode of the spectrometer in order to ensure the perfect functioning and spectrum analysis itself, is introduced.

To align the optical axis for the experimental beam path and the reference beam path optimal, it`s recommended to set long straight paths over the optical table, as illustrated in Figure 18 (showing the rheometer set-up, which we come later to in more detail). To enter the spectrometer, as parallel and orthogonal to the spectrometer and the table as possible, the experimental beam path is set to be very long. Nearly the whole range of the optical table (3 m * 1.8 m) is used for that.

Figure 18 shows the reference and experimental beam paths. The reference beam is directly split after the laser beam source and lead over 2 mirrors (for steering) and through a grey-filter (to adjust the intensity) to the side-entrance of the TFP2-HC aperture.

The experimental beam path is lead after transmission through the beam splitter, being steered with mirrors (M2, M3 and M4, for beam adjustment) onto a pentaprism (5 in Figure 18), which leads it in 90° reflection onto the aperture of the spectrometer.

The first adjustments can be made with a stencil to keep middle of the rails and height of the optical axis. Nevertheless, for a better adjustment the reflections of the pentaprism (4 % typical glass reflection), of the aperture itself and the prism for backscattering shall be used (as explained in the latter). The first back reflection, namely of the pentaprism, can be used by leading it back as far as possible and overlaying it with the beam coming from the laser (at the beam splitter). Now, as the pentaprism is reflecting exactly 90°, the opto-mechanic holder of it can be adjusted so that the transmitted light will hit the aperture of the spectrometer, giving a clean centered optical axis over the whole table.

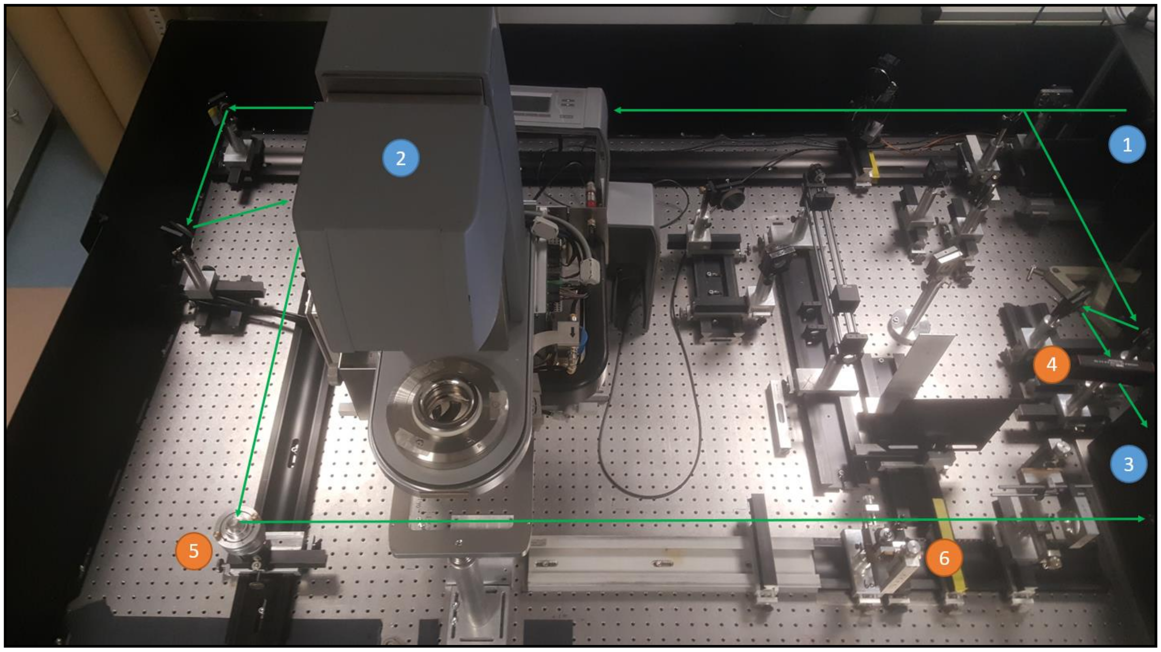

Figure 18: Illustration of the experimental beam path (described in detail in the latter). The laser source (1) sends the beam, it is split with a beam splitter and lead to the reference beam path where it goes through an intensity filter (4) and enters the spectrometer´s aperture (3) from the side. The experimental beam path is lead over the whole range of the optical table and send to the pentaprism (5) which reflects in 90°, passing under the rheometer (sample stage) (2), which is placed above the optical axis and the prism (6) for backscattering (which is unadjusted here), entering the aperture of the spectrometer from the front.

The interior optics of the spectrometer are quite sensitive and not easy to adjust, so this long (experimental) beam path arm is useful for the first calibration, as it is quite certain then, that the beam is entering the spectrometer well aligned and all further optical alignments have nothing to do with exterior issues.

Having the reference beam path and the experimental beam path set up and adjusted, one can start the calibration of the alignment- and tandem-mode-beam-paths of the spectrometer.

Before an experimental series, one should be aware of the settings, which have to be set regarding the goal of the study. This means, the FSR for the material of interest has to be known accordingly. Further, the mirror separation, the pinhole sizes and scan ranges should be set in combination [36, 56, 63-66].

The spectrometer has two “beam modes” that are to be used. One mode is to first calibrate and adjust the internal optics (alignment-mode) and then the full six-pass through the whole spectrometer (tandem-mode), which is used for the experiments and spectrum analysis.

The **alignment mode** beam path uses the FP`s in reflection mode, so one can test if the mirrors are set properly to the photon counter. The beam paths of the alignment mode are sketched in Figure 19 and shown as a sketch of the optical elements in the user manual [36].

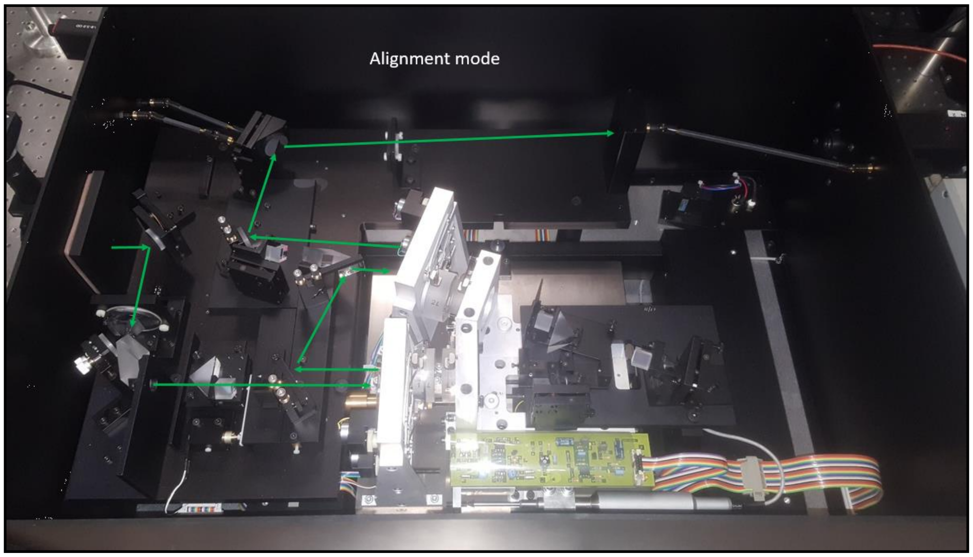

Figure 19: Illustration of the alignment mode of the TFP2-HC spectrometer. The beam is lead onto both FP doublets that are set to reflect the beam instead of transmission and it finally reaches the photon counter.

The **tandem mode** (illustrated in Figure 20) uses the full six-passes through the spectrometer as depicted in Figure 14.

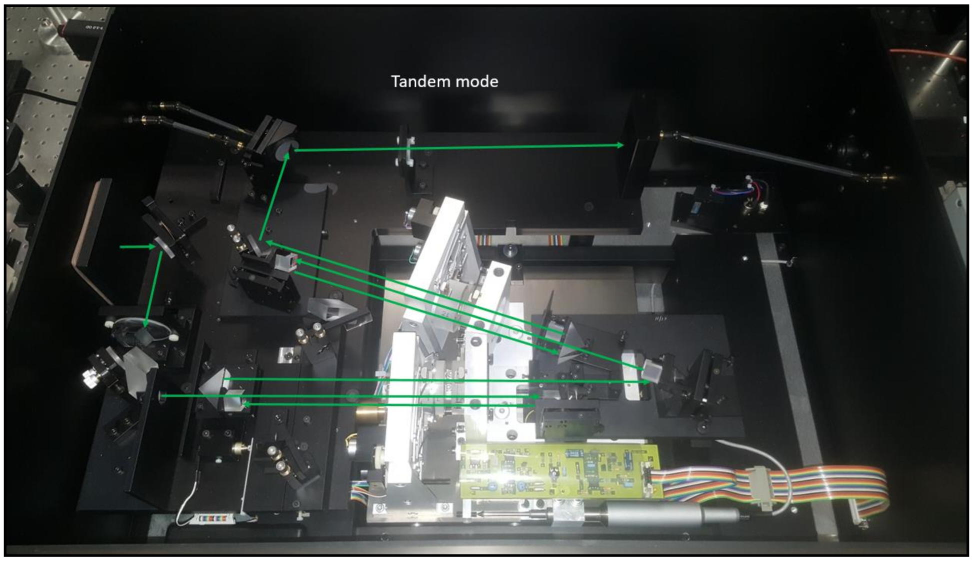

Figure 20: Illustration of the tandem mode of the TFP2-HC spectrometer. The beam is lead in each three passes through both FP-doublets that are set to transmission and reaches the photon counter after six passes.

The **Spectrum analysis** can be implemented with the software of the manufacturer of the spectrometer, namely, the Ghost software form (JRS). This software, shown in Figure 21, can be used to picture the absorption and transmission spectra of the Fabry-Perot doublets.

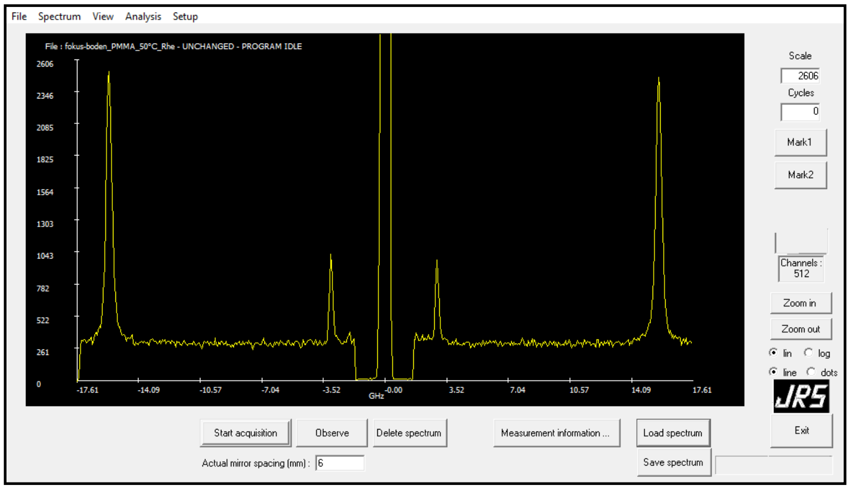

File : fokus-boden_PMMA_50°C_Rhe - UNCHANGED - PROGRAM IDLE

Scale: 2606

Cycles: 0

Channels : 512

Actual mirror spacing (mm) : 6

Figure 21: Screenshot of the Ghost software main window, from JRS (spectrum of a PMMA sample). Setting the mirror spacing, the FSR is automatically set. Observing the signal gives a live view to the spectra as a measurement is started by Start [67, 68].

Internal fit functions can be used for evaluation of the spectra as exemplarily shown in Figure 22. The three different possible functions are the Damped Harmonic Oscillator (DHO), the Gaussian and the Lorentian model.

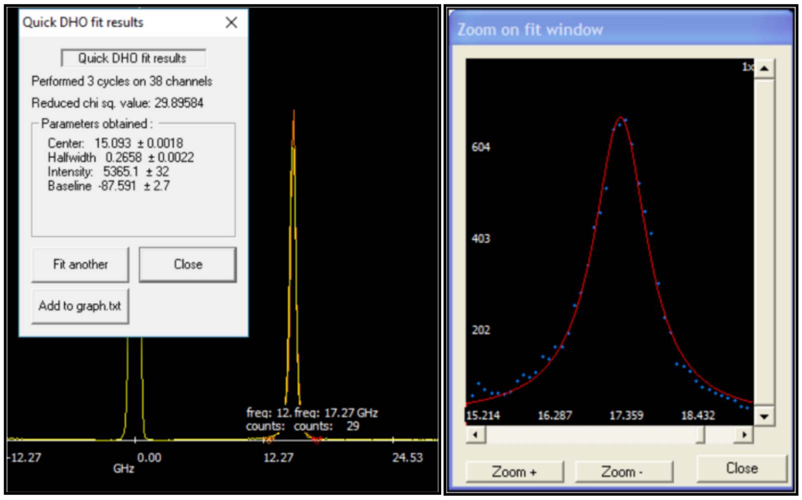

Quick DHO fit results

Performed 3 cycles on 38 channels

Reduced chi sq. value: 29.89584

Parameters obtained :

Center: 15.093 ± 0.0018
Halfwidth 0.2658 ± 0.0022
Intensity: 5365.1 ± 32
Baseline -87.591 ± 2.7

Figure 22: Screenshot of the (DHO) quick fit window of the Ghost software to the left, right a more detailed view, the "zoom on fit window" which shows the data points and one can export the original data series from here as pleased [68].

However, in this work, most of the evaluation is done manually with Origin software [69] to be most precise with the fitting of values and collection of the data for different experimental sequences, in a fine, comparable and reproducible way. Nevertheless, also DHO fitting with the Ghost software (from JRS) has been used to evaluate the measurements.

To acquire a Brillouin spectrum, the Ghost software is fed by the signal from the avalanche photo diode (SPCM-AQ), which is set as the photon counter of the spectrometer for this work. The gathered data of signal-counts over frequency is exported as raw data and is imported to the Origin software, where it is plotted (Figure 23). A tool of the Origin software is the base line correction that is pictured with the red dots in the spectrum picture and after subtraction, it looks like shown in Figure 24. The yellow dotted line in Figure 23 is noted as signal height in the latter evaluation, as the blue dotted line indicates the noise signal, which to be precise, includes also the quasi-elastic scattering parts.

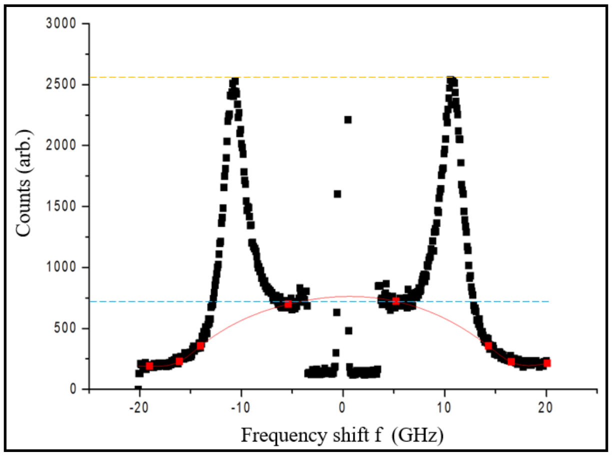

Figure 23: Brillouin spectrum of the sample material (PVP 2.5 mass percent PEG) in the sample stage with a gap size of 0.5 mm and no applied shear rate. The orange line indicates the later used signal height values, as the blue line indicates noise values, respectively. The red curve shows the base line correction of Origin, which is subtracted and follows in a spectrum like Figure 24 pictures.

Figure 24 shows previous spectrum after the beat line correction and for further evaluation a Gaussian fit is applied, giving among others, the signal height (Height) value and the Brillouin shift frequency (xc).

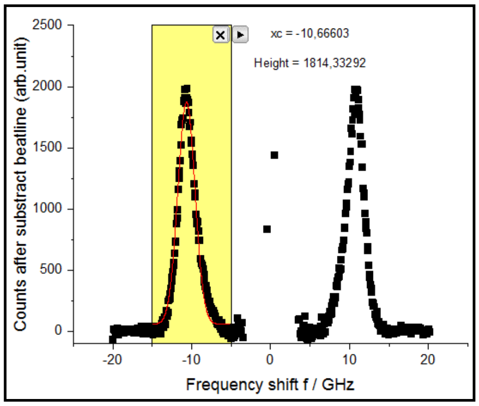

Figure 24: Origin plot of a beat line corrected Brillouin spectrum, collected from the sample material (PVP 2.5 mass percent PEG) on the stage with no applied shear. Right top, the Origin fit values, xc: the frequency shift and Height: the signal height.

The values for each of both peaks are collected, summed up and their average values for frequency and signal height are shown in the plots.

2.2 Rotational rheometry

The rotational rheometer is introduced as well as shear, strain and viscosity.

The rheometer used for this work is a MCR302 rotational rheometer series [37, 70] from Anton Paar (Figure 25). It was also used in own previous rheological studies [71, 72] to get more experienced with the system, the rheology itself and find fitting materials. The software used, is called RheoCompass. It is used for control and evaluation. In this work, again, the raw data are collected and evaluated with Origin software.

Figure 25: Picture of a MCR 302 rotational rheometer from Anton Paar used for this study [37, 70].

The range of materials that can be studied with such a rotational rheometer is from low-viscosity liquids over visco-elastic liquids, gel-like materials to even soft solids. Further, melts, paste like materials, reactive systems, and solids can be investigated with such a system. In the frame of this work, to control the temperature and humidity in the sample (and scattering volume) more accurate, an additional system is installed, namely a hood (H-PTD200/GL), which is pictured in Figure 26 as well as the glass ground plate that is used to gain optical access from below.

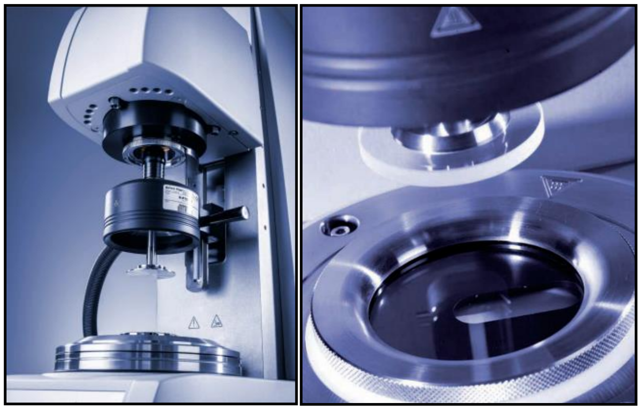

Figure 26: Picture of the H-PTD200/GL hood for temperature control of the MCR302 rheometer series with a PP50 geometry from Anton Paar left; right, top view on the glass ground plate that is the optical access for latter experiments of Brillouin Rheology (and an installed GL43 glass geometry).

Figure 27 shows common rotational rheological geometries. Plate-plate geometries (PP`s) with a diameter of 8 mm, 25 mm and 50 mm are shown as well as the cone-plate geometry (CP25) and glass geometries (GL`s) with 25 and 43 mm, respectively. The latter diameter seems unusual, but it is connected to the ground glass plate construction and the Peltier temperature control unit, which gives the boundary condition of a maximum diameter of 43 mm for any plate to use with this set-up.

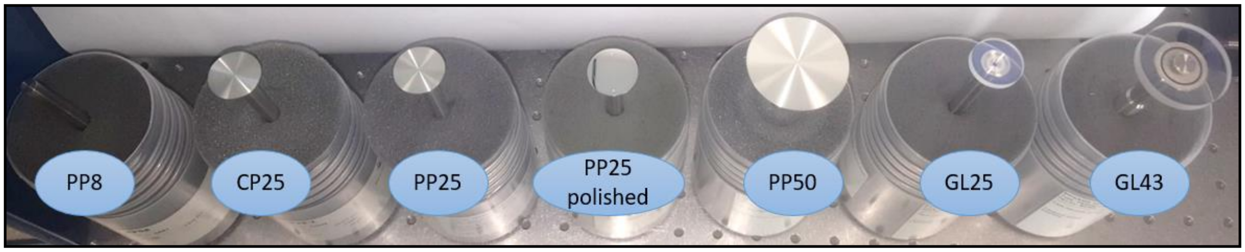

Figure 27: Overview of common rotational rheological geometries, from left to right, a plate-plate geometry with a diameter of 8 mm. A cone-plate geometry with 25 mm diameter and an angle of 1° from center to edge of the geometry. The plate-plate geometry with 25 mm and a polished one, which is used for the most experiments in this work are shown next to the 50 mm diameter plate-plate geometry. The glass geometries with diameters of 25 mm and 43 mm are shown and tested for latter approaches of different scattering geometries, but are not in the frame of this work.

The rheometer gives a broad variety and many options for experiments and rotational tests. For this work mainly flow and viscosity curves are measured, so introduced in the following. Principal investigations can be implemented for the elastic behavior and shear modulus, viscoelastic behavior, creep tests, relaxation tests and oscillatory tests. The investigation of rheological behavior has many influences, so certain conditions are important to fulfill and recognize e.g. the type of loading regarding the preset of deformation, shear strain or shear stress.

Rheology is the ‘study of deformation of matter’ [73], so the understanding of strain and stress is essential. The definitions of liquids and solids, the general rheometry, the behavior of deformation and flow are mainly assumed to be known, so they are not explained in detail (here some fine references [74-80]). However, the for this work important topics will be briefly explained [73, 81].

If one considers a rectangular bar (Figure 28), which is elongated due to a tensile force, it can be expressed in terms of **Cauchy strain** (also called engineering strain). Eq. (10) shows the relation between the initial length L_0, the elongated length L and the increased length δL of the elongated rectangular bar:

$$\mathrm{L} = \mathrm{L}_0 + \delta\mathrm{L} \tag{10}$$

Eq. (11) shows the description in terms of Cauchy strain:

$$\varepsilon_c = \frac{\delta\mathrm{L}}{\mathrm{L}_0} = \frac{\mathrm{L} - \mathrm{L}_0}{\mathrm{L}_0} = \frac{\mathrm{L}}{\mathrm{L}_0} - 1 \tag{11}$$

One also can formulate this relation in terms of Hencky strain (Eq. (12)), which is also called true strain and is determined by evaluating an integral from L_0 to L:

$$\varepsilon_h = \int_{L_0}^{L} \frac{dL}{L} = \ln(L/L_0) \tag{12}$$

If the material is unstrained both, Cauchy and Hencky strain are zero, and they are approximately equal at small strains.

$$\varepsilon_h = \ln(1 + \varepsilon_c) \tag{13}$$

For large deformations, the Hencky strain ε_h is preferred to be used. The relation of Cauchy and Hencky strain is formulated in Eq. (13).

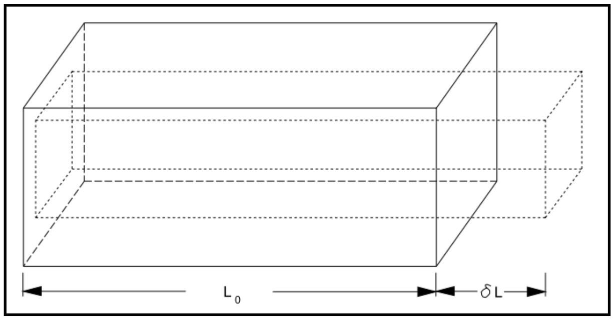

Figure 28: Strain, illustration of elongation of a rectangular bar, due to a tensile force. [73]

The **simple shear** can be imagined, again, by a rectangular bar, which now is stationary at the lower surface and linearly displaced by δL at the upper side (Figure 29). The size of the element is not relevant, as the level of deformation is equal. Eq. (14) gives a formula to express the deformation angle of shear γ_A:

$$\tan(\gamma_A) = \frac{\delta L}{h} \tag{14}$$

Having small deformations, the shear strain and the angle of shear (in radians) are considered to be equal ($\tan(\gamma_A) = \gamma$).

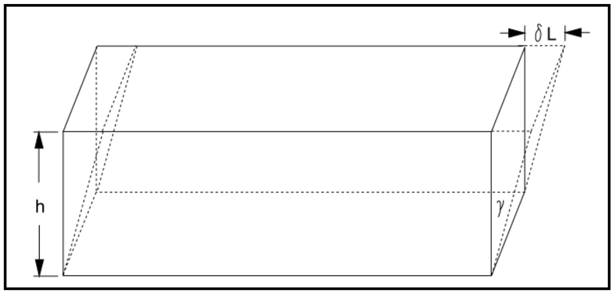

Figure 29: Shear, illustration of deformation of a rectangular bar. [73]

Stress can be shear, tensile, or compressive. It is defined as force per unit area and expressed in Pascal (N/m^2). For completely describing the state of stress in a material, nine separate quantities are required. Considering a small material element in terms of Cartesian coordinates ($x_1,\ x_2,\ x_3$), the stress can be indicated by σ_{ij} (Figure 30).

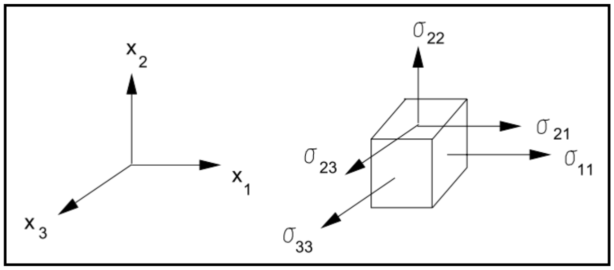

Figure 30: Stresses of a material element with Cartesian coordinates (3D). [73]

The subscripts refer once, to the orientation of the face upon the force acts (first) and to the direction of the force (second). As an example, a normal stress, acting in the plane perpendicular to x_1 and in direction of x_1, is denoted as σ_{11}. A shear stress acting in direction of x_3 and in the plane perpendicular to x_2 is denoted as σ_{23}.

One can write the stress components now in a matrix form (Eq. (15)), showing the nine necessary quantities, which are required to describe the complete state of stress in a material:

$$\sigma_{ij} = \begin{pmatrix} \sigma_{11} & \sigma_{12} & \sigma_{13} \\ \sigma_{21} & \sigma_{22} & \sigma_{23} \\ \sigma_{31} & \sigma_{32} & \sigma_{33} \end{pmatrix} \tag{15}$$

Rheological equations of state or consecutive equations show the relationship between stress and strain. For complex materials they usually include further variables, such as temperature, pressure and time. The ratio of stress to strain is called modulus. The ratio of strain to stress is called compliance.

Applying a force to a **solid material**, it follows **Hooke's law**. The general description from Robert Hook in 1660 states, that 'the displacement or size of deformation of a relatively small object is proportional to the deforming force or load'[3]. It can be formulated as a displacement or change in length x_H times a constant k_H (like a spring constant) equals the applied force F_H (Eq. (16)).

$$F_H = k_H \cdot x_H \tag{16}$$

Such Hookean materials do not flow and are linear elastic. That means that the stress remains constant until the strain is removed, then the material returns to its original form. Introducing the

---

[3] Encyclopedia Britannica, Inc.

shear modulus G, one can states the relationship for shear strain γ and shear stress σ as follows (Eq. (17)):

$$\sigma_{12} = G \cdot \gamma \tag{17}$$

Many materials subjected to small strains can be described by Hooke's law.

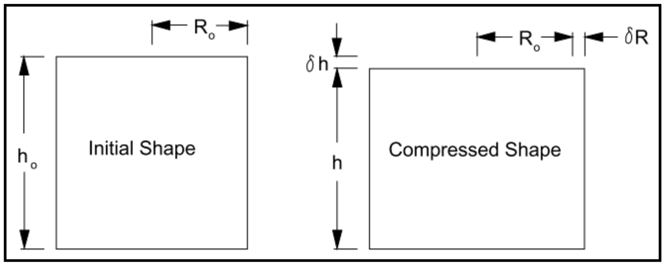

Figure 31: Illustration of compression of a cylindrical shaped material. [73]

If a Hookean material is compressed (here a cylinder shape), so that it has a change in radius, or length (Figure 31), then the normal strain (Eq. (19)) and stress (Eq. (18)) can be formulated as follows:

$$\sigma_{22} = \frac{F_H}{A} = \frac{F_H}{\pi(R_{0H})^2} \tag{18}$$

$$\varepsilon_c = \frac{\delta h}{h_0} \tag{19}$$

The **modulus of elasticity**, called **Young's modulus**, can now be determined (Eq. (20)):

$$E_Y = \frac{\sigma_{22}}{\varepsilon_c} \tag{20}$$

The relation of Young's modulus E_Y and shear modulus G are related in an isotropic medium as follows (Eq. (21)), where ν_Y is the Poisson's ratio (-lateral strain / longitudinal strain):

$$G = \frac{E_Y}{2(1 + \nu_Y)} \tag{21}$$

To study fluids, which are subjected to continuous shear for a constant rate, one can use the model of two parallel plates with a fluid in between the gap (height h_{PP}). If the lower plate is fixed and the upper plate has a constant movement with the velocity u_{PP}, one can be modeled as an incremental change of position for a small period of time ($\delta L_{PP}/\delta t$).

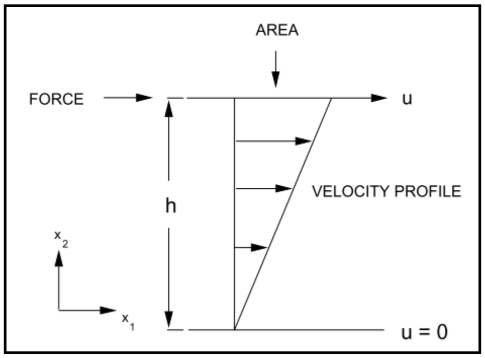

Figure 32: Illustration of a velocity profile in between two parallel plates. [73]

The rate of change of strain defines the described flow, which can be seen as steady simple shear and shear rate $\dot{\gamma}$ (Eq. (22)). The equation only suits laminar flows between parallel plates, like a sliding plate viscometer, described by Dealy and Giacomin [82].

$$\dot{\gamma} = \frac{d\gamma}{dt} = \frac{d}{dt}\left(\frac{\delta L_{PP}}{h_{PP}}\right) = \frac{u_{PP}}{h_{PP}} \tag{22}$$

To describe a **flow of a material**, one has to consider three dimension to describe the state of stress or strain completely. For a simple steady shear flow, the stress tensor may be oriented with the flow direction. The matrix (Eq. (15)) the reduces to (Eq. (23)):

$$\sigma_{ij} = \begin{pmatrix} \sigma_{11} & \sigma_{12} & 0 \\ \sigma_{21} & \sigma_{22} & 0 \\ 0 & 0 & \sigma_{33} \end{pmatrix} \tag{23}$$

Such a simple shear flow may be referred to as viscometric flow. This includes torsional flow (or rotational) in between plates, axial flow in a tube, and rotational flow between concentric cylinders or between a cone and a plate.

Giving also a more technical description and denotation, the shear stress τ (sometimes/beforehand denoted as σ) is defined as shear force F_S (N) divided by shear area A_S (m^2) as denoted in Eq. 26. The unit of the shear stress is Pascal.

$$\tau = {}^{F_S}/_{A_S} \tag{24}$$

The shear rate $\dot{\gamma}$ is defined as the velocity v_S (m/s) divided by the distance between the plates (here, the sample height H_S) as given in Eq. (25) (and Eq. (22)). Its unit is reciprocal seconds. Synonyms are velocity gradient, rate of deformation and strain rate.

$$\dot{\gamma} = {}^{v_S}/_{H_S} \ (= \frac{u_{PP}}{h_{PP}}) \qquad (25)$$

Figure 33 illustrates the common rheological set-up of a plate-plate geometry with a loaded sample (indicated yellow) in between, giving the experimental parameters of gap size H_S, radius of the sample (and geometry) R_S and the applied torque, which gives a rotational speed or angular velocity ω_S. The red dot indicates the scattering volume position of the Brillouin spectroscopy in the sample.

It is known that with the plate-plate geometries the shear field inside the sample is not homogeneously distributed (like for a cone-plate geometry), so the rheometer software (RheoCompass) calculates in accordance to the used geometry, a value for shear viscosity η by the measured shear stress τ for a given shear rate $\dot{\gamma}$.

However, this is a macroscopic measurement in principle, whereas the Brillouin spectroscopy is used for a local measurement of mechanical properties, so it is necessary to know the accurate value for the shear rate (locally) at the position of the scattering volume.

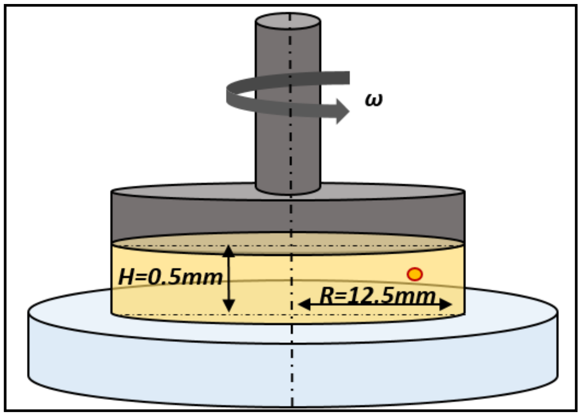

Figure 33. Illustration of a plate-plate (PP25) rheological geometry (black) having a loaded sample (yellow) in a 0.5 mm high gap. The ground glass plate is indicated blue. The red circle indicates a possible position of the laser focus, so the scattering volume.

Depending on the torque M of the rheometer, and the radial position R (here the radius of the geometry), the shear stress τ is expressed by Eq. (26).

$$\tau = \frac{2M}{\pi \cdot R^3} \qquad (26)$$

The local shear rate $\dot{\gamma}$ at a certain position R depends on the angular velocity ω_S applied by the rheometer and the gap size H_S, which gives following relation (Eq. (27)).

$$\dot{\gamma} = \frac{\omega_S \cdot R}{H_S} \qquad (27)$$

Materials that show a flow behavior are referred to as fluids (both, liquids and gases). As flowing fluids obtain inner friction forces of the molecules, there is a resistance in flow that is called viscosity. To further specify, the expressions of shear viscosity (sometimes called dynamic viscosity) and kinematic viscosity are introduced.

An ideal viscous fluid has a material constant, the **shear viscosity η** that describes the ratio between the shear stress τ and the shear rate $\dot{\gamma}$ for a constant temperature and is written in following relation (Eq. (28)).

$$\eta = {}^{\tau}\!/_{\dot{\gamma}} \tag{28}$$

The unit of the shear viscosity is Pascal-seconds (Pas) as for low-viscosity fluids milli-Pascal-seconds and is used mainly in this work to describe the rheology.

The term dynamic viscosity is also used for this relation (as mentioned before) and listed in DIN1342-1, but it is used more in the sense of describing the complex viscosity, determined by oscillatory tests, or even just the real part of it, so in this work, the variable η is used for the viscosity or shear viscosity.

The mainly used experimental method presets of rotational rheology are called controlled shear rate (CSR) and controlled shear stress (CSS) tests. For the CSR test, the rotational speed n_{ROT} (min^{-1}) and the shear rate $\dot{\gamma}$ (s^{-1}), are the presets and the results are the torque M (Nm) and the shear stress τ (Pa), wherefrom the shear viscosity η (Pas) is calculated. The CSS test is mainly the opposite, namely, setting the torque M and the shear stress τ, acquiring the rotational speed ω and the shear rate $\dot{\gamma}$, to determine the viscosity. This work is implemented with the CSR mode, as the shear rates are the presets for the experiments.

The rheological acquired data is usually plotted as shear stress τ over shear rate $\dot{\gamma}$ and is referred to as flow curve. Plotting the viscosity η over the shear rate $\dot{\gamma}$ is called viscosity curve (as depictured in Figure 34).

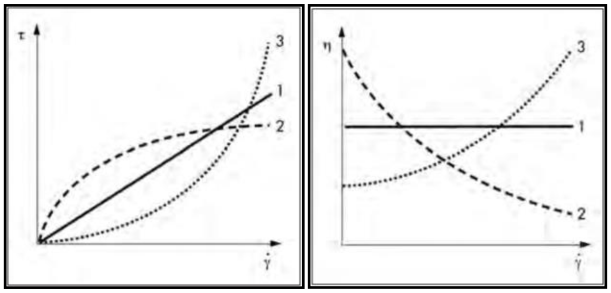

Figure 34: Comparison of flow curves (left) and viscosity curves (right) for different circumcisions. (1) ideally viscous (Newtonian) fluid, (2) shear thinning and (3) shear thickening [81].

The stiffness tensor

The relation or connection between the sound velocity in a medium and its stiffness tensor is an important relation in material sciences. This tensor characterizes a material’s behavior in the elastic regime under stress. It can be represented as a symmetric 6 x 6 matrix or by a 4-tensor in 3D space with 81 components. 21 of those 81 matrix elements are independent are called elastic constants. The material’s resistance to certain strains are quantified by those constants. The stiffness tensor will contain information about how sound waves behave in the medium, since the sound can be seen as a form of an elastic wave, which is traveling in a material. By solving the Christoffel equation one can predict the sound velocities in a medium, wherefore, the elastic constants have to be known. Contrariwise, a common way to find the elastic properties or constants of a material is to experimentally determine the sound velocities. [83]

A generalization of Hook’s law (introduced in the rheometry part of this work) in three dimensions, relating stresses and strain in the elastic regime, is called the stiffness tensor C, which is a fundamental property of a medium. The relation is pictured in following Eq. (29), where ε is the strain tensor (as in previous chapter) and σ is the stress tensor:

$$\sigma_{ij} = \sum_{nm} C_{ijnm} \varepsilon_{nm} \tag{29}$$

Picturing the 6 x 6 matrix of the elastic stiffness tensor (Eq. (30)) shall then be sufficient here, to give a picture of what is been spoken of, when it is said that a future goal is to determine the whole elastic stiffness tensor with the newly developed method of Brillouin Rheology.

$$\left(\begin{array}{c} \sigma_1 \\ \sigma_2 \\ \sigma_3 \\ \hline \sigma_4 \\ \sigma_5 \\ \sigma_6 \end{array}\right) = \left(\begin{array}{ccc|ccc} C_{11} & C_{12} & C_{13} & C_{14} & C_{15} & C_{16} \\ C_{12} & C_{22} & C_{23} & C_{24} & C_{25} & C_{26} \\ C_{13} & C_{23} & C_{33} & C_{34} & C_{35} & C_{36} \\ \hline C_{14} & C_{24} & C_{34} & C_{44} & C_{45} & C_{46} \\ C_{15} & C_{25} & C_{35} & C_{45} & C_{55} & C_{56} \\ C_{16} & C_{26} & C_{36} & C_{46} & C_{56} & C_{66} \end{array}\right) \left(\begin{array}{c} \epsilon_1 \\ \epsilon_2 \\ \epsilon_3 \\ \hline 2\epsilon_4 \\ 2\epsilon_5 \\ 2\epsilon_6 \end{array}\right) \tag{30}$$

Figure 35: Picturing Eq. (30), the 6 x 6 matrix of the elastic stiffness tensor through (Voigt notation). [83]

2.3 Refractometry

The Abbemat automatic refractometer (Figure 36) is a tool to measure the refractive index of materials by optical means with the physical principle of light refraction. The refractive index n is a dimensionless constant that describes how fast light can travel through a specific medium (in relation to vacuum) [55].

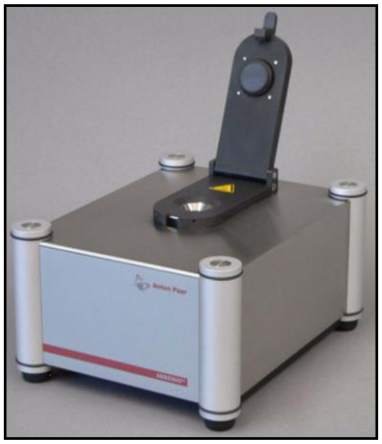

Figure 36: The Abbemat multi wavelength automatic refractometer from Anton Paar [38].

The speed of light is “higher” in a low optical density medium as the refractive index is lower. As an example, the speed of light in air is 299710 m/s and it is decelerated in water down to 225000 m/s.

The principle of refractometry is based on Snell`s law[4], which describes a change of the angle of an incident beam that enters a new medium, due to the change of the refractive index. More precise, the effect of total reflection is used, as depictured in Figure 37.

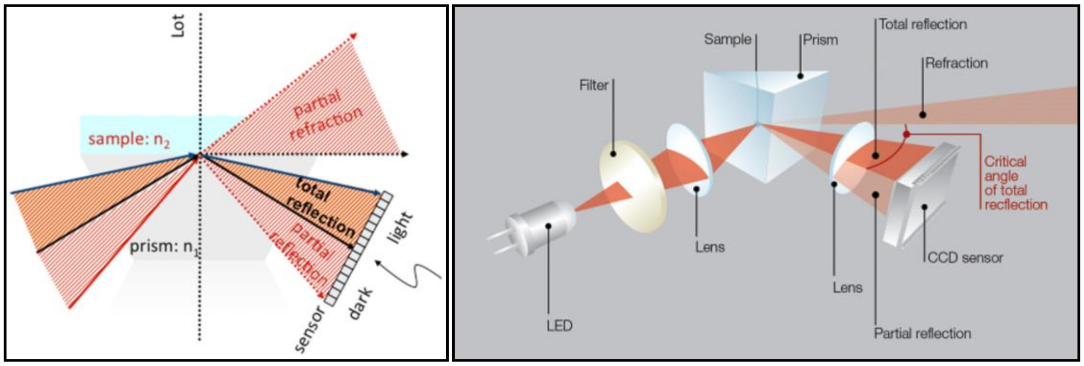

Figure 37: Left[5], principle of total reflection used to apply refractometry. Right[6], schema of an automatic refractometer where the sample is placed on the backside of the prism.

---

[4] Snell–Descartes law and the law of refraction

[5] wiki.anton-paar.com/kr-kr/basics-of-refractometry/

[6] mrclab.com/refractometers

Figure 37 (left) illustrates how a light beam is focused in the refractometer for a certain wavelength through a prism onto a sample. The total reflection occurs at the interface of the two different media, holding $n_2 < n_1$. Changing the angle of incidence gradually (scanning), the reflection can be observed with a sensor (CMOS or CCD chip), as its derivation in angle. Scanning now the critical angle of total reflection, the refractive index can be obtained. Figure 37 (right) shows the schematics of an automatic refractometer. The light source is a white light LED. Its light is lead through different edge filters to obtain certain wavelengths (589.3 nm, 435.8 nm, 480 nm, 486 nm, 488 nm, 514.5 nm, 532 nm, 546.1 nm, 632.8 nm, 643.8 nm and 656.3 nm) and is focused through the prism onto the sample, where the critical angle of total reflection is recorded and evaluated with a CCD sensor.

Chapter 3: Material and Experimental methods

The sample material for the main experiments is introduced, the Brillouin Spectroscopy theory explained and the idea as the creation of the Brillouin Rheology method is shown.

3.1 Material

The PVP 2.5 mass percent PEG sample material combination is chosen as a transparent, non- toxic and easy to handle sample, which shows shear thinning [84] and inhibits a good scattering cross section. The polymer Polyvinylpyrrolidone $(C_6H_9NO)_n$ (PVP1300000 from Sigma Aldrich) with an average molecular mass of 1300000 g/mol is combined with the solvent Polyethylen glycol (PEG400 from Carl Roth) with a molecular mass of 380-420 g/mol. (Some literature to those polymers, their combination and applications and other research is given in [85-103].)

The polymer and the solvent are combined with a tilt/roller mixer from Carl Roth. They are kept at a temperature of 70°C for further mixing in a magnet stirrer for 24 hours. The result is a transparent sample that has 2.5 mass percent polymer (PVP1300000) in the solvent (PEG400). Air bubbles, due to the mixing process, are removed by applying vacuum.

The mass density and the refractive index of the sample material are crucial parameters for the latter evaluation of the Brillouin Rheology. Figure 38 shows the temperature dependency of these quantities measured with a density meter 5000M and the Abbemat refractometer from Anton Paar.

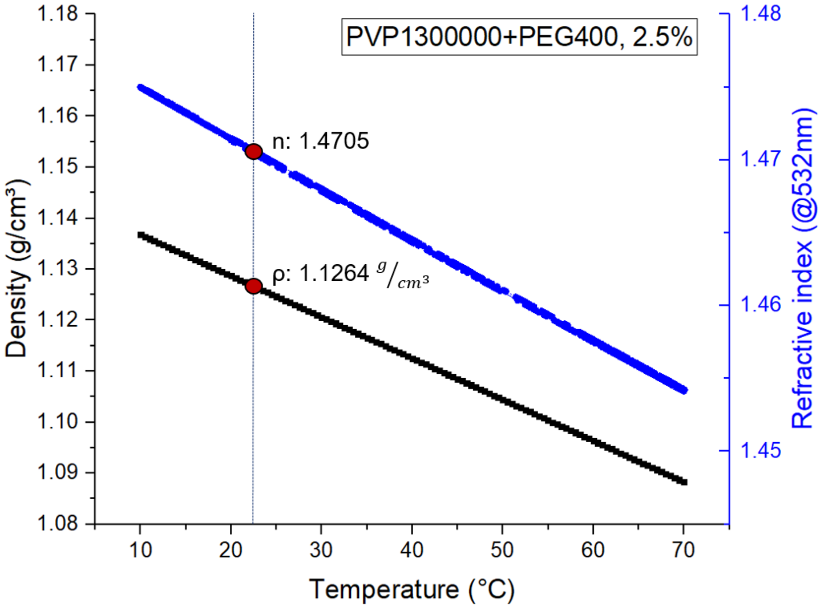

Figure 38: Refractive index and density of the PVP 2.5 mass percent PEG mixture, obtained with the Abbemat refractometer and a density meter 5000M from Anton Paar.

The density for the sample material at a certain chosen temperature of 22.5°C is 1.1246 g/cm^3 (measured with density meter 5000M from Anton Paar) and the refractive index 1.4705 (Abbemat refractometer from Anton Paar). The indicated temperature of 22.5°C is a temperature that was chosen for most of the experiments with this sample material in the latter.

3.2 Experimental methods

This section introduces the experimental methods, theoretical background of scattering, and the applied scattering geometries for the experiments. Further, the idea of Brillouin Rheology is explained and the corresponding systems as the realization and development of the opto-mechanical system is shown.

3.2.1 Brillouin spectroscopy, scattering processes and scattering geometries

Brillouin spectroscopy is a non-contact optical method to determine elastic properties of materials. More precise, the light scattering from density variations of transparent materials (also some opaque materials and surfaces of non-transparent materials [43]) can be used to acquire information about sound waves in the material, where from elastic properties can be derived. However, for a better understanding, the scattering of light is introduced.

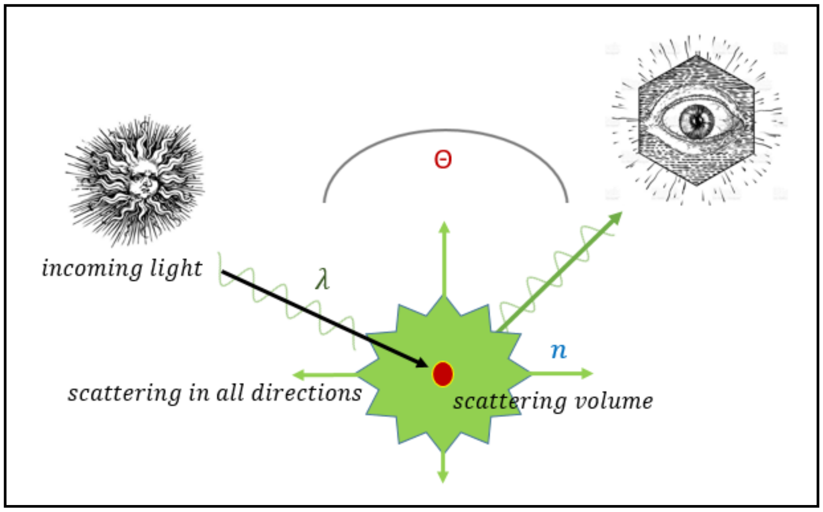

Figure 39: Illustration of scattering process of an incident light beam at a scattering volume. Depending on the position of observance, the q-vector of the acoustic wave in a certain orientation can be investigated. (λ the wavelength of the incoming light, Θ the scattering angle and n the refractive index of the medium where the scattering occurs.) More details follow in the text below.

The most known scattering processes are called Rayleigh [104], Raman [105] and Brillouin scattering [10], so they are introduced shortly (Figure 40). The energy E_{Ph} of a photon (frequency ν_P) is shown in the following equation, with $\boldsymbol{c}$ as the speed of light with $2.998 * 10^8\ m/s$ and h_P Planck`s constant $6.626 * 10^{-34}\ Js$.

With $c = \lambda * \nu_P$, one can write the following relation (Eq. (31)) [106].

$$\mathrm{E_{Ph}} = \frac{\mathrm{h_P c}}{\lambda} = \mathrm{h\nu_P} \tag{31}$$

The process of Rayleigh scattering causes a photon to change its direction. Nevertheless, its energy is conserved, so one speaks of elastic scattering ((a) in Figure 40) as the emitted photon has the same energy than the absorbed one.

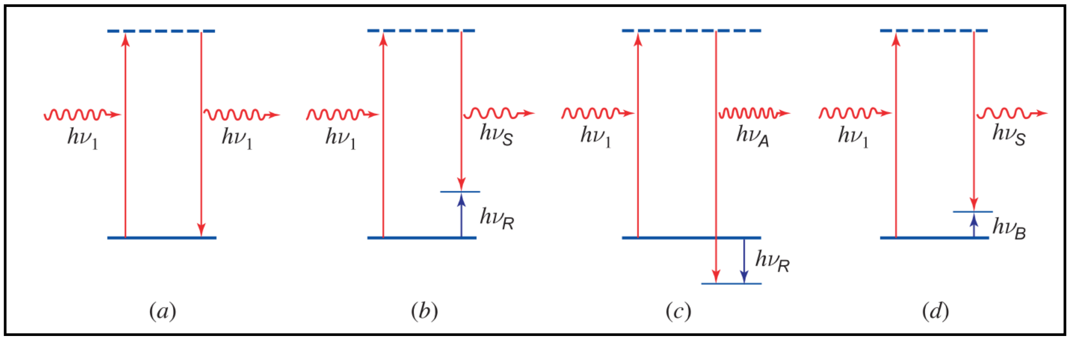

Figure 40: Scattering effects, (a) Rayleigh; (b) Raman (Stokes); (c) Raman (anti-Stokes) and (d) Brillouin (Stokes). As those are non-resonating scattering, the dotted lines indicates virtual states [107].

The process of Rayleigh scattering causes a photon to change its direction. Nevertheless, its energy is conserved, so one speaks of elastic scattering ((a) in Figure 40) as the emitted photon has the same energy than the absorbed one. This scattering happens in solids, liquids and gases and is brought about due to inhomogeneities in glasses' refractive indices, or from particles, which sizes are much smaller than the wavelength of the scattering process (like atoms, electrons, molecules, or nano-particles). The intensity of the scattered light is proportional to (the frequency of the incoming light) ν_P^4 and so (to the wavelength) ${}^{1}/_{\lambda^4}$. Therefore, the sky appears to be blue.

Raman scattering is an inelastic scattering process as there is an energy interchange ($h\nu_R$ in Figure 40 (b) and (c)), with a vibrational and/or rotational mode of a molecule or a phonon of a solid-state material. The following denotation shows the Stokes and anti-Stokes cases, which describe energy given (Stokes (b)) or taken (anti-Stokes (c)) from/of the photon to the matter (Eq. (32) and Eq. (33)).

$$\mathrm{h}\nu_\mathrm{S} = \mathrm{h}\nu_\mathrm{I} - \mathrm{h}\nu_\mathrm{R} \tag{32}$$

$$\mathrm{h}\nu_\mathrm{A} = \mathrm{h}\nu_\mathrm{I} + \mathrm{h}\nu_\mathrm{R} \tag{33}$$

This scattering appears to be in gases, fluids and solid-state materials. In principle the spectrum of scattered light from a material consist of a Rayleigh component, having the frequency of the incoming light and blue or red shifted side bands from the inelastic scattered Stokes and anti-Stokes components. Even this scattering is a weak process, having just $10^{-7}$of the intensity of the incoming light, it is used for material characterization.

Brillouin scattering is also an inelastic scattering process ((d) in Figure 40 shows the stokes Brillouin scattering) that seems to be very similar to the Raman scattering, but the source of the effect is different. Light is scattered by acoustic modes of a medium, not by vibrational modes [107]. One also can state, that from an empirical point of view, those scattering processes differ only so far, that acoustical modes are involved in the Brillouin scattering, as optical phonons in

Raman scattering. By studying phonons with Brillouin spectroscopy, one can get information about the transversal (TA) and longitudinal (LA) acoustic modes for small wave vectors q. The observed frequency shifts can be transformed to sound velocity and it is possible to determine the elastic constants out of them as well [108].

Describing the Brillouin scattering as Leon Brillouin [10] as scattering of light waves on thermally induced sound waves, we can write Eq. (32) and Eq. (33) in quantum dynamical means, keeping the conservation of momentum and energy (Eq. (34) and Eq. (35)) [109].

$$\hbar\omega_{\mathrm{s}} = \hbar\omega_{\mathrm{i}} \pm \hbar\Omega \tag{34}$$

$$\hbar\vec{\mathrm{k}}_{\mathrm{s}} = \hbar\vec{\mathrm{k}}_{\mathrm{i}} \pm \hbar\vec{\mathrm{q}} \tag{35}$$

In this denotation ω_i and $\vec{k}_i$ represent the angular frequency and the wave vector of the incoming light, respectively. Further, the angular frequency of the scattered light ω_s and the wave vector $\vec{k}_s$. The phonon´s angular frequency is written as Ω and its wave vector as $\vec{q}$. The $\pm$ denotes the Stokes and anti-Stokes of the photons and phonons, meaning the creation and annihilation, respectively [110]. Figure 41 shows a simplified sketch of such a scattering process.

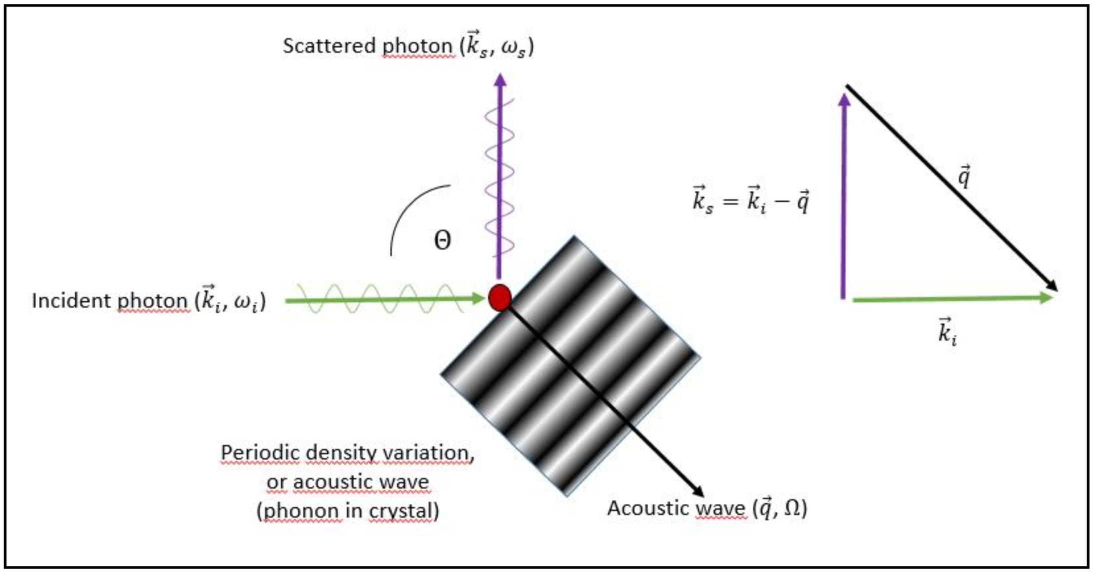

Figure 41: Scattering process; the laser light is scattered at a scattering volume (indicated as red circle). The wave vectors for the incident and scattered light $\vec{k}_i$ and $\vec{k}_s$ as for the wave vector $\vec{q}$ and the incident angle θ_i are indicated.

Figure 42 pictures a spectrum for the different scattering processes. The Rayleigh scattering intensity is extremely high compared to the Brillouin and Raman scattering. The shift of the Brillouin peaks, in frequency, depends on the temperature and the elastic property of the material. The peaks are very close to the input signal (in the GHz regime), so very sophisticated filtering methods are necessary for evaluation.

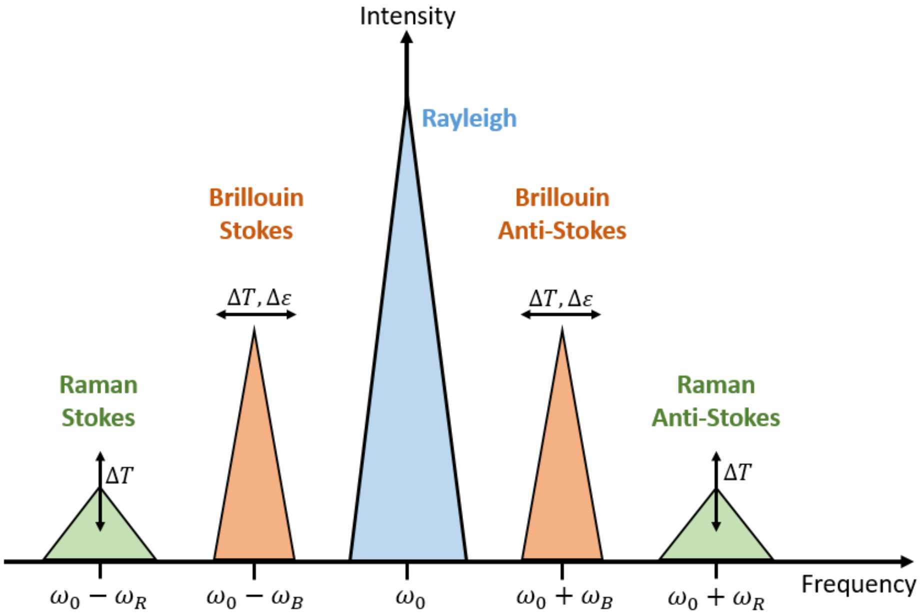

Figure 42: Illustration of scattering spectra, adopted from [111]. The Rayleigh peak is extraordinary high in intensity. The Brillouin shifts, in frequency, depend on temperature and elastic properties. The height of the Raman peaks depend on temperature effects in the material.

The Raman peaks, in comparison, are largely separated (in the THz regime), which makes it easy to filter the Rayleigh scattering signal and achieve a good Signal to Noise Ratio (SNR).

The measurement parameter of Brillouin spectroscopy (BS) is the frequency $f_B = {}^{\Omega}/_{2\pi}$ of the acoustic sound waves in the medium. The direction and magnitude of the phonon wave vector is predefined by certain optical scattering geometries. In general, there are several scattering geometries, whereas the mostly known type is the backscattering. Here the q-vector is oriented in backwards direction of the incident light. Further 90A and 90R scattering geometries describe types, where the incoming light and the scattered light have an angle of 90° in between (Figure 43). For the 90A geometry, there is no need of knowledge of the refractive index, what makes it interesting for several applications and combination with other scattering geometries [112-116].

The main part of this work is concerned with the backscattering technique. However, there are experiments attached in the appendix regarding the RIΘA scattering geometry, so it is depicted here as well. For deeper knowledge of the scattering geometries in general, here are some references [117-121]. The first use of the RIΘA scattering geometry [122] and some works regarding this type of scattering geometry can be found in those works [123-125].

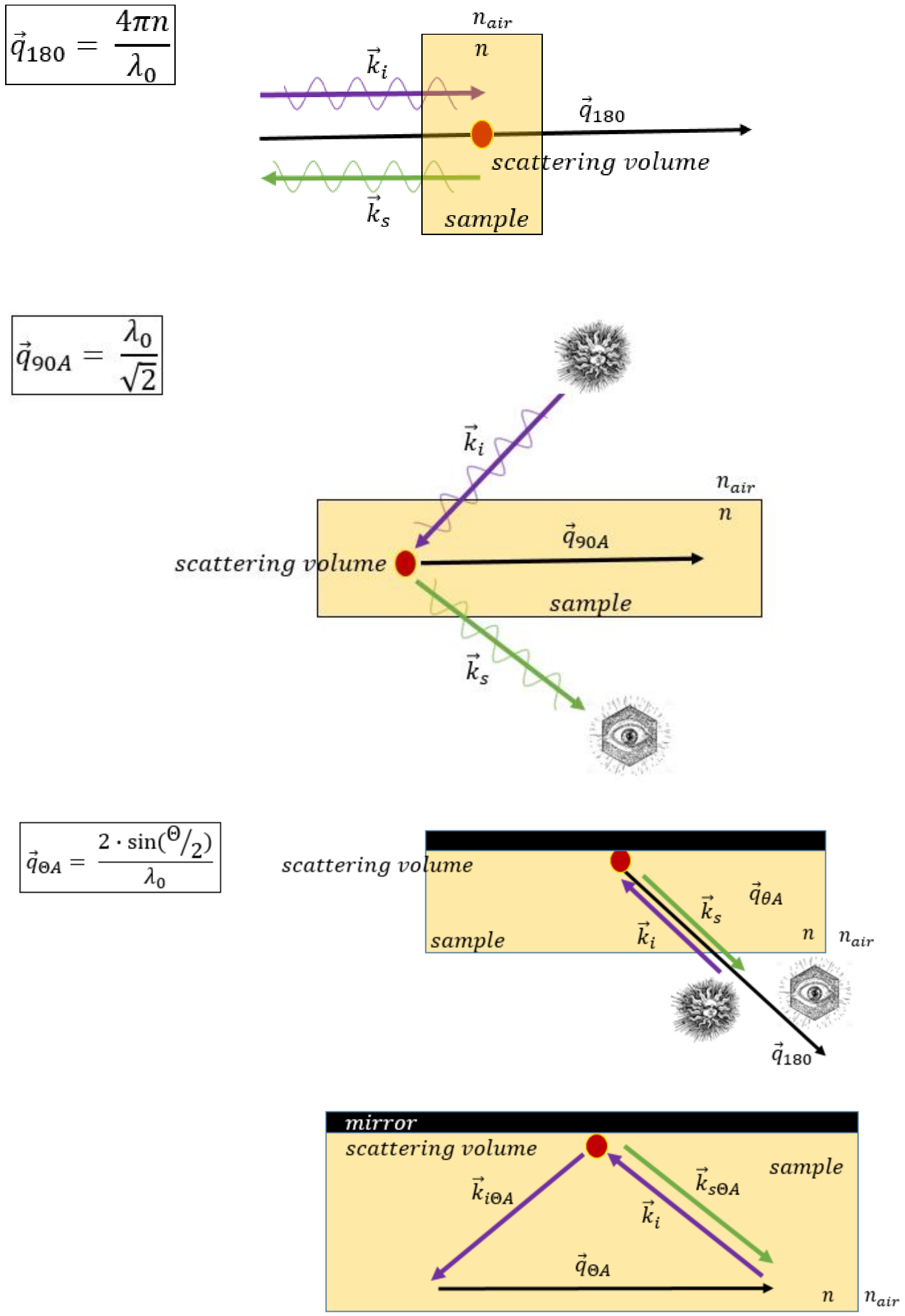

$$\vec{q}_{180} = \frac{4\pi n}{\lambda_0}$$

$$\vec{q}_{90A} = \frac{\lambda_0}{\sqrt{2}}$$

$$\vec{q}_{\Theta A} = \frac{2 \cdot \sin(\Theta/2)}{\lambda_0}$$

Figure 43: Scattering geometries, top back-scattering, middle 90A scattering and both lower show the RIΘA scattering. The red circles indicate the scattering volume onto which the focus of the light beam is set to. For the backscattering 180° the observation is on the same side as from where the light is coming from (reflection). At the 90A scattering (3) the scattered light is observed from the other side of the sample (transmission)y. The RIΘA scattering, using a mirror on the back surface of the sample gives two signals for backscattering and one for the RIΘA which is a special case of 90A (depicted in lower sketch).

Figure 43 gives an overview of the common scattering geometries for Brillouin spectroscopy with corresponding relations to frequency and sound velocity. The incident light is marked with the wave vector $\vec{k}_i$ and the scattered light with the wave vector $\vec{k}_s$. The acoustic wave vector $\vec{q}$ is given for each geometry and its direction, indicated with the black arrow. The special case of RIΘA scattering (which is a combination of back-scattering and 90A scattering) is achieved by using a reflecting surface at the backside of the sample. The red circles indicates the scattering volume, into which the laser beam is focused and the scattering radiates from spherically.

3.2.2 Brillouin Rheology

The idea of Brillouin Rheology is to apply Brillouin scattering in a common rotational rheometer. A shear rate $\dot{\gamma}$ is applied to a sample, while observance with the Brillouin spectrometer.

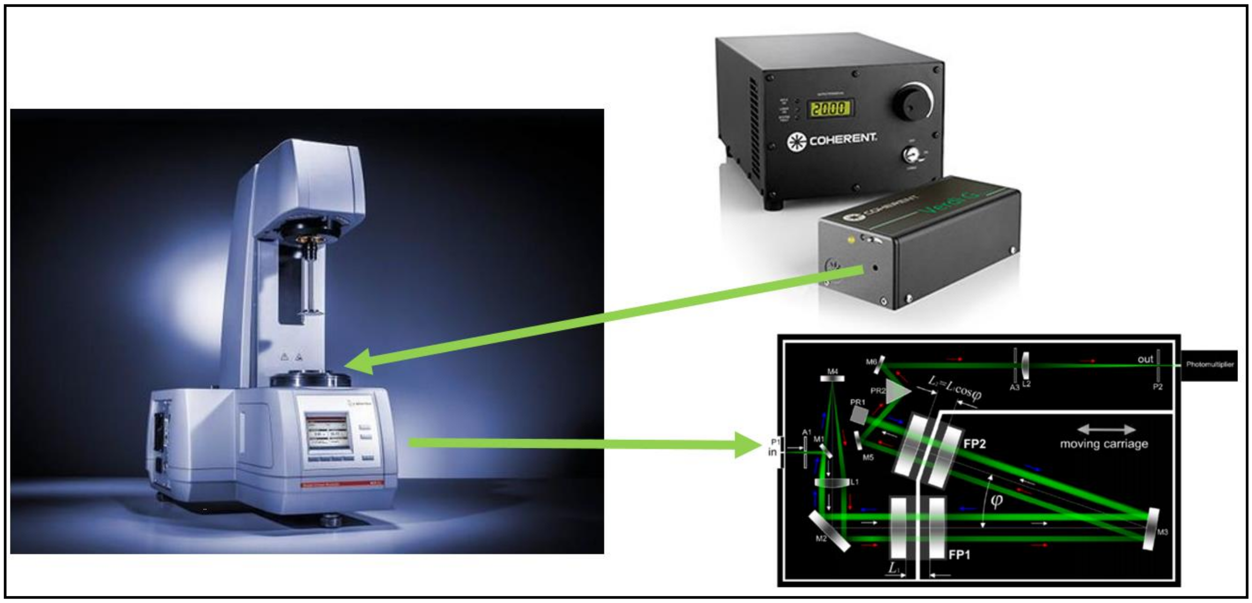

Figure 44: Illustration of the Brillouin Rheology idea. The laser light is lead into the rheometer sample stage and analogically observed with the spectrometer, so the analysis of the sample can be done rheologically and spectroscopically, respectively.

The experiments should give both, the rheological measurement data and the Brillouin spectroscopy values of frequency shifts f_B and following the hyper-sound velocities v_B in the sample volume while shearing. Due to the applied shear field, that gives a viscosity curve or flow curve from the rheometry, the optical analysis should give some deeper inside about structural behavior of the investigated system under flow, which the rheometer cannot show.

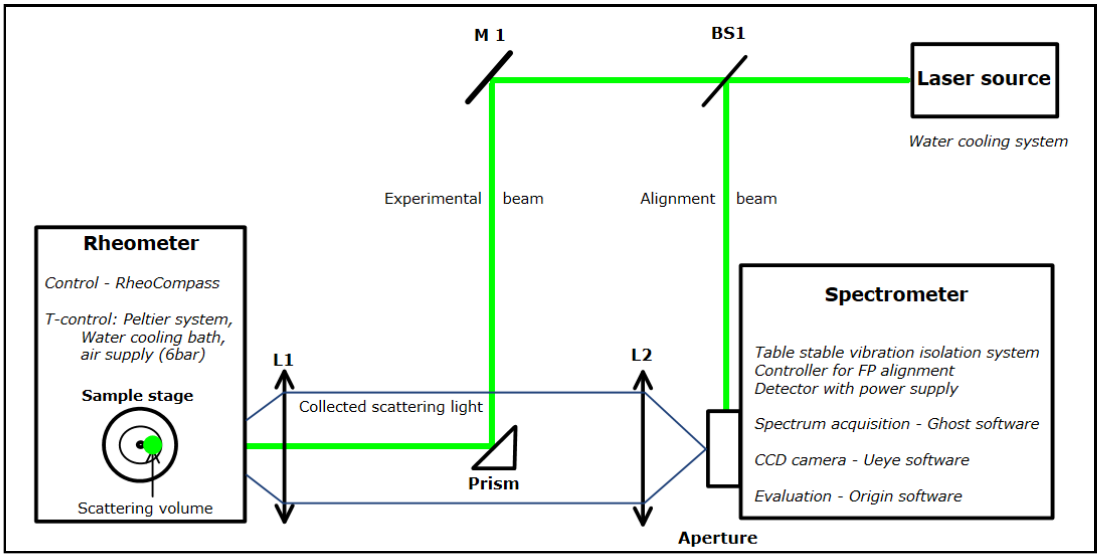

Figure 45: Schematics of a Brillouin Rheology experimental set-up. The three main systems (laser, rheometer and spectrometer) with corresponding elements and software (cursive) are shown with the optical system. The laser beam is lead through a beam splitter (BS1) over the alignment beam path to the side entrance of the spectrometer. The experimental beam path is lead over a small prism into the rheometer sample stage. The scattered light is collected by the detection path (L1 and L2) into the aperture of the spectrometer.

Figure 45 gives an overview about the main parts of the set-up for Brillouin Rheology. The three main systems, the light source (VerdiG2 series from Coherent, 532 nm), the spectrometer (TFP2-HC from Table stable) and the rheometer (MCR302 from Anton Paar) are shown with the corresponding software and system elements. The laser needs an active water-cooling, that has to be kept in maintenance with distilled water. The spectrometer has several system elements to it, (also shown in Figure 1) the active isolation system, the controller, to set the mirror fine alignment and the stabilization. The avalanche photo diode, with its external power control. The spectrum acquisition is acquired with the Ghost software (also from Table stable), installed at a computer. A CCD camera is linked to the aperture of the spectrometer to align the internal prism, for overlaying the alignment and experimental beam path and additionally image the sample volume. The evaluation of the spectra, as well as the rheological data is done with Origin software. The rheometer is controlled by the RheoCompass software (from Anton Paar). The Peltier system for temperature control needs an additional water bath and an air supply, while the rheometer needs also 6 bar air pressure, plugged in, for the bearing of the rotational geometries. The laser beam has to be lead into the side entrance of the spectrometer´s aperture for alignment. Further, the experimental beam path is steered over a beam splitter (BS1) and a mirror (M1) to a very small reflecting prism (about 3*1.5mm) and a focusing (positive) lens (L1) into the sample stage of the rheometer. The scattered light is collected by the same lens and lead over another positive lens (L2) in the main entrance of the spectrometer`s aperture.

The realization of the set-up has to be done in several steps, that has been found, to achieve a very fine adjustment of the optical system. Figure 46 shows a sketch of the first steps with a more detailed view of optical elements necessary for alignment.

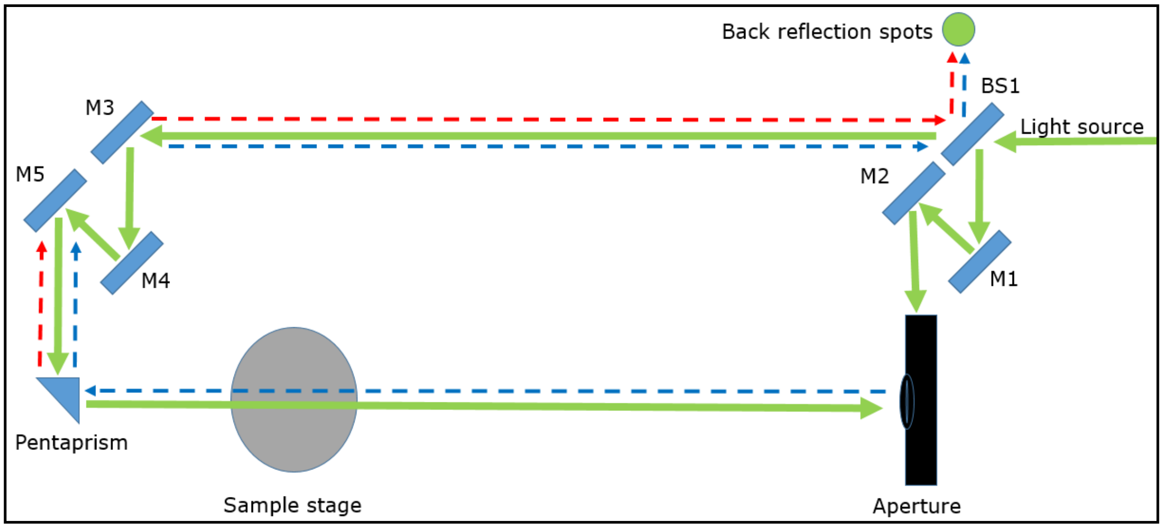

Figure 46: Illustration of the optical alignment for Brillouin Rheology. The laser beam is split (BS1) and steered over two mirrors (M1 and M2) for alignment into the side entrance of the spectrometer`s aperture. The experimental beam path goes over mirrors M3, M4 and M5 onto the pentaprism that leads it in 90° transmission over the indicated sample stage, into the main entrance of the aperture. The pentaprism reflects 4 % of the laser light due to its refractive index, back, which is illustrated with the red dotted line, giving a back reflection spot at a screen. The aperture of the spectrometer is made out of a sheet of iron, in which holes with different sizes are swaged into, so putting the smallest size of 150 µm diameter, it also reflects the main part of the beam back. Those two back reflections are used to set the optical alignment, as both spots get visible at the screen and are overlaid per adjustment of the mirrors and prism.

The optical alignment should be applied with quite long optical paths (as introduced in previous chapter) to ensure a proper optical pathway to the rheometer and the spectrometer, respectively. The optical table is used in its whole dimension for this, as Figure 47 indicates.

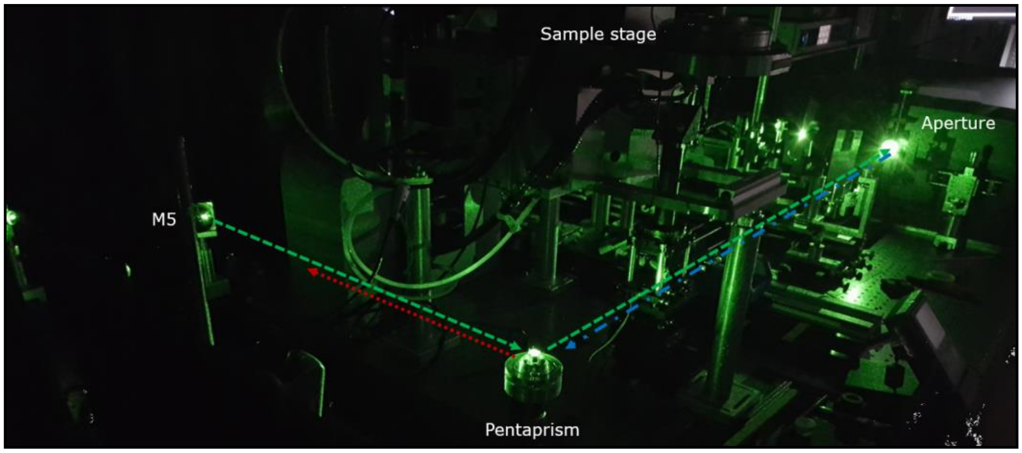

Figure 47: Picture of the optical set-up for alignment of the Brillouin Rheology. As indicated in Figure 46 the experimental beam path is lead over mirror (M5) to the pentaprism that reflects a part of the light back (indicated as red dotted arrow). Further, the beam goes to the aperture of the spectrometer that also reflects a part of the beam back (indicated as blue arrow). Those back reflections are used to align the outer beam path, the pentaprism and the spectrometer. The sample stage, so the rheometer, is placed elevated about 30 cm over the optical table, so the beam path can be steered underneath it and the optics can be set to lead the beam into the sample stage later on.

The beam is lead over the mirror (M3, M4 and M5), which are used to adjust the beam properly onto the pentaprism, that, due to its construction, transmits in an angle of 90°. Aligning the beam with the prism on the aperture of the spectrometer (Figure 48) the back reflection of the aperture can be used for aligning the pentaprism, also reflecting a part of the light back. Those two back reflections can be overlaid at the screen (indicated in Figure 46), which then assures the proper alignment of the mirrors and pentaprism to that point.

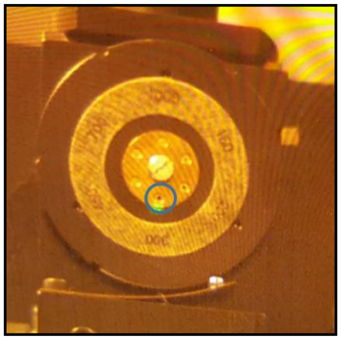

Figure 48: Picture of the spectrometer`s aperture trough laser protection glasses (alignment glasses to be exact, as they let a small part of the laser wavelength through and so allows the optical alignment). The blue circle indicates the laser beam which is set with the pentaprism, to hit the smallest sized aperture, this ensures the proper alignment from prism to spectrometer, as the aperture gives another back reflection that is to be used for the fine adjustment.

The next steps are, to include a second prism (P1) in the beam path that is the one to use for the experiments. Figure 49 gives an overview of those steps for the optical alignment. Mirrors (M6, M7 and M8) are set to steer the beam onto a very small prism (P1) with the dimensions of 1.5 mm * 3 mm. Adjusting this prism, on one hand, to the pentaprism, gives a back reflection (indicated as red arrow) after the beam splitter (BS1) as before. On the other hand, the transmitted beam, which is only to align with the new set mirrors (M6, M7 and M8) and the prism (P1), gives a spot through the backside of mirror M6, if a proper alignment has reached.

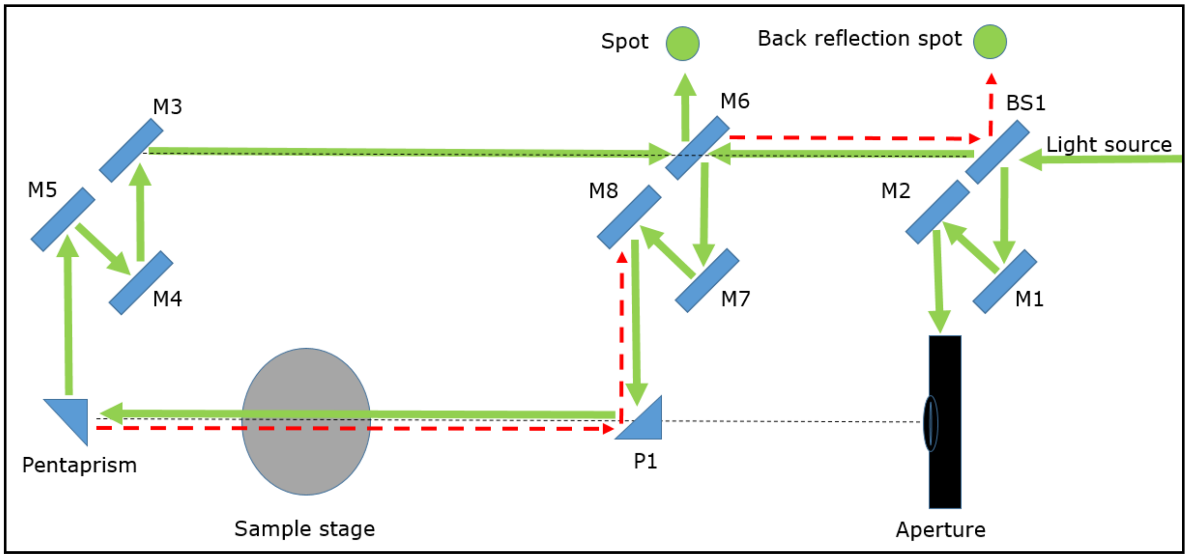

Figure 49: Illustration of the construction of the optical set-up for Brillouin Rheology. Another prism is set on the optical axis between the pentaprism and the aperture of the spectrometer. Mirrors (M6-M8) are installed, to steer the beam over prism P1 and the pentaprism, to give a spot at a screen behind mirror M6. The back reflection of the pentaprism is going to be visible next to the beam splitter BS1 at fine alignment.

Figure 50 gives a picture of the back reflection spots after installing the main prism (P1) for the latter experiments. The spots are visible behind the beam splitter BS1 and the mirror M6, respectively. This mirror M6 can be let down, so the beam goes as before (Figure 46), over mirrors M3-M5 and the pentaprism, in direction of the aperture of the spectrometer.

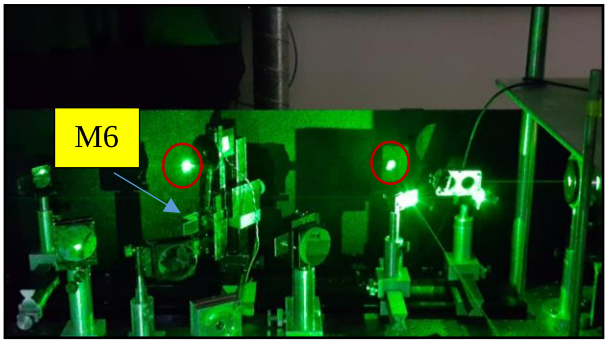

Figure 50: Picture of the back reflections (indicated with red circles) in the screen behind the beam splitter BS1 (from the pentaprism) and the mirror M6 after installing the prism P1 and lowering the mirror M6.

Is there a proper alignment, the new installed prism P1 leads the beam over mirrors M8-M6 onto the screen behind the mirror M6. With this principle it is now ensured that the new prism is well aligned to the optical axis and the spectrometer's aperture as well.

Having achieved the proper pre alignment of the optical set-up, now the rheometer has to be aligned. A mirror M9 is set at the position previously marked as sample stage, which is exactly beneath the rheometer sample stage. The laser beam is lead 90° orthogonally upwards to the x-y axis of the optical axis on the table. The beam is now entering the rheometer sample stage from below through the glass ground plate and is reflected back by the glass plate as well as the plate-plate geometry of the rheometer as pictured in Figure 51. These back reflections can now be used to level and adjust the rheometer perfectly in its lot and align it to the spectrometer.

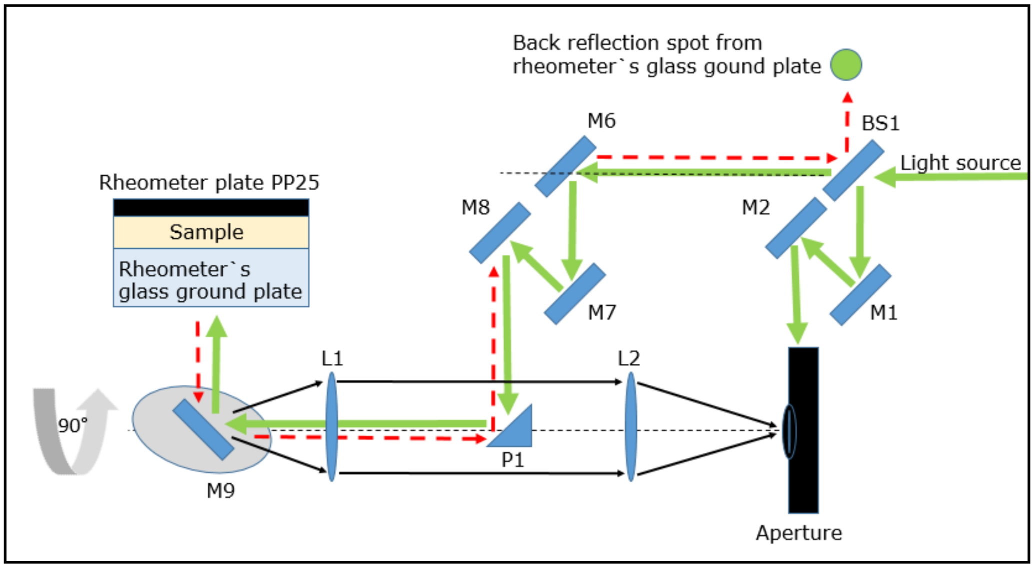

Figure 51: Illustration of the optical set-up for Brillouin Rheology, installing the rheometer. A mirror M9 is placed at the sample stage position below the rheometer and is used to steer the beam 90° orthogonal to the optical axis

upwards, towards the rheometer glass ground plate. Entering the sample volume, the beam gets reflected by the rheometer geometry PP25, as well as from the glass ground plate. These back reflections, again, shall be used to align the rheometer to the optics and the spectrometer. The detection beam path (indicated with the black arrows), leads the scattered light over lens L1 to lens L2, which focus the light into the aperture of the spectrometer.

Having this achieved, one can now start to align the detection path. Indicated with the black arrows in Figure 51, the scattered light is collected by lens L1 and focused into the aperture of the spectrometer with lens L2. For the calibration, one can use a ring pattern, printed smallest possible onto a sheet of transmissible film. Setting this at the central position of the glass ground plate of the rheometer and lighten it up from the background, the optics will image this pattern into the aperture of the spectrometer, which can be observed with the Ueye software that pictures the entrance aperture via a CCD camera. With this method the pre-alignment is pretty well done. The focal position in x-y dimension and in z direction is now quite clear. Letting the laser beam enter, one can calibrate the laser spot to the image as pictured in Figure 52. The beam has to be set in the center of the pattern, as it is centered at the glass ground plate, so sample stage of the rheometer. The ring pattern has to be set to a sharp image (mainly with lens L2) and the focal spot to minimum diameter, with lens L1, so the plane of image of the ring pattern lies on the focal plane of the laser beam.

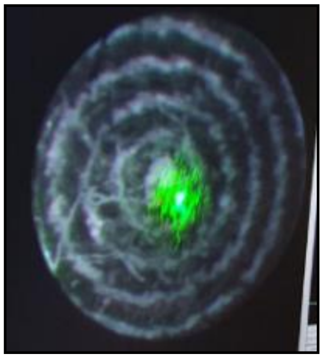

Figure 52: Picture of the ring pattern fixed on the rheometer ground plate and illuminated from the backside with divergent light, to image it, in the aperture of the spectrometer and picture it with the Ueye software and the CCD camera, installed at the aperture. The laser beam is lead to the sample stage and is so visible as well.

Chapter 4: Development of a Brillouin Rheology Set-up

This section introduces the backscattering approach of Brillouin light scattering in the rheometer`s sample stage, while researching the temperature regime and the shear rate behavior of a polymer solution.

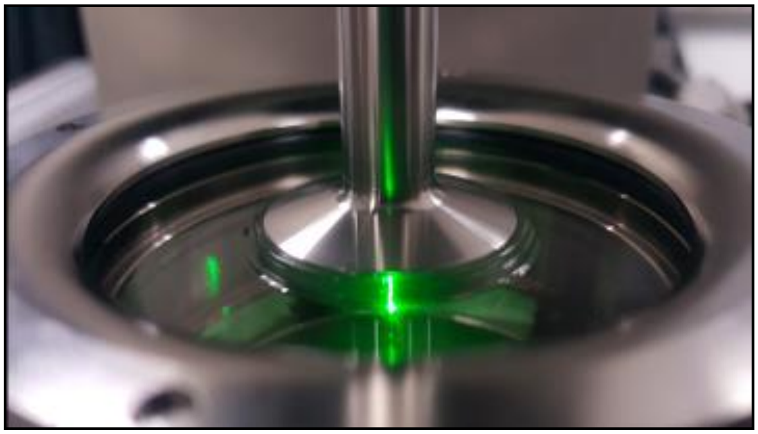

Figure 53: Picture of the rheometer sample stage with a loaded sample and an applied high shear rate. The scattering volume at central position (green laser beam in the middle of the rheological plate-plate geometry).

Figure 53 shows the Rheometer glass plate and the PP25 geometry having a loaded sample and a laser beam in central position. The final experimental set-up for the combination of rheology and Brillouin spectroscopy with backscattering is shown in Figure 54.

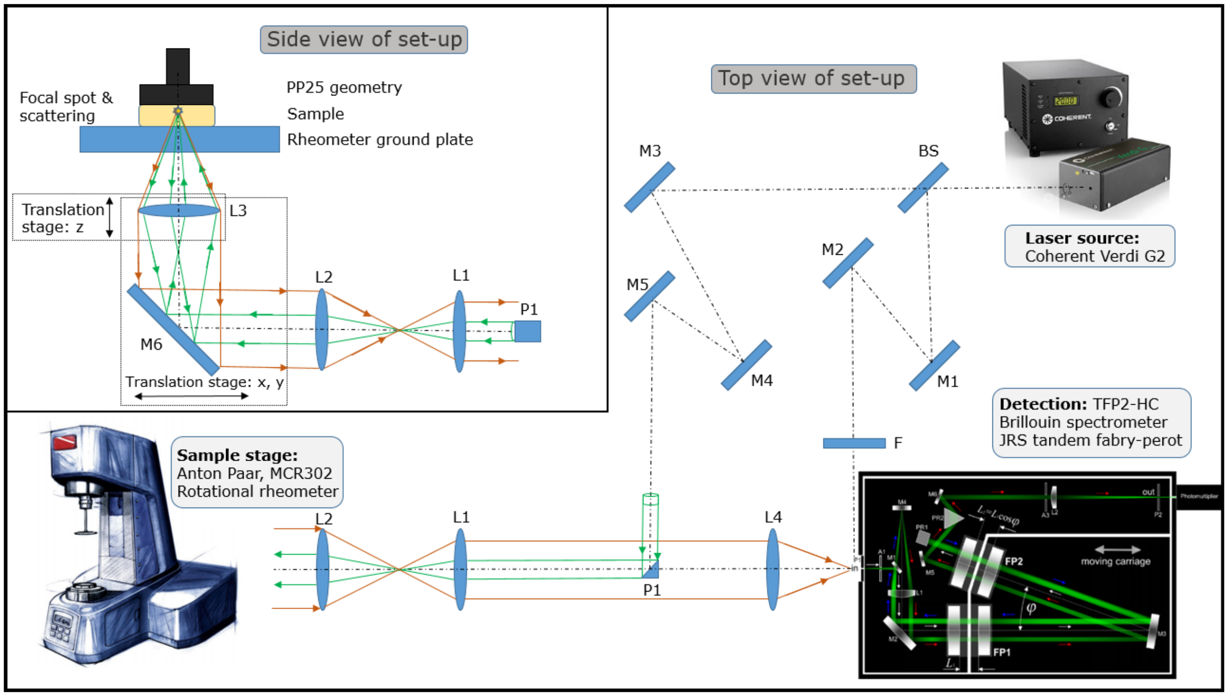

Figure 54: Illustration of the experimental set-up for Brillouin Rheology with backscattering geometry. The main components are the laser light source (532 nm), the rotational rheometer (MCR302 from Anton Paar) as sample stage of the rheometer and the tandem Fabry-Perot spectrometer to apply Brillouin scattering. (BS: beam-splitter, M: mirrors, F: intensity filter, P: prism and L: lenses.) For more information, see text.

One part of the laser beam is directed onto prism P1 used to implement 180° backscattering. The beam is expanded with telescope optics (lenses L1 and L2) to reach smaller focal parameters in the latter. Mirror M6 reflects the expanded beam upwards to the rheometer sample stage. In front of the ground glass plate of the rheometer`s sample stage an objective lens L3. It is mounted on a translation stage CT1, in order to be able to move the focal point along the optical axis in z-direction (see later). In order to exclude direct reflections from the different optical surfaces in the rheometer set-up, the incoming laser beam (green lines) is slightly tilted by 4° with respect to the surface normal of the rheometer plates, as discussed more in the latter. The detection path, indicated with red lines, starts from the scattering volume and is collected by the objective lens L3. The scattered light is lead over the prism (which cuts out a part) to the ocular lens L4, which projects it onto the entry aperture of the spectrometer.

The following subsections are mainly three-parted; first, the development of the fitting optics and mechano-optical set-up to deliver the best results. Tests are implemented with an 80 mm focusing lens (L3) to study the viscosity over shear rate and for comparison, rheological investigations. As the rheometer hard cover and elements, like the Peltier element for tempering, gives limiting conditions for the adjusting of the opto-mechanics the 80 mm focusing lens is chosen for the investigation. The viscosity to shear rate behavior is studied as well as a scan of the Brillouin shift frequencies in variation of the y-plane and the z-plane position (the height) of the scattering volume in the sample. Rheological investigations are done regarding stability of the viscosity over time. However, the focusing lens is changed to 100 mm for more detailed investigation, then 60 mm, which is the very smallest focal length lens to install, to investigate, and get a better understanding of the position of the scattering volume in the sample via the measurement itself. Secondly, an experimental series for three different radial positions in the sample volume is implemented to gain more knowledge about necessary parameters of the set-up and the experiments itself. The third part shows the final experimental series and corresponding data for the previous described experiments and gives a comparison of the Brillouin shift frequencies for temperatures, shear rates and different radial positions of the scattering volume.

4.0.1 First experimental approach of BR with 80 mm focusing optics

The objective lens (L3, Figure 54) has a focal length of 80 mm, the scattering volume is set 2 mm away from the edge of the geometry as it is expected to have the most impact at the edge of the geometry, which is set to a gap size of 0.5 mm. The laser is set to 11 mW (at the sample stage). First, fast Brillouin spectroscopy measurements are executed for different shear rates $\dot{\gamma}$ (0 s^{-1}, 100s^{-1}, 1000 s^{-1} and 5000 s^{-1}) for the investigation of the material and are plotted in Figure 55 with the rheological acquired values of the viscosity η, at room temperature of 23°C.

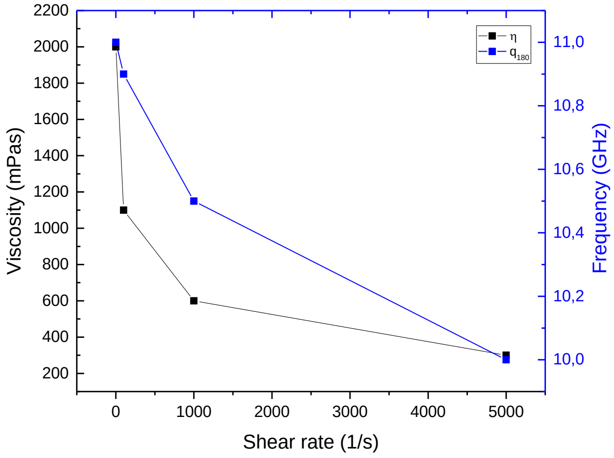

Figure 55: Viscosity η and Brillouin shifts q_{180} over shear rate $\dot{\gamma}$ for the sample PVP 2.5 mass percent PEG in a 0.5 mm gap, at edge position, for room temperature (23°C).

Shear thinning behavior is recognizable with the rheological measurements. The Brillouin spectroscopical measurements picture this as well (also see Table 2).

Table 2: First experimental results for BR of the PVP 2.5 mass percent PEG polymer solution for different applied shear rates $\dot{\gamma}$ in a 0.5mm gap and the rheologically acquired values of viscosity η, as the spectroscopically acquired values of Brillouin frequency shifts, for q_{180} backscattering, with a 80mm focal lengths objective lens, at room temperature (23°C).

Shear rate $\dot{\gamma}$ (s^{-1})	**Viscosity η (mPas)**	**Frequency f_{q180} (GHz)**
0	2000	11
100	1100	10.9
1000	600	10.5
5000	300	10

The measurement looks promising, so it is repeated with more values for the shear rates $\dot{\gamma}$ (0 s^{-1}, 10 s^{-1}, 100 s^{-1}, 1000 s^{-1}, 1500 s^{-1}, 3000 s^{-1} and 5000 s^{-1}) and an acquisition time of 2.5 min.

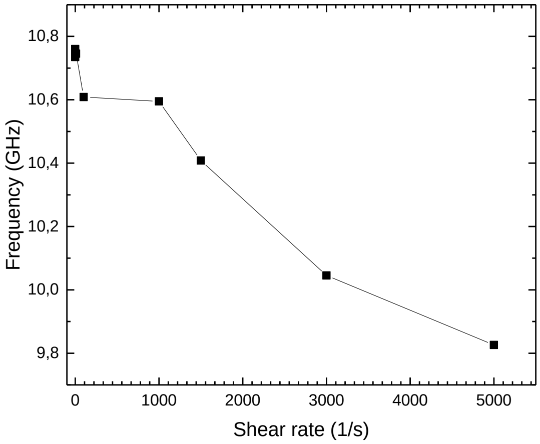

Figure 56: Backscattering Brillouin shift frequencies $f_{q_{180}}$ over shear rate $\dot{\gamma}$ for the PVP 2.5 mass percent PEG sample in a 0.5 mm gap at room temperature (23°C).

The measurement values for zero shear, 10 s^{-1} and 100 s^{-1} shear rate, lie next to each other. Starting with a shear rate $\dot{\gamma}$ of about 1000 s^{-1} the frequency decreases with increasing shear, so shear thinning behavior is approved (Figure 56, Table 3) and pictured as well with the Brillouin spectroscopy.

To investigate the sample material PVP 2.5 mass percent PEG, a flow and viscosity curve is recorded with the polished PP25 geometry at 25°C and a gap size of 0.5 mm. The corresponding plots are shown in Figure 57.

Table 3: Experimental results of Brillouin Rheology of the PVP 2.5 mass percent PEG sample in a 0.5 mm gap, for different applied shear rates $\dot{\gamma}$ and the rheological acquired values of viscosity η, as the spectroscopically measured values of back scattering Brillouin frequency shifts $f_{q_{180}}$, with corresponding signal heights, for the 80mm focal length objective lens, at room temperature (23°C).

Shear rate $\dot{\gamma}$ (s^{-1})	**Viscosity η (mPas)**	**Frequency $f_{q_{180}}$ (GHz)**	**Signal height (counts)**
0	-	10.76	214.3
10	830	10.746	254.6
100	680	10.609	288.5
1000	475	10.595	318.5
1500	370	10.408	289.5
3000	270	10.046	315
5000	210	9.826	335.5

The flow and viscosity curves (Figure 57) confirm that this sample shows a shear thinning behavior at a temperature of 25°C, so it is interesting to investigate this in more detail.

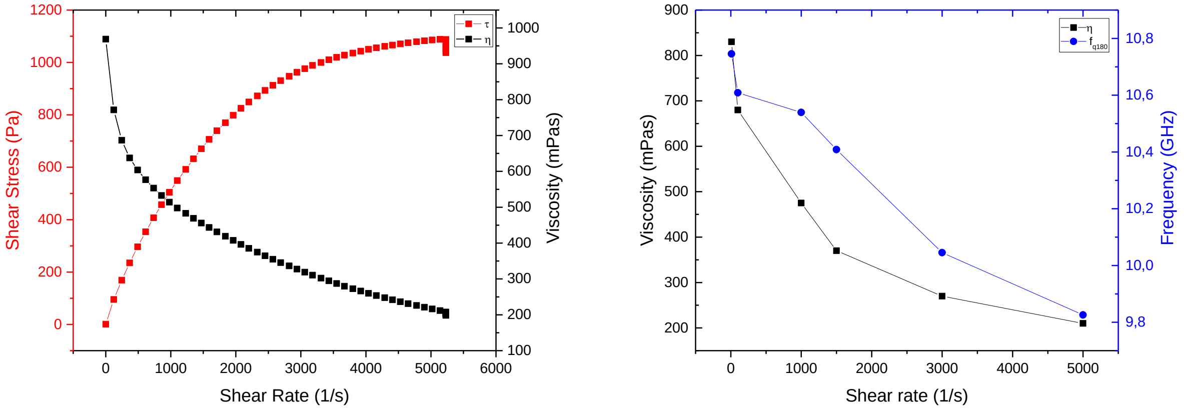

Figure 57: Left, flow (red) and viscosity η (black) curve of the PVP 2.5 mass percent PEG sample in a 0.5 mm gap, at 25°C. Right, the measured viscosity (black) and Brillouin shifts $f_{q_{180}}$(blue dots) over shear rate $\dot{\gamma}$.

To gain a bit more freedom of space for the optical set-up under the rheometer, a lens with wider focal distance is chosen for further measurements.

4.0.2 A study with a 100 mm focusing optics

In the following, a new sample of the PVP 2.5 mass percent PEG solution has been tested with the Brillouin Rheology method. The objective lens has a focal length of 100 mm and is chosen to gain more space with the opto-mechanics, to position the scattering volume that is set to be 3 mm from the edge of the geometry. The gap size is set to 0.5 mm, the laser is applied with 26.5 mW and Brillouin spectra are collected (2.5 min) for several shear rates $\dot{\gamma}$ (0, 1 s^{-1}, 10 s^{-1}, 1000 s^{-1}, 2000 s^{-1}, 3000 s^{-1}, 4000 s^{-1}, 5000 s^{-1}, 6000 s^{-1}) at 25°C and plotted in Figure 58.

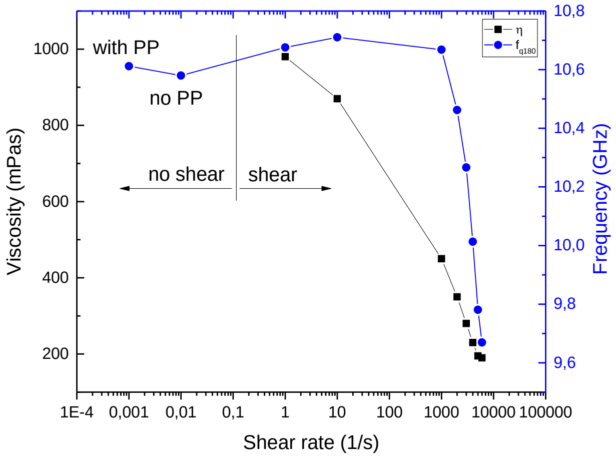

Figure 58: Measured viscosity η values and Brillouin shift frequencies $f_{q_{180}}$ over shear rate $\dot{\gamma}$ for the PVP 2.5 mass percent PEG sample in a 0.5 mm gap, with a 100 mm objective lens, at 25°C. The measurement points on the left show spectral values with and without the PP25 without shear. To the right, the applied shear, with corresponding measurement values for viscosity (from rheometer) and frequency (from spectrometer) are shown.

The rheologically measured values of viscosity for the sample are depicted in Figure 58 (black squares) and show, again, the shear thinning behavior. Regarding the Brillouin shifts (blue dots), the first measurement values are with and without the PP plate and show a minor variation. From shear rate $\dot{\gamma}$ of 1 s^{-1} to about 1000 s^{-1} the Brillouin frequency shifts for $f_{q_{180}}$ stay somewhat constant, but increase then strongly. This implies that the Brillouin Rheology can depict the variation in viscosity of the sample (corresponding measurement values in Table 4).

Table 4: Experimental results of Brillouin Rheology of the PVP 2.5 mass percent PEG in a 0.5 mm gap, for different applied shear rates $\dot{\gamma}$ and the rheologically acquired values of viscosity η, as the spectroscopically acquired values of Brillouin frequency shifts $f_{q_{180}}$for a 100 mm focal length objective lens, at 25°C temperature.

Shear rate $\dot{\gamma}$ (s^{-1})	**Viscosity η (mPas)**	**Frequency $f_{q_{180}}$ (GHz)**
0.001		10.612
0.01		10.58
1	980	10.676
10	870	10.710
1000	450	10.668
2000	350	10.462
3000	280	10.267
4000	230	10.013
5000	195	9.781
6000	190	9.67

Plotting the shear rate regime of the measurement sequence just from 1000 s^{-1} to the maximum shear, results in the following plot (Figure 59).

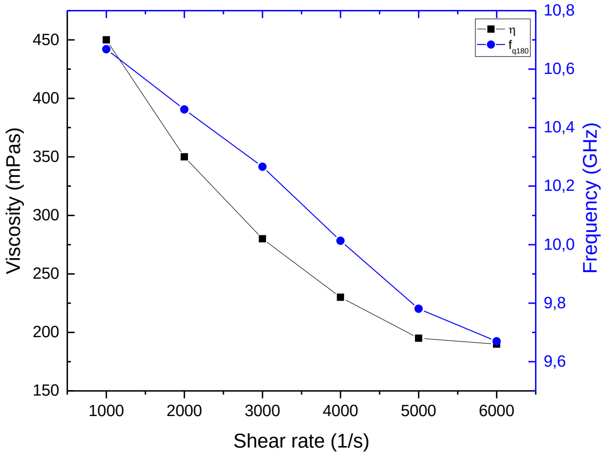

Figure 59: Measured viscosity η (with rheometer) and Brillouin shift frequencies $f_{q_{180}}$ over shear rate $\dot{\gamma}$ for the PVP 2.5 mass percent PEG sample in a 0.5 mm gap with a 100 mm focal lengths objective lens, at 25°C. The shear rate regime is from 1000 s^{-1} to 6000 s^{-1}.

The shear thinning of the material is coherent to the decrease in Brillouin shift frequencies for q_{180}. For the further measurements, the higher shear rates seem to be of interest. The Brillouin shifts show peculiar behavior after stopping the rheological measurements, but further collecting spectra. This might imply some relaxation effects in the material that will be investigated and discussed in more detail later. Now, the position of the scattering volume is changed horizontally and vertically, to study the effect of the position of it, in the sample volume.

4.0.2.1 Positioning of the scattering volume

A **scan over the y-axis** (radial position) in the sample is implemented. The scattering volume is translated from outside into the sample volume and is approaching the edge of the sample (rheo-geometry) as illustrated in Figure 60, respectively. The positioning with the opto-mechanical translation stage is measured from the moment the laser beam is hitting the PP25.

The Brillouin shift frequencies and values for viscosity are measured analogy and plotted in Figure 61. (The Brillouin frequency shift values for the edge position might be influenced by edge effects.) The gap size is set to 0.5 mm at 25°C with an applied shear rate $\dot{\gamma}$ of 3000 s^{-1} and an acquisition time of 3 min is applied.

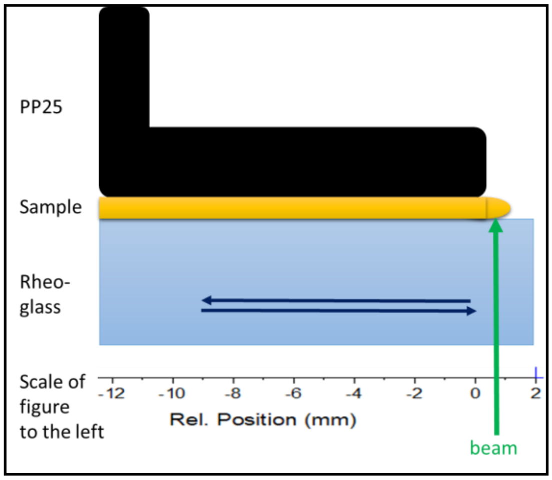

Figure 60: Illustration of the experimental approach of a y-scan. The laser beam, so the scattering volume, is translated from outside the sample (radial) in direction to the center. The Brillouin spectra start to show signal as the sample is reached. Setting the scattering volume at the edge of the PP25 and translating a certain distance in direction to the center of the sample (stage).

The Brillouin shift frequencies are decreasing over the radial position direction to the edge of the geometry of about 0.1 GHz, as the rheometer shows quite constant values for viscosity of about 270 mPas. This indicates that the inhomogeneous shear field in the sample for a plate-plate rheological geometry is possible to picture with Brillouin Rheology method.

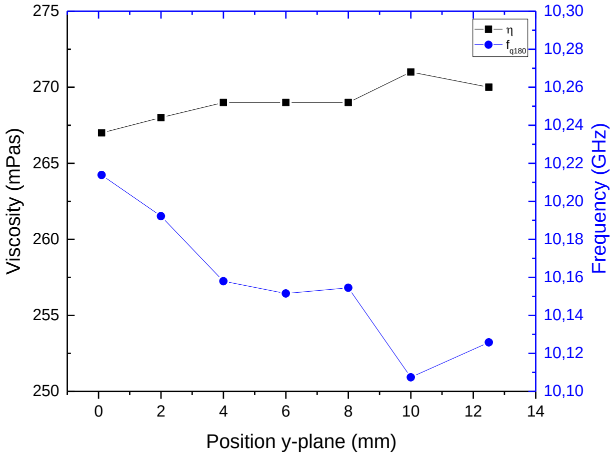

Figure 61: Viscosity η and Brillouin shifts $f_{q_{180}}$ over radial position in y-direction for the PVP 2.5 mass percent PEG sample in a 0.5 mm gap at 25°C.

As a next step, **a z-scan** (height of the sample volume) is implemented for the sample at a radial position of 2mm from the edge of the sample (by translating the opto-mechanical stage of the objective lens L3 in Figure 54). The Brillouin shift frequency for backscattering q_{180} measured at zero shear, is about 10.65 GHz in average, while applying 3000 s^{-1} the value shrinks to about 10.075 GHz.

Figure 62 shows the z-scan with the 100 mm focal distance objective lens for the PVP 2.5 mass percent PEG sample, in a 0.5 mm gap, at 3000 s^{-1} shear rate. The focus of the lens is translated from the lower glass plate-sample-interface upwards.

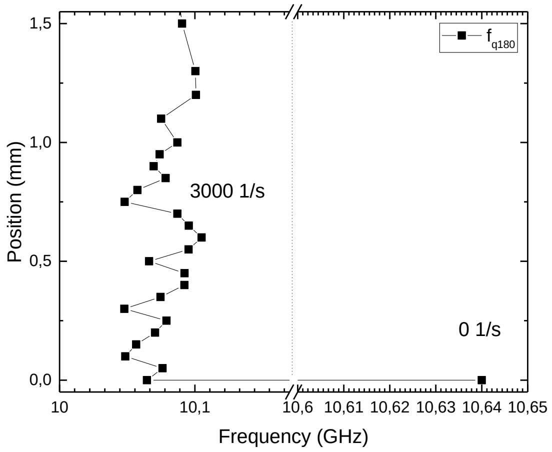

Figure 62: Scattering volume position in z-direction for the PVP 2.5 mass percent PEG sample, at 3000 s^{-1} shear rate $\dot{\gamma}$ over the Brillouin shift frequencies $f_{q_{180}}$ with a 100 mm focal distance lens. The value to the right is without applied shear rate.

The mainly visible difference is the Brillouin frequency shift from zero to 3000 s^{-1} shear rate $\dot{\gamma}$. The position in z-direction does not give much information, yet.

As the measurement values are not expressive enough the optics are changed to a 60 mm objective lens later, but first, some rheological studies are implemented and depicted to investigate the material behavior over time.

4.0.3 Rheological investigations of the PVP 2.5 mass percent PEG sample

To get a better picture of the rheological behavior of the system, long time measurements of viscosity η over time (Figure 63) are implemented.

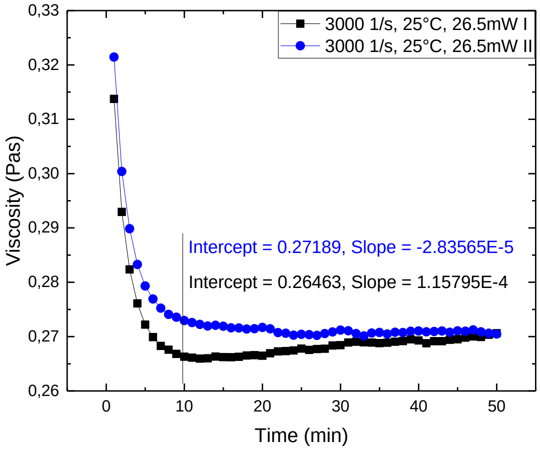

Figure 63: Two viscosity curves for the PVP 2.5 mass percent PEG sample in the 0.5 mm gap, at 25°C, with 3000 s^{-1} *shear rate* $\dot{\gamma}$.

The gap size is 0.5 mm, with a set temperature of 25°C and an applied shear rate $\dot{\gamma}$ of 3000 s^{-1}. The laser beam is entering the sample volume (to assure same conditions as in the latter experiments) and two measurements are executed after each other to see how the material behaves.

It implies that the viscosity η of the second measurement is faster in a stable regime than the first time the material is used. This indicates, that there are some relaxation effects. The calculated average value for viscosity from 10 min to 50 min is for the first run 268.114 mPas +-2.496 mPas, whereas the second series gives 271.075 mPas +- 1.875 mPas.

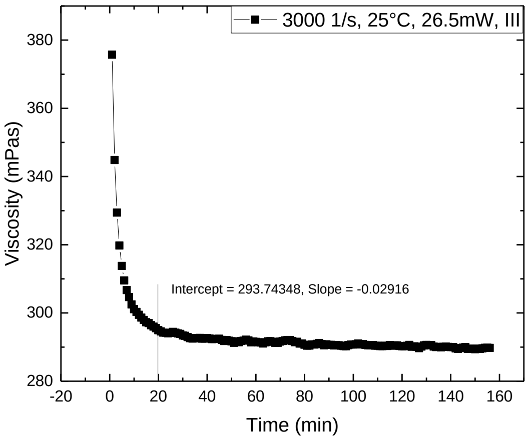

Figure 64: Viscosity η over time for the PVP 2.5 mass percent PEG sample in a 0.5 mm gap, at 25°C, for 3000 s^{-1} shear rate $\dot{\gamma}$ and an acquisition time of 160 min. The laser power at the sample stage is 26.5 mW.

The long time experiment with an applied shear rate $\dot{\boldsymbol{\gamma}}$ of 3000 s^{-1} and a gap size of 0.5 mm for the PP25 is repeated for more than 2 hours with the laser hitting the sample with 26.5 mW. Figure 64 shows the measurement and the fitted value for the average viscosity after 20 min.

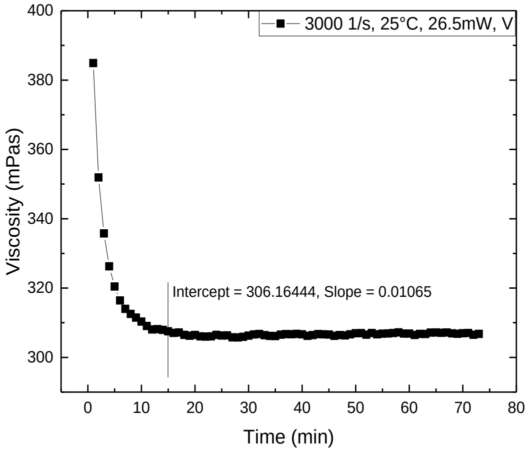

Figure 65: Viscosity values over time for the PVP 2.5 mass percent PEG sample in a 0.5 mm gap to find a proper pre-running time of the rheometer before an experiment is started. The time is 70 min for 3000 s^{-1} applied shear rate $\dot{\gamma}$.

The calculated average value of the viscosity η after 20 min is 291.15 mPas +- 3.44 mPas.

In order to find a proper pre-running time for the rheometer before a spectroscopical measurement is implemented, measurements are made for 70 min time-period (Figure 65). The calculated average value of viscosity η from 15 min to 70 min is 306.62 mPas +- 0.88 mPas.

As the values are variating to each other slightly a measurement sequence for up to 16 hours is implemented and shown in Figure 66.

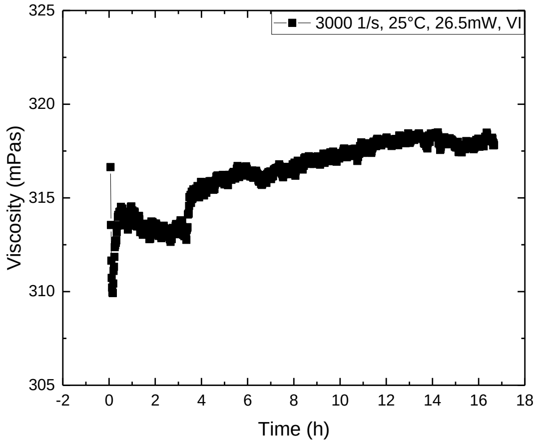

Figure 66: Long time measurement of the PVP 2.5 mass percent PEG sample in a 0.5 mm gap, at 25°C temperature, with 26.5 mW laser power hitting the sample, and 3000 s^{-1} applied shear rate $\dot{\gamma}$.

Principally, the viscosity values are quite constant as they increase from about 310 mPas to 320 mPas, as the fitted average value over the whole measurement time is 316.37 mPas +- 6.45 mPas.

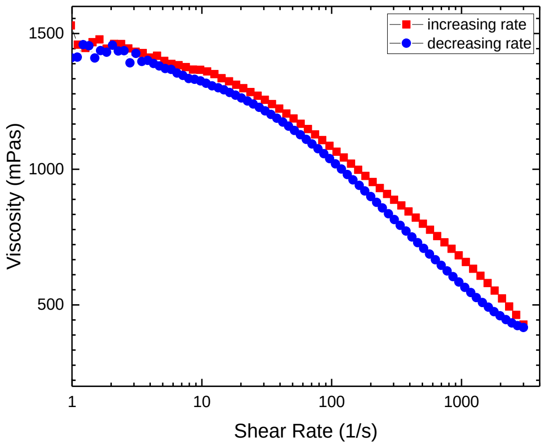

Figure 67: Viscosity curve of the PVP 2.5 mass percent PEG sample in a 0.5 mm gap at room temperature (21°C).

This rheological experiments lead to the decision that a pre running time of the rheometer (after some change of parameter like shear rate) is minimal 15 min, before Brillouin spectra shall be recorded. The constancy of the values of viscosity for the sample might be increased by minimizing evaporation effects and heating of sample.

The rheology, so the viscosity curves for an increasing and decreasing shear rate ramp (meaning de/increase of shear rate, step by step) of the PVP 2.5 mass percent PEG sample in a 0.5 mm gap at room temperature of 21°C, are retested, and plotted in Figure 67.

The viscosity curves behave like in previous experiments. The higher viscosity values at the beginning may result from 4°C cooler temperature as well as a new sample is used.

4.0.4 Final investigations with 60 mm focusing optics

To more deeply investigate the behavior of the sample material regarding shear rate and the radial position of the scattering volume a y-scan is implemented with a shorter focal length objective lens.

The Brillouin shifts in y-axis direction are recorded for 3 min (retests with 14 min) and implemented for zero shear and a shear rate $\dot{\gamma}$ of 3000 s^{-1} in the middle z-position of the sample (0.25 mm gap size position) and are plotted in Figure 68.

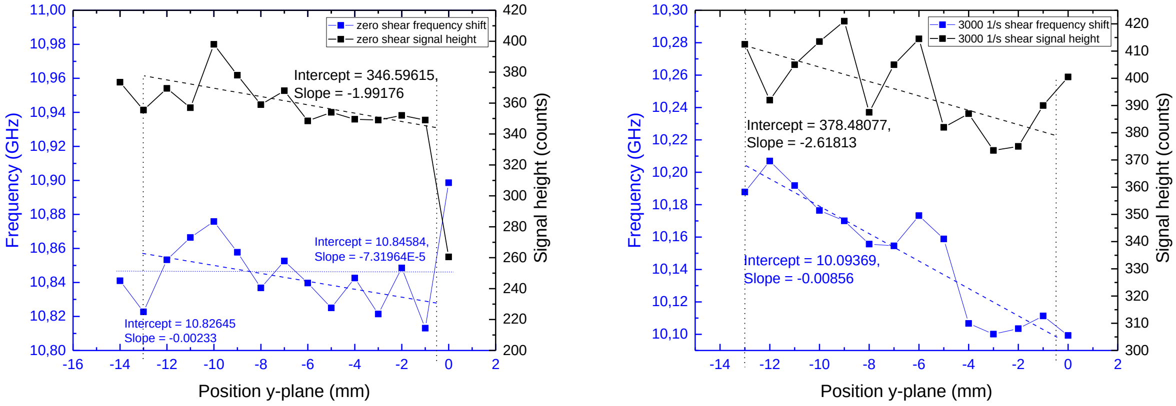

Figure 68: Brillouin shift frequencies $f_{q_{180}}$over radial position of the scattering volume in y-direction, left for zero shear, right applied 3000 s^{-1} shear rate $\dot{\gamma}$ at room temperature (21°C). The intercept and slope values are fitting values from Origin and indicated with dotted lines.

The Brillouin frequency shift values for q_{180} lie between 10.88 GHz and 10.82 GHz for zero shear and 10.2 GHz and 10.1 GHz for the 3000 s^{-1} applied shear rate $\dot{\gamma}$. The comparison of zero shear to 3000 s^{-1} shear rate and the Brillouin frequency shifts to the radial position might indicate that the inhomogeneous shear field can be pictured. The Brillouin shift frequencies increase to inner radial position, where smaller velocities of the sample in the PP in are present. This will be discussed in the corresponding chapter in the latter.

The **z-scan**, using an objective lens with a focal length of 60 mm, is chosen, as it is the one, which just fits the opto-mechanical boundaries of the set-up. The rheometer construction (lower glass plate holder and Peltier tempering elements) define those. The gap size is set to be 0.5 mm at 25°C. The laser power approaching the sample is 25 mW and spectra are collected for 2.5 min acquisition time, for zero shear. The focal spot position is translated upwards from the lower glass plate of the rheometer in direction to the upper PP25 plate. Measuring the Brillouin shift frequencies for $\boldsymbol{q_{180}}$ backscattering, reflecting effects occur, as the frequency shifts are not indicating the position of the sample properly (Figure 69, left). As the laser beam is reflected from the polished PP25, it will start to go downwards after reaching the interface area between sample and PP25, going upwards with the objective lens, so there is no real indication where the sample starts or ends. On the other hand, plotting the signal height values of the spectral peaks to the position of the scattering volume in the sample, it seems to give some indication (Figure 69, right).

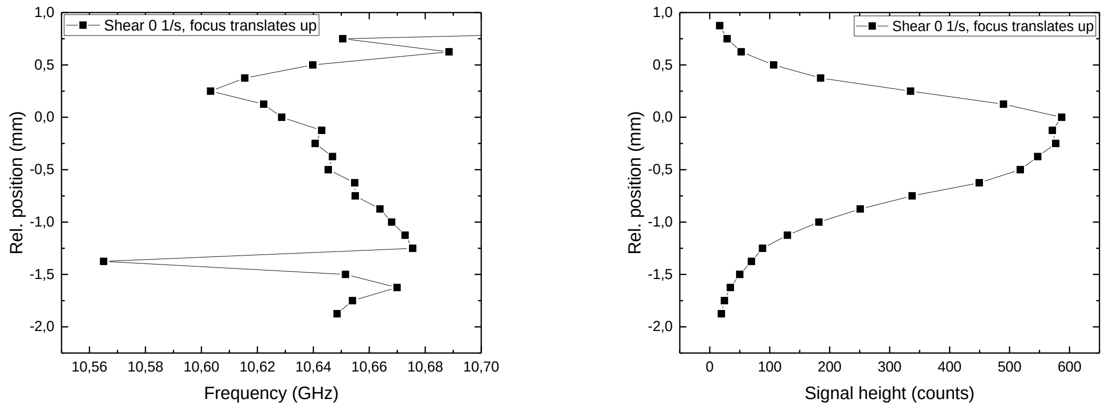

Figure 69: Position of the scattering volume (focal spot) in z-direction over Brillouin shift frequencies $f_{q_{180}}$*, left; right, the signal height values, for the PVP 2.5 mass percent PEG sample, in a 0.5 mm gap, at 25°C for zero shear.*

The progression of the signal height is promising as it shows an area of maximal signal in a distance of 0.5 mm, what most probably is the sample volume height. Due to reflections of the PP25 the Brillouin shift frequencies cannot really give information about the distinct position of the scattering volume in the sample for this fast tests, but the method (the use of signal height values of the Brillouin peaks) seems to be able. However, for further comparison, a shear rate $\dot{\boldsymbol{\gamma}}$ of 3000 s^{-1} is applied and the experiment is repeated with an acquisition time of 2 min per spectra. The focal spot is translated downwards from the last position (previous measurement) and the resulting plot is shown in Figure 70.

The average value for the Brillouin shift frequency $f_{q_{180}}$ for zero shear is 10.655 GHz +- 0.195 GHz and for 3000 s^{-1} applied shear rate $\dot{\gamma}$ is 10.053 GHz +- 0.172 GHz, so there is a difference of about 0.6 GHz visible, as well as a difference in form of the Brillouin spectra. For zero shear, the frequency increases in the middle regime of z position, whereas at 3000 s^{-1} shear, it seems more balanced.

Nevertheless, plotting the signal height values next to the Brillouin shift frequencies gives information about the position of the scattering volume, as it appears, in between the rheological plate geometries.

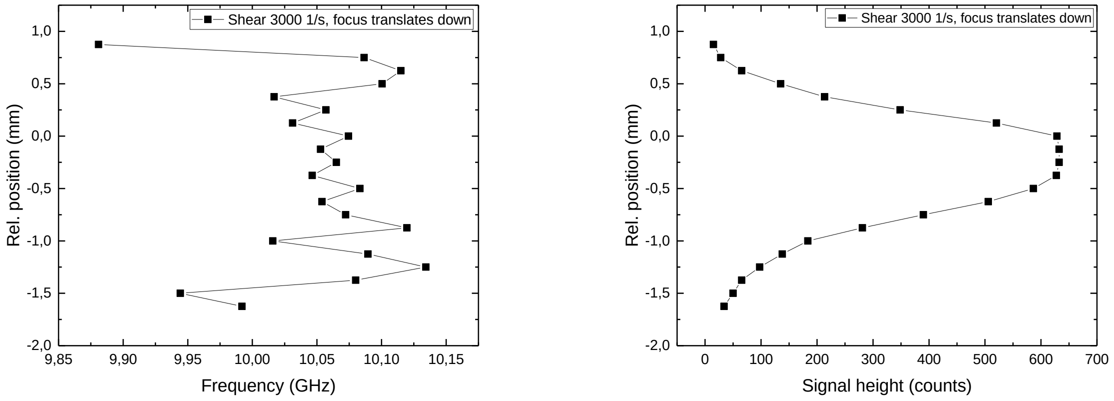

Figure 70: Position of scattering volume in z-direction over Brillouin frequency shifts $f_{q_{180}}$, left; right, the corresponding signal height values for the PVP 2.5 mass percent PEG sample in a 0.5 mm gap, at 25°C, for 3000 s^{-1} shear rate $\dot{\gamma}$.

The measurement is repeated, the focal spot position is translated in upward direction with 3000 s^{-1} shear rate in the regime of interest (z position), which is indicated beforehand by the highest signal height values. The shear rate $\dot{\gamma}$ is set to be 3000 s^{-1} at 25°C sample temperature and a laser power of 25 mW reaching the sample. The acquisition time of the spectra is now 4.5 min. The data of the position of the scattering volume in z-direction in regard to the Brillouin frequency shifts and signal height values are plotted in Figure 71.

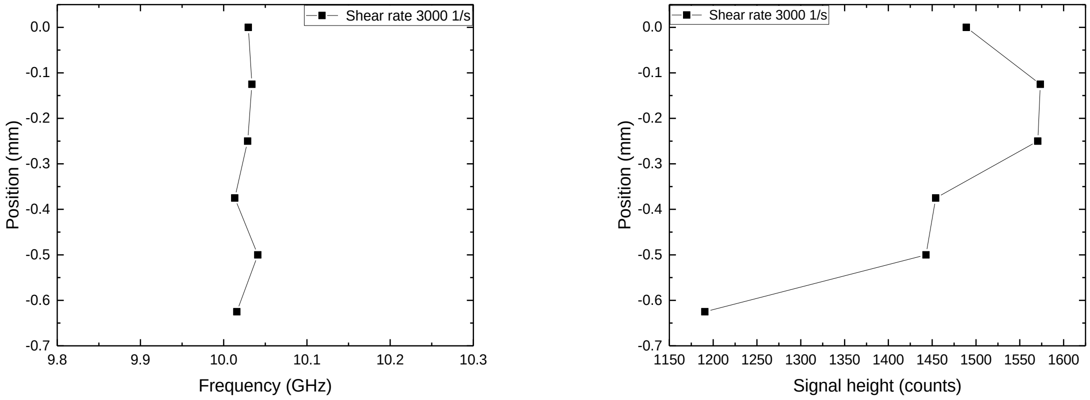

Figure 71: Position of scattering volume in z-direction over Brillouin frequency shifts $f_{q_{180}}$, left; right, the signal height values for the PVP 2.5 mass percent PEG sample in a 0.5 mm gap, at 25°C, for 3000 s^{-1} shear rate, for the sample area (height).

The average frequency over the z-axis is 10.027 GHz +- 0.014 GHz for 3000 s^{-1} shear rate $\dot{\gamma}$ with a maximal signal height of about 1550 counts. Repeating the zero shear rate experiment, going upwards with the focal spot position is giving the plots of Figure 72.

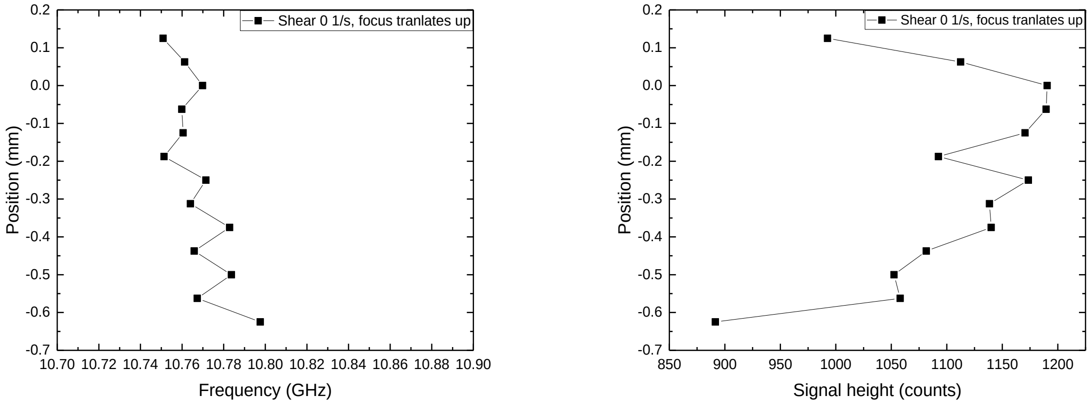

Figure 72: Position of scattering volume in z-direction over Brillouin frequency shifts $f_{q_{180}}$, left; right, the corresponding signal height values for the PVP 2.5 mass percent PEG sample in a 0.5 mm gap, at 25°C, zero shear, picturing the sample area.

The average frequency for zero shear over the z-axis is 10.774 GHz + -0.075 GHz and the maximum signal height is about 1200 counts.

For 5 different positions in z-direction, for which each three Brillouin spectra of 1min acquisition time, at 25°C, and no applied shear, are recorded and plotted in Figure 73. The average Brillouin shift values are then plotted next to it, as the signal height values. The scale of the relative position is now different as before.

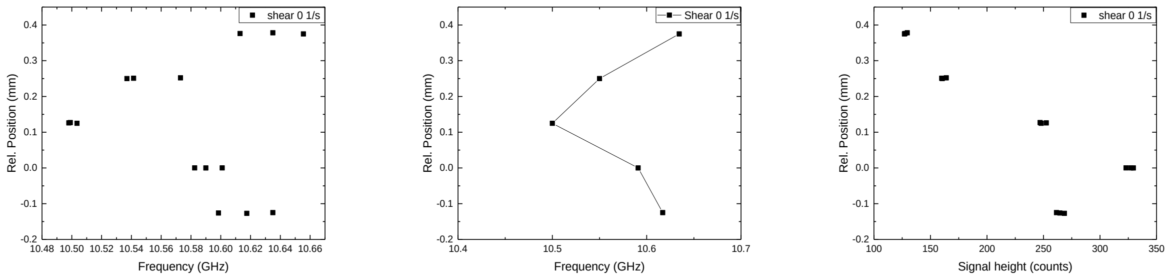

Figure 73: Relative position of scattering volume (5 positions) in z-direction, left three measurement values for each position, middle, the average values for the PVP 2.5 mass percent PEG sample, in a 0.5 mm gap at 25°C, for zero shear and 1 min acquisition time. Right the signal height values of the each of the three measurements.

The average value of the frequencies over z-position is 10.578 GHz +- 0.079 GHz and the signal height has its maximum at about 350 counts. Interestingly, the frequency has its minimum value at middle z-position, while the signal height behaves inverted, having its maximum intensity in this regime.

The acquisition time is raised to 3 min, as again, three measurements of the Brillouin shifts, now for 9 positions in z-direction, have been implemented and are plotted in Figure 74 for zero shear, next to their signal height values.

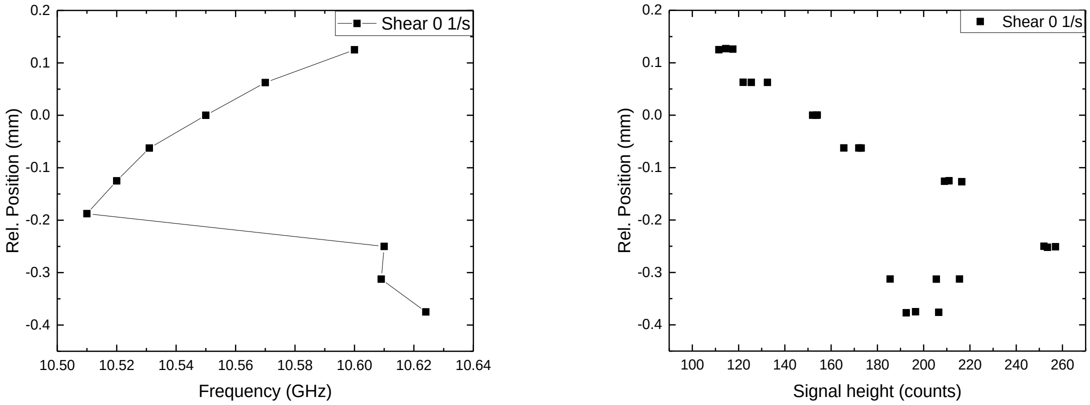

Figure 74: Relative position of scattering volume (9 points) in z-direction with its average values for frequencies, left. Right, the signal heights of the PVP 2.5 mass percent PEG sample in a 0.5 mm gap, at 25°C, for zero shear and 3 min acquisition time, each.

The average value of the frequencies over z-position is 10.569 GHz +- 0.059 GHz as the signal height has its maximum at about 250 counts. However, the inverted behavior of frequency and signal heights over the position is again visible. This experiment is repeated a last time showing still the same inverted behavior of frequency (10.521 GHz +- 0.034 GHz) and signal heights over z-position and is plotted in the Figure 75.

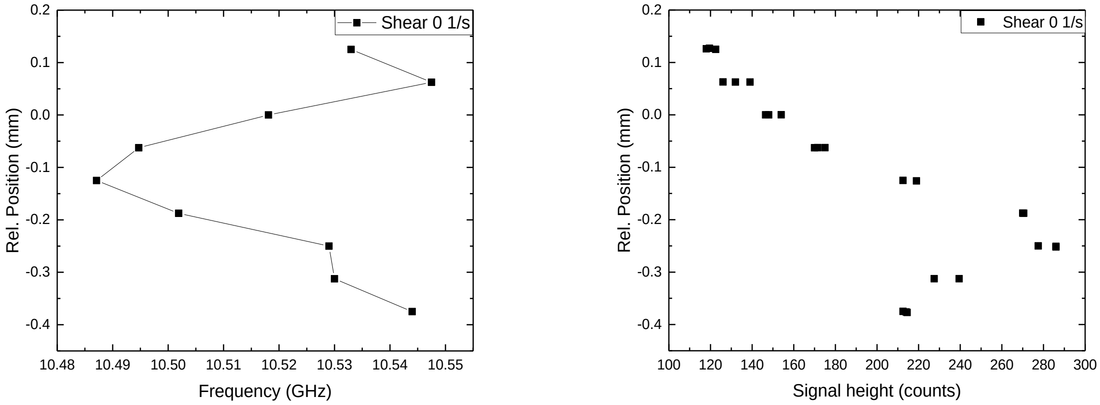

Figure 75: Relative position of scattering volume (9 points) in z-direction, average values for the PVP 2.5 mass percent PEG sample in a 0.5 mm gap, at 25°C, for 3000 s^{-1} applied shear rate and 3 min acquisition time, each.

A discussion of this investigation is shown in a latter section.

4.1 First results from Brillouin Rheology using backscattering

4.1.1 Shear rate dependency

In the following, viscosity curves of the sample material for a range of shear rates $\dot{\gamma}$ are recorded and plotted in Figure 76. Brillouin shift frequencies of $f_{q_{180}}$ are measured analogy to the rheology and plotted in Figure 77.

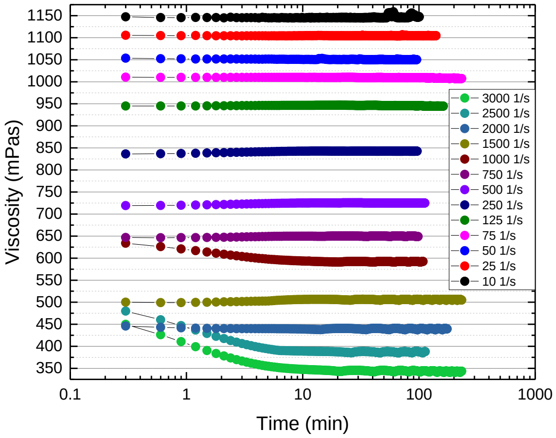

Figure 76: Viscosity curves of PVP 2.5 mass percent PEG in a 0.5 mm gap at 25°C for different shear rates $\dot{\gamma}$.

The rheology shows that about 10-15 min are needed to record stable values for the viscosity η. However, recording the viscosity curves for different shear rates $\dot{\gamma}$, analogy, Brillouin shifts are recorded (scattering volume in middle z-position in the sample at the edge of the geometry) for 14 min. Each of the 5 measurements are plotted in Figure 77.

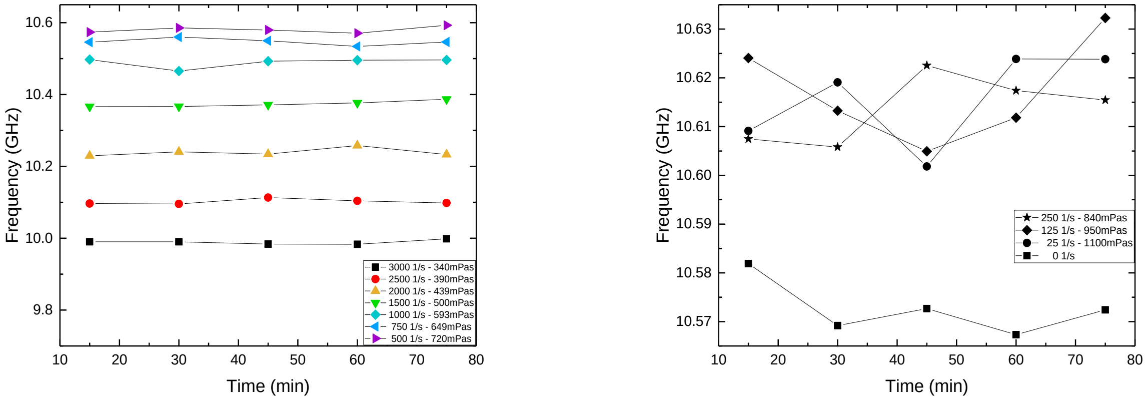

Figure 77: Recorded Brillouin shifts $f_{q_{180}}$ of PVP 2.5 mass percent PEG over time for different shear rates $\dot{\gamma}$.The corresponding viscosity values from rheology are noted as well. Left, the colored sequence from 500 s^{-1} shear rate upwards; right, the ones with smaller shear, to visualize it more clearly.

The recorded Brillouin shift values $f_{q_{180}}$ are quite constant over time. Nevertheless, the dependency, or correlation to the viscosity η gets more obvious, as the Brillouin shift frequencies, starting from 500 s^{-1} decrease with increasing shear rate $\dot{\gamma}$ and decreasing viscosity. The average values for the frequency shifts are listed in Table 5.

Table 5: Brillouin shift frequency average values $< f_{q_{180}} >$ (out of five measurements) in GHz, with corresponding tolerance for the scattering volume being in middle z-direction position and radial edge position of the sample. The shear rate $\dot{\gamma}$ applied with the rheometer and the measured viscosity η values recorded after 15 min shearing.

$\dot{\gamma}$ (s^{-1})	$< f_{q_{180}} >$ (GHz)	$<f_{q_{180}}>$ +- (GHz)	η (mPas)	η +- (mPas)
0	10.573	0.009	-	-
10	10.604	0.012	1151	7
25	10.616	0.014	1105	2
50	10.621	0.022	1051	2
75	10.611	0.013	1008	2
125	10.617	0.015	945	2
250	10.614	0.009	839	3
500	10.581	0.012	722	3
750	10.547	0.013	648	2
1000	10.489	0.024	592	2
1500	10.374	0.013	503	4
2000	10.239	0.019	441	4
2500	10.102	0.012	386	4
3000	9.989	0.01	342	2

Plotting the values of Brillouin shift frequencies $f_{q_{180}}$ and viscosity η over the shear rate $\dot{\gamma}$ regime gives Figure 78 (as normal and logarithmic-scale plot).

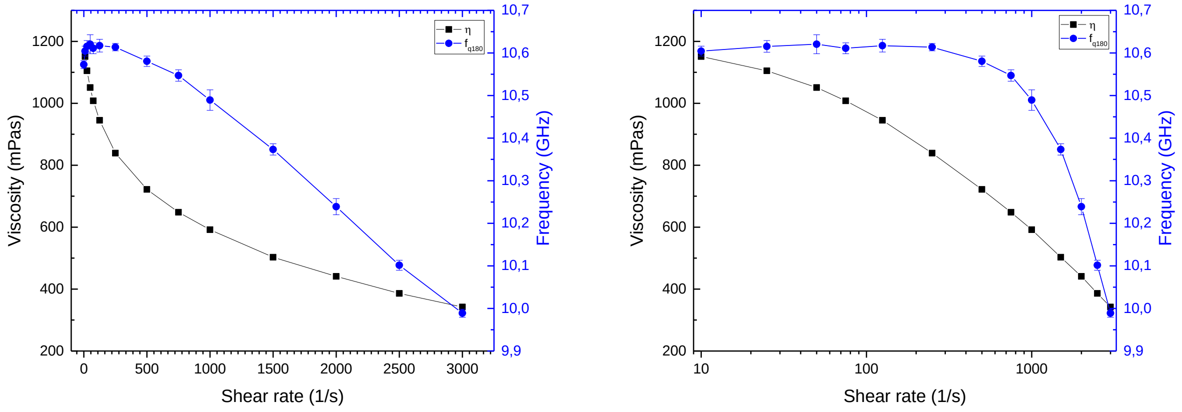

Figure 78: Viscosity η and Brillouin shifts $f_{q_{180}}$ over shear rate $\dot{\gamma}$. Left, normally plotted, right logarithmically, respectively.

As the plots show, the Brillouin shift frequencies are decreasing with increasing shear rate as the viscosity values are decreasing as well. This starts for the frequency shifts mainly at about 1000 s^{-1} shear rate from about 10.5 GHz to about 10 GHz at 3000 s^{-1} shear rate.

Further analysis lead to the comparison of Brillouin shift frequencies $f_{q_{180}}$ for the scattering volume, positioned at different radial positions for a shear rate $\dot{\gamma}$ of 3000 s^{-1}, which is plotted in the following Figure 79 for a central, relative middle, and edge position (y-direction) of the scattering volume in the sample between the plate-plate rheological geometry (sketched in Figure 125).

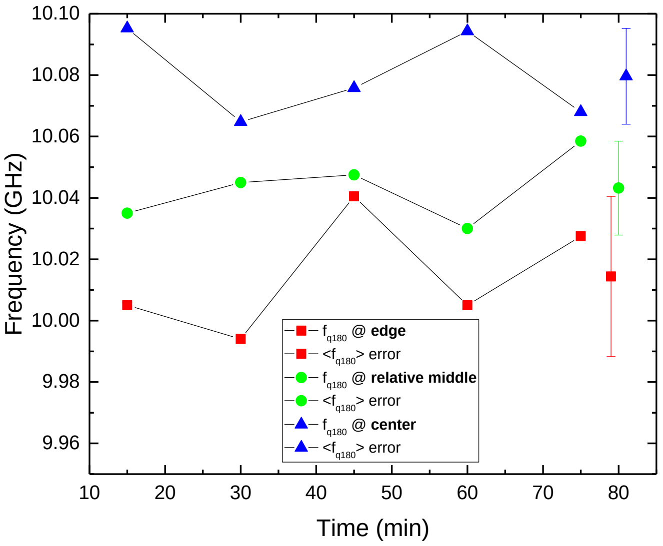

Figure 79: Brillouin shifts $f_{q_{180}}$ over time at three different radial positions of the scattering volume inside the rheometer sample stage at an applied shear rate $\dot{\gamma}$ of 3000 s^{-1} at 25°C.

The measurements imply that we can picture a difference in the Brillouin frequency shifts $f_{q_{180}}$ for the three radial positions. However, the series of edge, middle and center position also show a same order that might indicate the inhomogeneous shear field in the PP25 geometry.

To investigate, if the seemingly position (of scattering volume in y-direction) dependency of the Brillouin frequency shifts is there, an experimental series at central position of the scattering volume in the sample has been implemented. The shear rate is decreased from 3000 s^{-1} down to a minimum shear rate and spectra are collected for 14 min, 5 times and plotted in Figure 80.

The Brillouin shift frequencies again display the same behavior. The error of the average values for the spectra are calculated and the maximum derivation taken as error. This tells us that we can distinguish the Brillouin frequency shift values starting from an applied shear rate $\dot{\gamma}$ of 500 s^{-1} up to 3000 s^{-1}. The corresponding errors are smaller so the values are not overlapping anymore, like for smaller shear rates, so the measurements are valid as Table 6 depictures with the measured values.

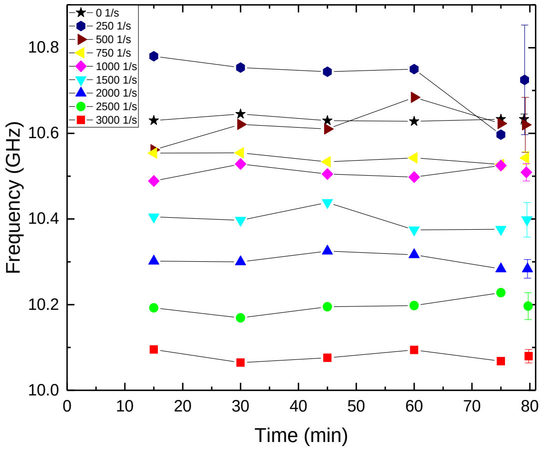

Figure 80: Brillouin shifts $f_{q_{180}}$ over time for the PVP 2.5 mass percent PEG sample in a 0.5 mm gap, at 25°C, for different shear rates $\dot{\gamma}$, having the scattering volume in central position of the sample stage.

Table 6: Brillouin shift frequency average values (out of five measurements) $<f_{q_{180}}>$ in GHz with corresponding tolerance for the scattering volume being in middle z-direction position and radial central position of the sample with corresponding shear rate $\dot{\gamma}$ applied with the rheometer.

$\dot{\gamma}$ (s^{-1})	$< f_{q180} >$ (GHz)	$< f_{q180} >$ +- (GHz)
0	10.633	0.012
250	10.725	0.128
500	10.62	0.064
750	10.542	0.015
1000	10.509	0.020
1500	10.398	0.040
2000	10.284	0.022
2500	10.197	0.032
3000	10.08	0.016

Plotting this measurement series (Figure 81) at central radial position to the previous experimental series at edge position it gets obvious that there is a difference that we can picture with the Brillouin Rheology approach.

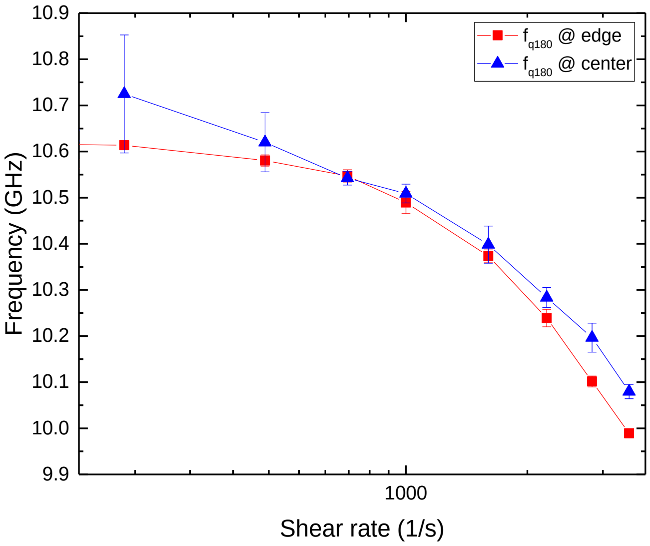

Figure 81: Brillouin frequency shifts $f_{q_{180}}$ *over shear rate* $\dot{\gamma}$ *for the scattering volume being in the middle z-plane of the sample. Comparison of central and radial edge position in y-direction.*

To get more precise measurements the experiments are repeated in a bigger scale experimental series that is shown in the following section.

4.1.2 A study of shear rate and radial position dependency

In the following, a large experimental series is implemented. The Brillouin shifts $f_{q_{180}}$ are collected for 14 min, three times for each shear rate $\dot{\gamma}$, at 25°C, in the 0.5 mm gap, for three z positions (edge of the plate-plate geometry (r = 11.5 mm), in the relative middle between the edge and the center of it (r = 6.5 mm) and in the center of the sample stage (r = 0.5 mm)). More detailed information are to be found in the next chapter. The Brillouin frequency shift values for q_{180} are plotted over time as the average value is then plotted over the shear rate $\dot{\gamma}$, respectively.

Edge position of the sample

The Brillouin shift frequencies for different shear rates over time, at the edge position of the sample volume are shown in Figure 82.

The measurement values of Brillouin frequency shift`s average value $<f_{q_{180}}>$ with maximum derivation to the corresponding shear rates is listed in Table 7.

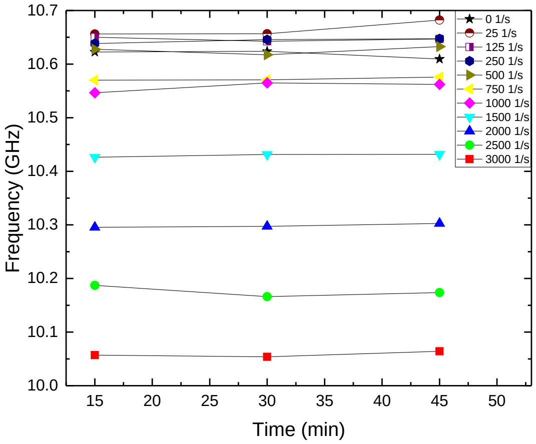

Figure 82: Brillouin shifts $f_{q_{180}}$ over time for the PVP 2.5 mass percent PEG sample in a 0.5 mm gap at 25°C. The acquisition time is each time 14min. Different shear rates $\dot{\gamma}$ are compared. Scattering volume in middle z-plane and at edge position of the sample.

Table 7: Brillouin shift frequencies' average values <$f_{q_{180}}$> with maximum derivation (out of three measurements) for shear rates $\dot{\gamma}$, applied in the rheometer with the PVP 2.5 mass percent PEG sample in a 0.5 mm gap, at 25°C. Scattering volume at edge position of the PP25.

$\dot{\gamma}$ (s^{-1})	**<$f_{q_{180}}$> (GHz)**	**<$f_{q_{180}}$> error (GHz)**
3000	10.0584	0.006
2500	10.176	0.011
2000	10.299	0.004
1500	10.43	0.004
1000	10.558	0.011
750	10.572	0.004
500	10.626	0.009
250	10.644	0.006
125	10.647	0.004
25	10.665	0.017
0	10.619	0.009

The average values of each of the three measurements of Brillouin shift frequency <$f_{q_{180}}$> (previous plot and table) are plotted over shear rate $\dot{\gamma}$ in logarithmic scale in Figure 83.

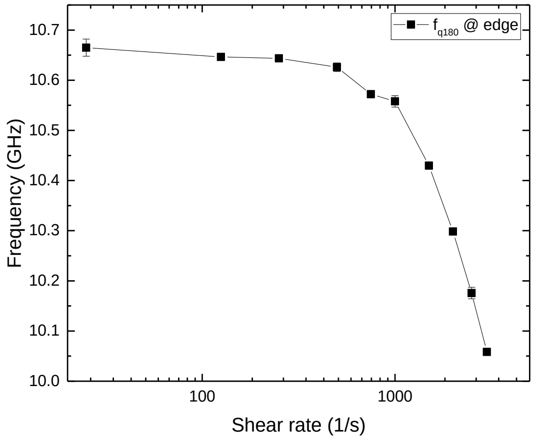

Figure 83: Brillouin shifts average values <$f_{q_{180}}$> at edge position of the PVP 2.5 mass percent PEG sample in a 0.5 mm gap, at 25°C, over shear rate $\dot{\gamma}$ (logarithmically plotted).

Relative radial middle position of the sample

The scattering volume is translated 6 mm in direction to the center of the sample stage and the PP25. The experimental series is repeated and plotted in Figure 84.

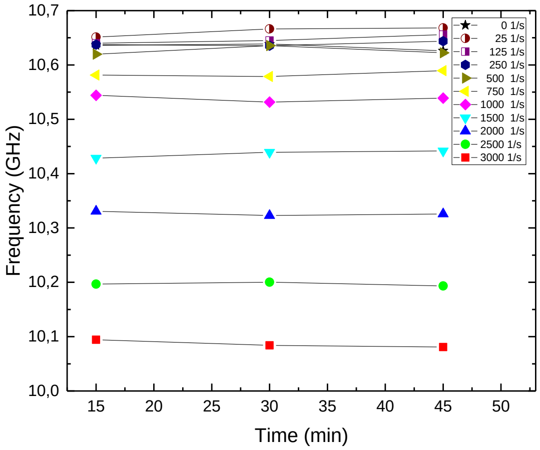

Figure 84: Brillouin shifts $f_{q_{180}}$ over time for the PVP 2.5 mass percent PEG sample in a 0.5 mm gap at 25°C, acquisition time for each spectra is 14 min, for different shear rates $\dot{\gamma}$. Scattering volume in middle z-plane and at relative radial middle position of the sample.

The behavior of the frequency shifts to increasing shear is identical to the measurement at the edge position, just the values appear to be slightly higher as depictured with Table 8, of the average frequency values <$f_{q_{180}}$> from the three measurements, with corresponding maximum derivation.

Table 8: Brillouin shift frequencies' average values <$f_{q_{180}}$*> with maximum derivation (out of three measurements) for shear rates* $\dot{\gamma}$ *applied in the rheometer with the PVP 2.5 mass percent PEG sample in a 0.5 mm gap, at 25°C. Scattering volume at relative radial middle position of the PP25.*

$\dot{\gamma}$ (s^{-1})	$<f_{q180}>$ (GHz)	$<f_{q180}>$ error (GHz)
3000	10.086	0.008
2500	10.197	0.004
2000	10.327	0.004
1500	10.437	0.008
1000	10.538	0.007
750	10.583	0.006
500	10.626	0.01
250	10.639	0.005
125	10.647	0.009
25	10.662	0.011
0	10.634	0.008

Figure 85 shows the average values of Brillouin shifts plotted over the shear rate $\dot{\gamma}$ in logarithmic scale. The errors are so small that one cannot see them in the plot.

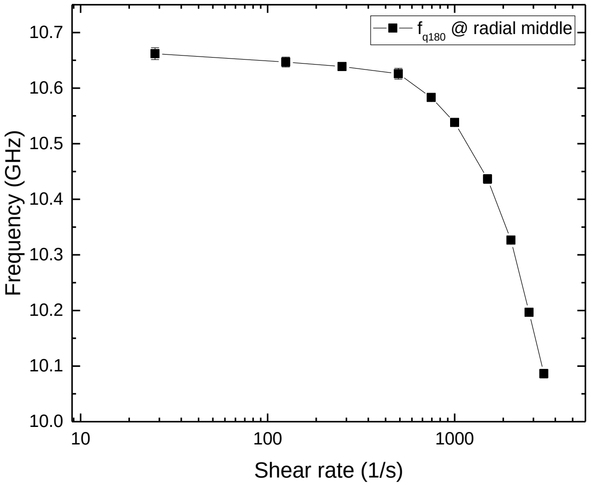

Figure 85: Brillouin shifts average values <$f_{q_{180}}$*> at relative radial middle position of the PVP 2.5 mass percent PEG sample in 0.5 mm gap, at 25°C, over shear rate* $\dot{\gamma}$ *(logarithmically plotted).*

The curve of the measurement values having the scattering volume at relative radial middle position of the sample also shows the steep increase of frequency at high shear rates. Comparing the values of both previous measurement series (Table 7 and Table 8), imply slightly higher values of frequencies, having the scattering volume at this position than at the edge. Next, the scattering volume is translated in direction to the center position of the sample and the measurements are repeated.

Central position of the sample

At last, the scattering volume is positioned near the central position of the PP25 geometry and the measurement sequence is repeated. The Brillouin shift frequencies for each of the three measurements are plotted in Figure 86.

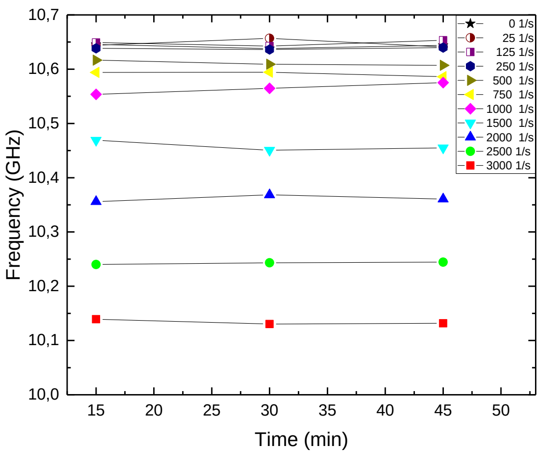

Figure 86: Brillouin shifts $f_{q_{180}}$ over time for the PVP 2.5 mass percent PEG sample in a 0.5 mm gap at 25°C, acquisition time each 14 min, for different shear rates $\dot{\gamma}$. Scattering volume in middle z-plane and at central position of the sample.

Again, the measurement values of the Brillouin frequency shifts are slightly higher, in general, compared to both previous measurement series.

Table 9 lists the average frequency values $<f_{q_{180}}>$ of these three measurements with the corresponding maximum derivation.

Plotting the average values of frequency shifts $<f_{q_{180}}>$ with its maximum derivation for the scattering volume being in center position of the sample stage, over the shear rate $\dot{\gamma}$ in logarithmic scale, results in Figure 87.

Table 9: Brillouin shift frequencies' average value <$f_{q_{180}}$> with maximum derivation (out of three measurements) for shear rates $\dot{\gamma}$ applied in the rheometer with the PVP 2.5 mass percent PEG sample in a 0.5 mm gap, at 25°C. Scattering volume at central position of the sample stage.

$\dot{\gamma}$ (s^{-1})	<$f_{q_{180}}$> (GHz)	<$f_{q_{180}}$> error (GHz)
3000	10.134	0.006
2500	10.243	0.003
2000	10.362	0.007
1500	10.458	0.011
1000	10.566	0.011
750	10.592	0.005
500	10.611	0.006
250	10.638	0.002
125	10.648	0.006
25	10.647	0.01
0	10.643	0.005

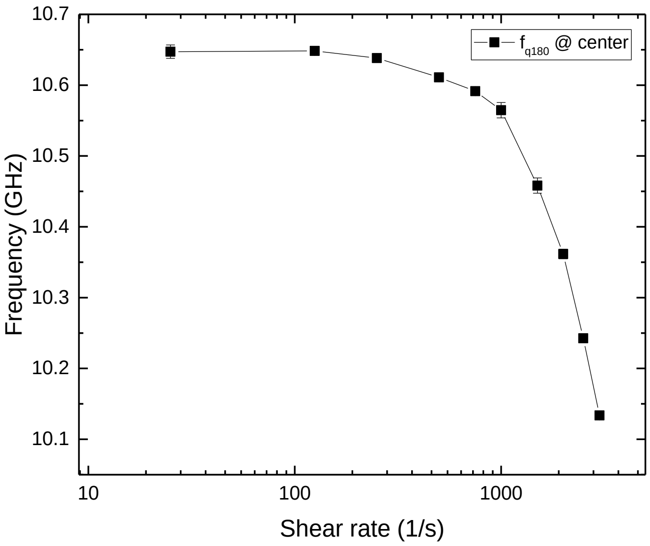

Figure 87: Brillouin frequency shift average values <$f_{q_{180}}$> at central position of the sample stage for the PVP 2.5 mass percent PEG sample in 0.5 mm gap, at 25°C, over shear rate $\dot{\gamma}$ (logarithmically plotted).

A third time, the curve seems very similar, having a steep decrease of frequency at high shear rates. To picturize and visualize better, in the following, the plots are compared.

4.1.3 Comparison of Brillouin shifts over increased shear rate at different radial positions

Comparing the three measurement sequences at the three radial positions and plotting it, it gives Figure 88 of average values of Brillouin shift frequency $<f_{q_{180}}>$ over shear rate $\dot{\gamma}$ in logarithmic scale.

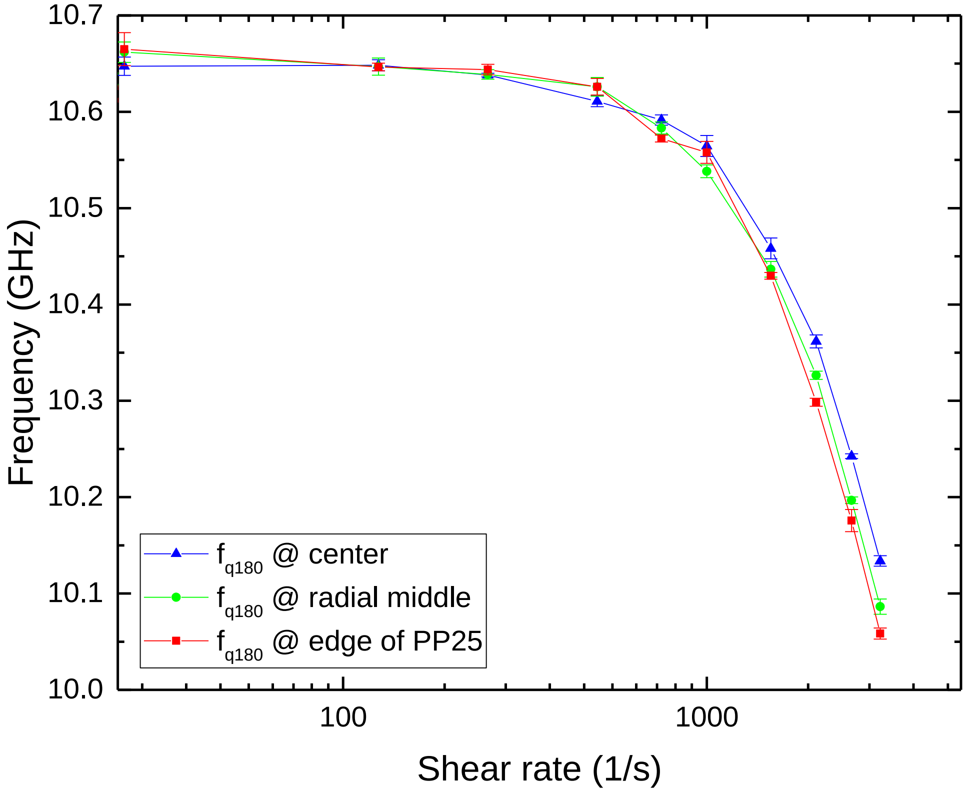

Figure 88: Comparison of three measurement positions of the scattering volume (at the middle of the sample volume in z-direction). Collected Brillouin shift average values $<f_{q_{180}}>$ over shear rate $\dot{\gamma}$ (logarithmically plotted) for the PVP 2.5 mass percent PEG sample in a 0.5 mm gap, at 25°C.

The comparison shows the same behavior as previous measurements indicated, namely, that the average Brillouin shift frequency values $<\boldsymbol{f_{q_{180}}}>$ seem to be able to picture the shear thinning behavior of the material. However, a distinct difference of the Brillouin frequency shifts for the three positions of the scattering volume are imminent. The change of frequency at central position is merely smaller than the one at the edge position. The measurement series at the relative center merges into those two, starting with higher shear rates than 1000 s^{-1}. A more detailed investigation and discussion is given in the next chapter. However, to picture this area of interest more clearly following Figure 89 is shown. With higher shear rates than 1000 s^{-1} the curves are separated from each others and do not cross again. This seems to indicate that a difference in viscosity due to the different relative velocities at the radial positions can be pictured for those high shear rates.

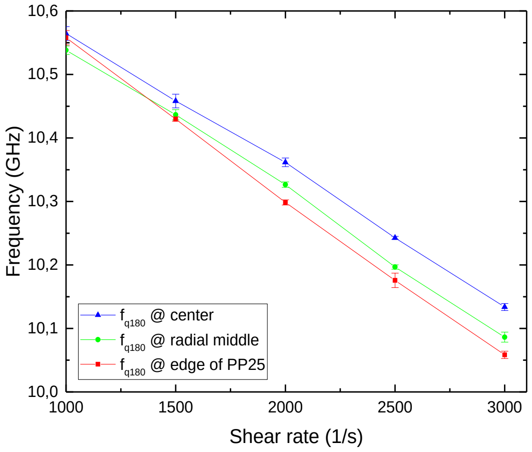

Figure 89: Comparison of three measurement positions of the scattering volume (at the middle of the sample volume in z-direction). Collected Brillouin shift frequency average values $<f_{q_{180}}>$ *over shear rate* $\dot{\gamma}$ *for the PVP 2.5 mass percent PEG sample in a 0.5 mm gap, at 25°C. Shear rate regime just from 1000* s^{-1} *to 3000* s^{-1} *to show the area of interest.*

Previously in this work it was mentioned that the material seem to show relaxation effects, which we might also be able to picture with the spectrometer, so a little investigation in that regard is undertaken in the following.

4.1.4 Brillouin Rheology and relaxation effects

While the experiments are implemented, it gets obvious that the shear stress and the viscosity measured with the rheometer, show different behavior in the beginning of new measurement sequences.

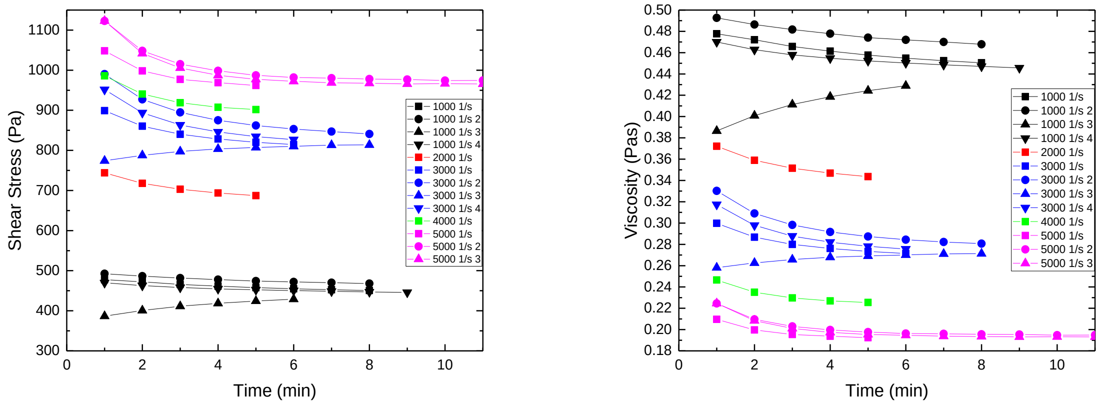

Figure 90: Comparison of shear stress τ and viscosity η over time for several starts of measurement sequences and corresponding high shear rates $\dot{\gamma}$ for the PVP 2.5 mass percent PEG sample in 0.5 mm gap, at 25°C.

The rheology data differ slightly, dependent if the material is newly put into the stage, or after long time high shear rates were applied. This may imply some orientation or texturing effects while shearing. This is shown in the overview of viscosity curves for different shear rates $\dot{\gamma}$ (1000 s^{-1}, 2000 s^{-1}, 3000 s^{-1}, 4000 s^{-1}, 5000 s^{-1}), shear stresses τ and viscosities η over time, for several start periods of measurement sequences (Figure 90).

It gets visible that repeating a measurement with the same shear rate $\dot{\gamma}$, for different times, can lead the viscosity η to either increase or decrease, till it reaches its constant value. This implies relaxation effects that shall be studied in more detail in the following.

Plotting the comparison for high shear rates $\dot{\gamma}$ of 1000 s^{-1}, 3000 s^{-1} and 5000 s^{-1} it gives Figure 91.

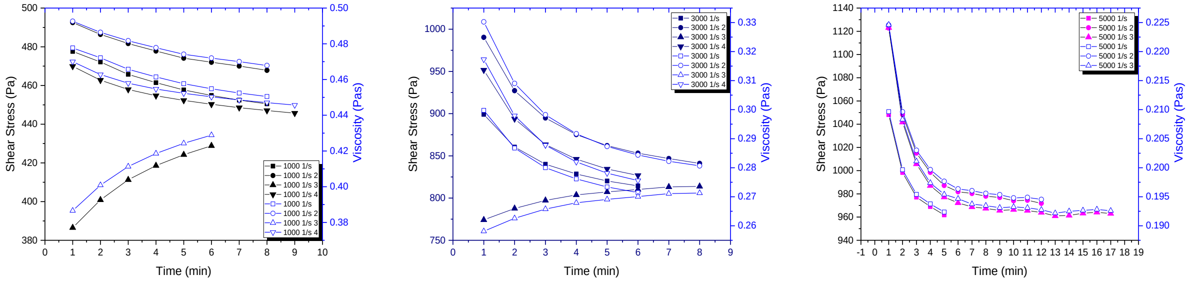

Figure 91: Comparison of viscosity curves for three high shear rates $\dot{\gamma}$ (1000 s^{-1}, 3000 s^{-1} and 5000 s^{-1}) and retests plotted over time for the PVP 2.5 mass percent PEG sample in 0.5 mm gap, at 25°C. Open symbols denote the viscosity values.

Applying 5000 s^{-1} shear rate and measuring the flow curve (shown right, Figure 91), after about 10 min, the value of shear stress and viscosity find a kind of an equilibrium state. The first measurement, which is stopped after 5 min is the initiation of the test. Repeating the measurement, both values are quite higher and appear to be constant after about 10 min. The third test merges in between both measurements. Going to 3000 s^{-1} shear rate the same effect happens. First, measurement has the lowest values of viscosity η, second, the highest, and third, in the middle of both previous measurements. Nevertheless, a measurement with 3000 s^{-1} made directly after a measurement with 5000 s^{-1} shows a different behavior, namely, the shear stress and viscosity are increasing with time, until arriving its constant value. This further indicates that there are relaxation effects in the material. Having the applied shear rate of 1000 s^{-1}, again, the order is the same. The first flow curve shows low values, the second, the highest. Anyhow, now the third measurement series appears quite lower in values than the second one. Increasing the shear to 3000 s^{-1} and then apply the measurement with 1000 s^{-1} also leads to the behavior of shear thickening at the beginning of the measurement. To investigate this further, Brillouin Rheology measurements are implemented.

The rheometer is set to a shear rate $\dot{\gamma}$ of 3000 s^{-1}, the PVP 2.5 mass percent PEG sample is loaded in the 0.5 mm gap at 25°C and a laser power of 28 mW is applied. Figure 92 shows the recorded flow and viscosity curves of the experimental series for 25°C and 40°C. After the shear is applied for 20 min the rheometer is stopped and spectra are collected for about 1 min each, 10 measurements in a row, so for 10 min.

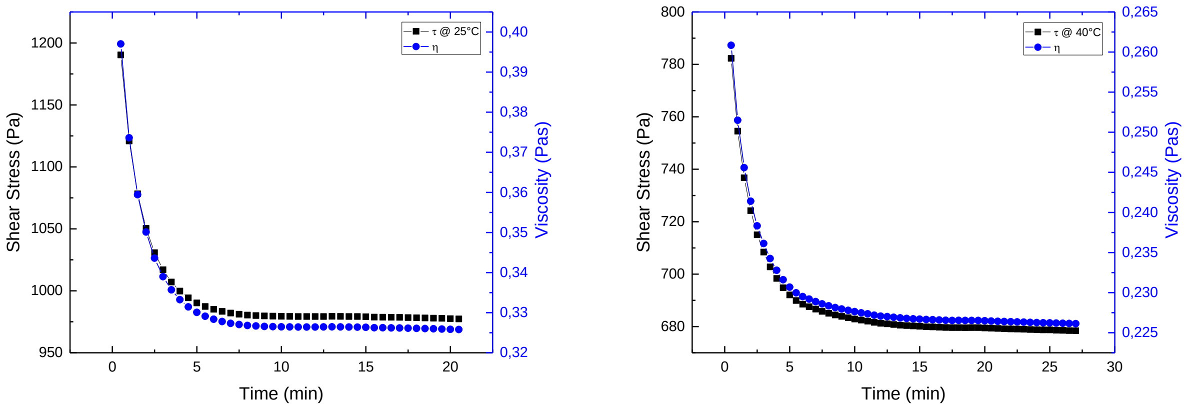

Figure 92: Flow and viscosity curves of the relaxation experiments for PVP 2.5 mass percent PEG at 25°C left; right, at 40°C with 3000 s^{-1} applied shear rate $\dot{\gamma}$.

The first acquired Brillouin spectra of about 1 min per each measuring point after stopping the rheometer from 3000 s^{-1} shear rate at a temperature of 40°C are plotted in Figure 93 over time. Next to it, the signal height values that are quite stable over time as the frequency is increasing about 0.2 GHz in 8 min.

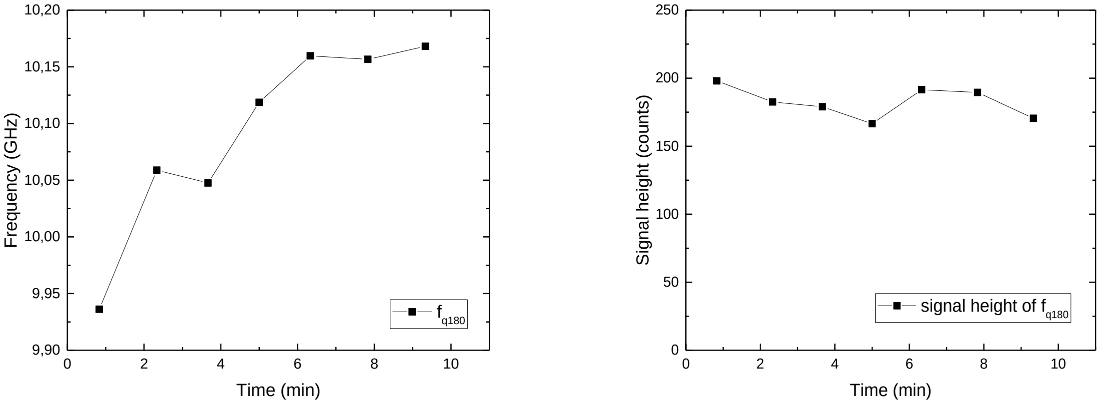

Figure 93: Brillouin shifts $f_{q_{180}}$ over time of the PVP 2.5 mass percent PEG sample in a 0.5 mm gap at 40°C, left; right, corresponding signal heights. After stopping the rheometer from 3000 s^{-1} shear rate, after 30 sec, the first measurement starts, goes for 50 sec, is saved and the second measurement is started, etc..

To investigate this behavior more detailed, Figure 94 shows a measurement sequence in which point 1 shows a Brillouin spectroscopy measurement for 4 min of the PVP 2.5 mass percent PEG sample without a PP25 attached to the rheometer (and sample). Point 2 denotes the same measurement having the PP25 attached and a set gap size of 0.5 mm. Both measurements are done without an applied shear. Applying 3000 s^{-1} shear rate to the sample for 20 min (the rheometer gives a viscosity η value of 325 mPas) then the spectroscopic measurement has been implemented for 4 min acquisition time. Point 4 shows the measurement point 10 sek after the rheometer stopped (the PP25 still turning out). The acquisition time starting from there on is 50 seconds for each point for a set temperature of 25°C.

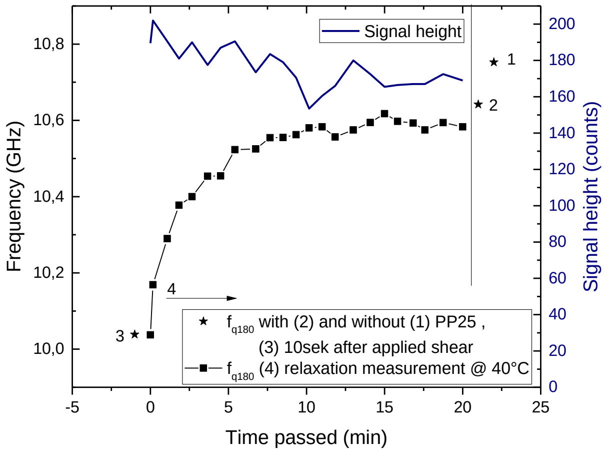

Figure 94: Investigation of relaxation behavior of PVP 2.5 mass percent PEG, at 25°C. Brillouin frequency shifts $f_{q_{180}}$ over time for different settings (1-4 see description in text) with corresponding signal height values.

The Brillouin frequency shift curve shows the tendency of the relaxation the sample is undergoing after stopping the applied shear force.

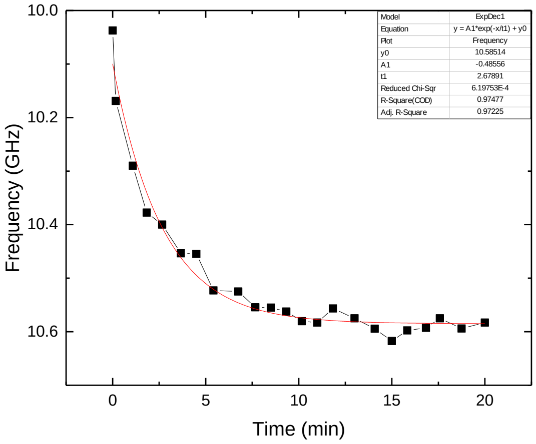

Figure 95: Brillouin shifts $f_{q_{180}}$ over time after stopping the rheometer from 3000 s^{-1} shear rate with an exponential decrease fitted curve, at 25°C.

The signal strength (signal height values) shows same quality (but a small decrease) over the measurement time. Plotting the frequency inverse from high to small values a fit (e.g. an exponential decrease fit) can be implemented with Origin to describe the measurement curve mathematically for further evaluation (Figure 95).

The relaxation experiments are repeated and implemented for <u>40°C</u> temperature as it is expected, that the relaxation times decreases with the higher temperature.

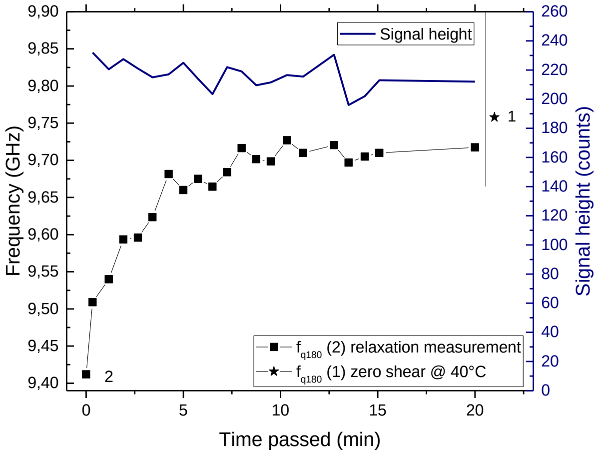

Figure 96: Investigation of relaxation behavior of PVP 2.5 mass percent PEG at 40°C. Brillouin frequency shifts $f_{q_{180}}$ over time for different settings (1 and 2 see description in text) with corresponding signal height values.

Point 1 in Figure 96 shows the Brillouin measurement without shear. Applying a shear rate of 3000 s^{-1} for 20 min the 2nd Point is measured as the following for 50 sec acquisition time. The Brillouin frequency shift curve shows similar behavior then before, at 25°C, as now the corresponding frequency values at 40°C are smaller in general and show a change in frequency of about 0.3 GHz over time.

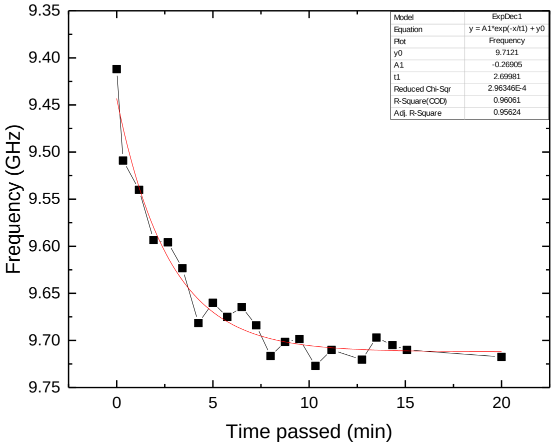

Figure 97: Brillouin shifts $f_{q_{180}}$ *over time after stopping the rheometer form 3000 s*$^{-1}$ *shear rate with an exponential decrease fitted curve, at 40°C.*

Plotting the frequency inverted, again, giving a decreasing exponential fit function that is shown in Figure 97. An interesting corresponding article can be found in [126]. Comparing both fits, the times are nearly the same. This is unexpected and should be researched in another study.

Chapter 5: Brillouin Rheology - the proof of concept

This chapter contains in the beginning the comparison of different rheological geometries to clarify which influence the material, surface and diameter of the plates may have to the measurements. The temperature of the sample which is heated and controlled by the rheometer is measured additionally with a temperature sensor to see if the change of the rheometer` s body (and hard cover) to gain optical access has an influence. The dimensions of the scattering volume are discussed as the chosen optics for the experiments. The signal quality of the Brillouin spectra is analyzed regarding the laser beam power. A way to identify and position the scattering volume in the sample volume (inside the gap of the rheological geometries) is explained. The behavior of Brillouin frequency shifts regarding temperature change are discussed in comparison to the viscosity behavior, having the scattering volume at an outer radial position and an applied high shear. The behavior of the Brillouin shifts for increasing the shear rate (in the rheometer` s possible range) is interpreted and discussed regarding further experiments at three different radial positions. At last the relaxation effects which are found rheologically and could be measured with Brillouin spectroscopy are interpreted and compared.

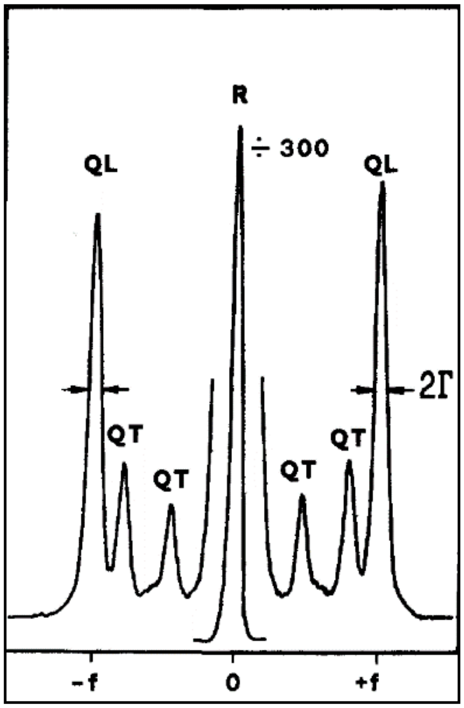

Figure 98: Example Brillouin spectrum of a crystal from [127], a Hexatriacontane at room temperature. The Stokes (f) and anti-Stoke (-f) lines are shown for the quasi-transvers (QL) and quasi-longitudinal (QT) acoustic phonons at phonon frequency f. The middle peak is the Rayleigh line, which is due the elastic scattering much more intense and is shorted here by 300 % to fit the plot. The linewidth 2Γ gives a measure of the acoustic losses.

As introduced in the beginning, the scattering geometries are shown as the corresponding equations to relate the wave vector of the light with the wave vector of the acoustic wave in the material. Figure 98 shows a spectra of a crystal [127] with quasi-transverse (QT) and a quasi-longitudinal (QL) peaks (for stokes and anti-stokes scattering). The indicated linewidth [128] that can be related to acoustic losses and the viscosity [129] is not studied into detail here, as this work is more concerned with the proof-of-concept of the whole idea and the development, realization and function.

Nevertheless, if this work proves well, all these additional information and relations can be derived out of this newly developed system afterwards, due to a more improved set-up in the future.

To get a deeper inside in the topic the works from J. G. Dil [130] regarding the Brillouin spectroscopy in condensed matter and R. Figgins [131] regarding the scattering in liquids are recommended as the works of Patterson, Krüger and Sandercock, which are cited several times in this work.

The q-vector, hyper-sound velocity and the longitudinal stiffness modulus

Figure 43 gives the overview of the most common scattering geometries and their related equations, which are mathematically derived from Bragg-Snell law of refraction and scattering (both introduced in [127, 132-134]). As this work is concerned mainly with the backscattering geometry (in the appendix with the more special scattering type of $RI\Theta A$ scattering as well) only these two will be discussed further.

The following relation (Eq. (36)) describes the scattering acoustic wave vector in an isotropic sample, which depends on the scattering angle Θ_s, the refractive index of the material $\boldsymbol{n}$ and the wavelength $\boldsymbol{\lambda}$ of the laser which is 532 nm.

$$q = \frac{4\pi n \cdot \sin(\frac{\Theta_s}{2})}{\lambda} \tag{36}$$

For the simple approach of backscattering (Θ_s = 180°) the relation reduces to (Eq. (37)):

$$q^{180} = \frac{4\pi n}{\lambda} \tag{37}$$

With $q^{180} = \frac{\omega^{180}}{v^{180}}$ it follows the dependency of the sound velocity v^{180} (Eq. (38)) from the measured Brillouin shift $f^{180} = \frac{\omega^{180}}{2\pi}$ in the spectra:

$$\mathrm{v}^{180} = \frac{\omega^{180} \cdot \lambda}{4\pi \mathrm{n}} \tag{38}$$

For backscattering only frequencies of longitudinal phonons can be evaluated. From the acoustic hyper-sound velocity of the longitudinal phonons v_{long} in an isotropic medium the corresponding component c_{11} of the elastic stiffness tensor (Voigt notation [135, 136]) can be calculated (Eq. (39)) using the data from the density measurements, e.g. for the PVP 2.5 mass percent PEG sample material:

$$\mathrm{c}_{11} \triangleq \mathrm{M}' = \rho * (\mathrm{v}_{\mathrm{long}})^2 \tag{39}$$

It follows finally (Eq. (40)) for the purely longitudinal component c_{11} of the stiffness tensor for solids or in fluids, the longitudinal rigidity modulus M’ [137-139]:

$$\mathrm{M}' \triangleq \mathrm{c}_{11} = \rho \cdot \left(\frac{\omega^{180} \cdot \lambda}{4\pi \mathrm{n}}\right)^2 \tag{40}$$

Regarding the special type of a scattering geometry, the $RI\Theta A$ scattering (Figure 43) has the following geometrical relations (Eq. (41)):

$$\mathrm{q}^{\Theta \mathrm{A}} = \frac{2 \cdot \sin(\frac{\Theta_s}{2})}{\lambda} \tag{41}$$

The relation of Brillouin shift frequency to sound velocity of the phonon and q-vector (Eq. (42)) is given by the following equation.

$$\omega^{\theta \mathrm{A}} = \frac{\mathrm{v}_{\mathrm{a}}^{\theta \mathrm{A}} \cdot \sin(\frac{\Theta_s}{2})}{\pi \lambda} \tag{42}$$

To calculate the hyper-sound velocity of $v_a^{\theta A}$ for the laser wavelength λ and an acquired spectrum with a certain frequency shift ($f^{\theta A}$) for the $R\Theta TA$ scattering (angle: $\boldsymbol{\theta}$) the following expression (Eq. (43)) can be used.

$$\mathrm{v}_{\mathrm{a}}^{\theta \mathrm{A}} = \frac{\omega^{\theta \mathrm{A}} \cdot \pi \lambda}{\sin(\frac{\Theta_s}{2})} \tag{43}$$

The longitudinal rigidity modulus M` can then be achieved by Eq. (39), Eq. (40), respectively.

5.0.1 Influence of plate diameter, material and surface to BR-spectrum and rheological results

The rheological plate-plate geometry PP25 that is used so far gets polished out of two reasons. On one hand, the latter application of the $R\Theta TA$ scattering geometry to the rheometer needs a good reflecting surface and on the other hand, the signal height of the Brillouin shift frequencies might increase due to less randomly scattered light in the sample due to the surface of the PP25 plate. Further, it will be interesting to see which influence this may have to the rheology values themselves due to the smoother surface. As depictured in Figure 27, Figure 99 shows two PP25 plate-plate geometries, one in original version where the striae from construction are visible (left) and the polished one (right).

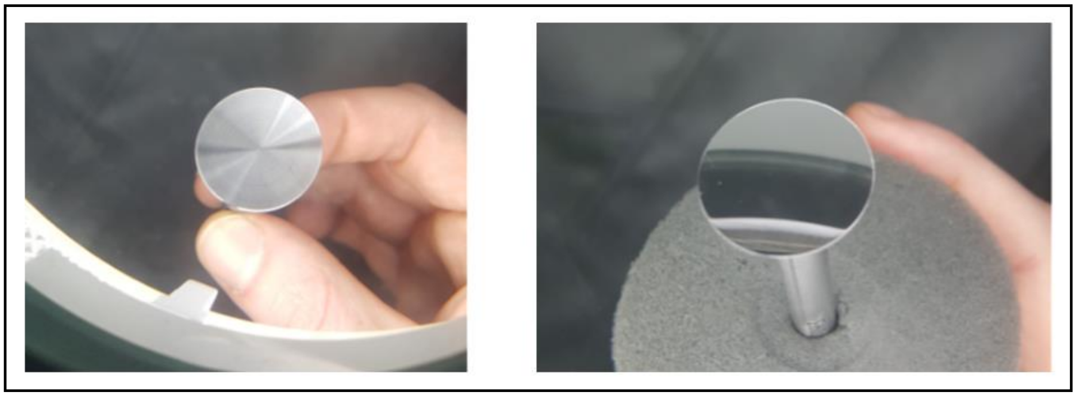

Figure 99: Picture of PP25 geometries, left a common plate-plate geometry where the rings of manufacturing are still visible; right, the polished PP25 geometry used in further experiments.

A comparison for both plates is exemplified shown in Figure 100. The distilled water sample at set 10°C (rheometer temperature control) is put into a 1 mm gap and the spectra are collected for 4 min. As a result, the background of the spectra increases, some inner peaks (RIθA) appear and the back-scattering signal is strengthened.

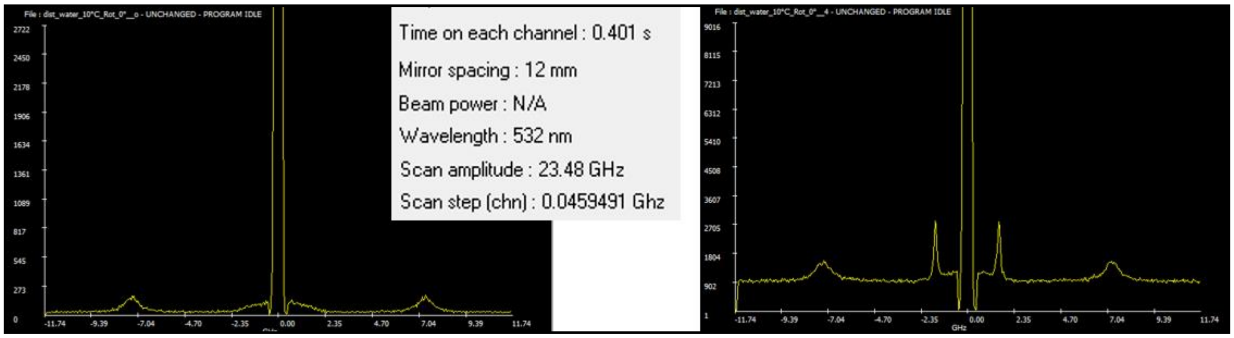

Time on each channel : 0.401 s
Mirror spacing : 12 mm
Beam power : N/A
Wavelength : 532 nm
Scan amplitude : 23.48 GHz
Scan step (chn) : 0.0459491 Ghz

Figure 100: Exemplary spectra for distilled water at 10°C from the Ghost software. Measurements with a normal PP25 (left) and right, with the polished plate geometry. The acquisition time is 4 min for each and the drastically increase of signal quality is visible in comparison.

In order, to experimentally determine the range of shear rates for which reliable data can be recorded with the 25 mm polished steel top plate (PP25), a comparison is executed and shown in Figure 101.

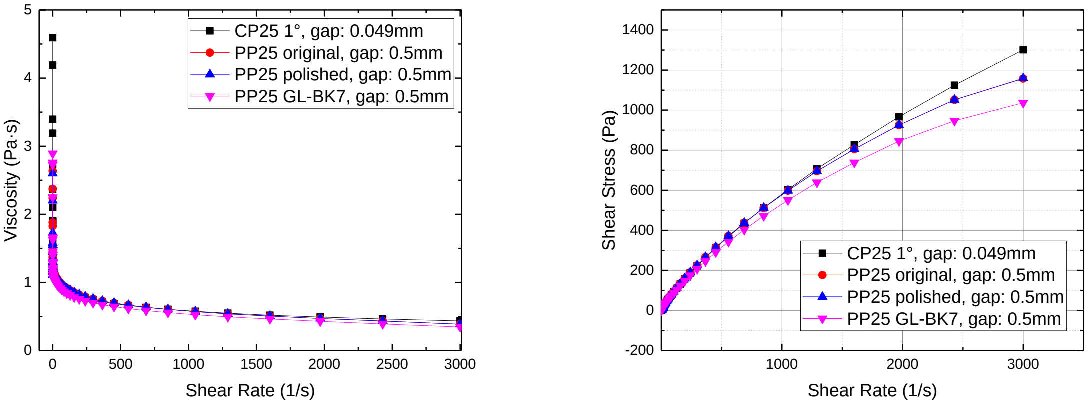

Figure 101: Rheological measurements of viscosity and shear stress for increasing shear rate and different rheological geometries (a cone plate geometry (CP25 1°), an original and polished plat-plate geometry (PP25) and a glass plate (PP25-GL-BK7)) for the PVP 2.5 mass percent PEG sample in a 0.5 mm gap (except the CP plate with 0.049mm) and an applied laser radiation of 10 mW into the sample.

Measurements with an unpolished (PP25), a cone plate geometry (CP25 1°, gap size 0.049 mm) and a glass plate (PP25 GL BK7) have been performed with a gap size of 0.5 mm (0.049 mm for the CP geometry) and the laser beam send into the sample has 10 mW at a sample temperature of 25°C (rheometer control). The rheological measured values for the viscosity and the shear stress are plotted over the shear rate in previous Figure 101. To give a better picture the measurements are plotted also logarithmically in the following Figure 102.

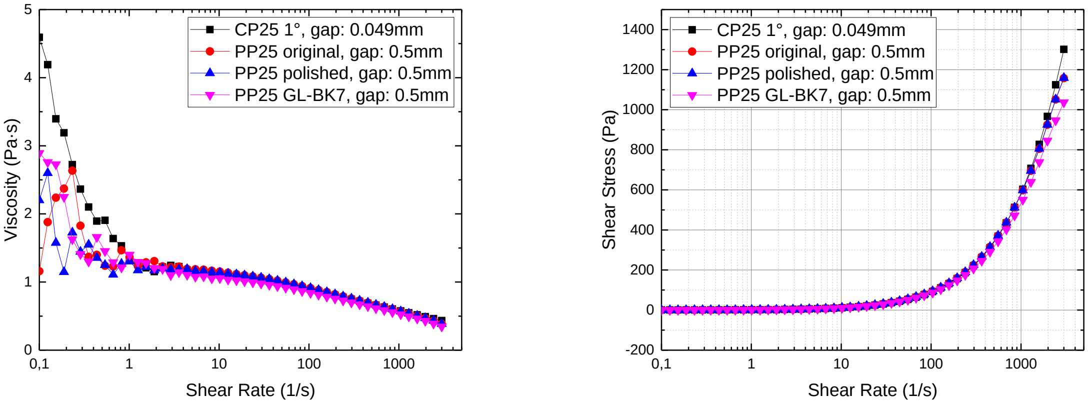

Figure 102: Logarithmical depiction of Figure 101.

Figure 102 shows the comparison of the different rheo-geometries plotted logarithmically. The shear thinning behavior for the material is occurring at high shear rates, so the regime of interest is shown in the Figure 103.

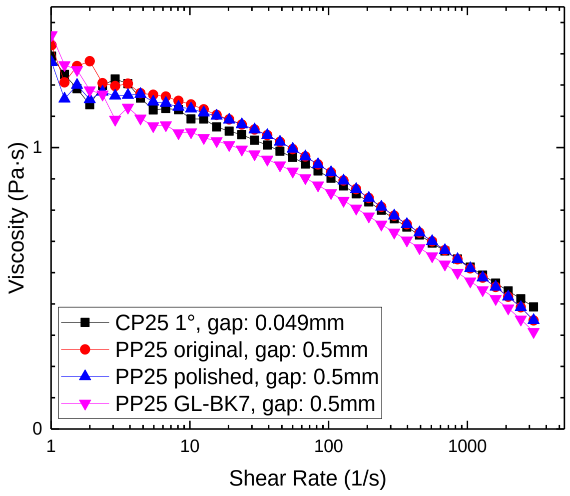

Figure 103: Viscosity curve for different rheological geometries shown in the shear rate regime of interest.

All measurements show the shear thinning behavior of the material. Further, the plate geometries compared to the cone-plate geometry have the same behavior for shear rates over 10 s^{-1}. In this regime, all tested plates show comparable results, so the polished PP25 can be used without influencing the rheological results of the experiments.

Nevertheless, comparing the polished PP25 geometry further to the maximum diameter geometry fitting into the optical access ground plate (and heating device) of the rheometer, which is the PP43 GL HT glass plate, gives following plots (Figure 104 and Figure 105). One can see that the bigger diameter plate delivers values over the whole range of shear rates and they appear to be a bit smaller as with the PP25 plate.

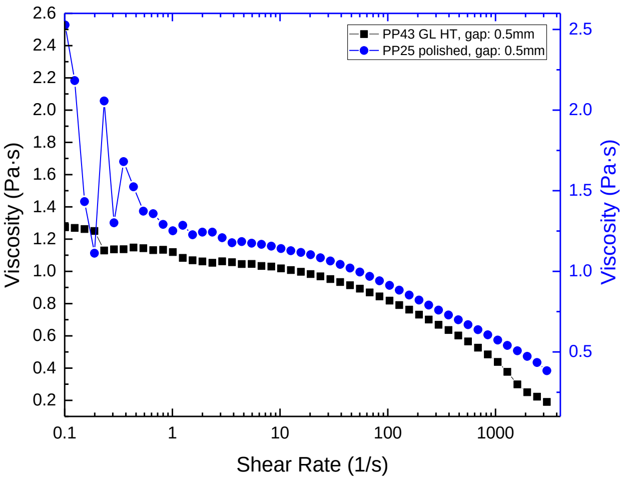

Figure 104: Comparison of rheologically measured values for viscosity for a polished PP25 rheo-geometry (blue dots) and a PP43 glass plate (black squares) for increasing shear rate.

The plate with greater diameter is able to give more precise measurements due to the rotational rheological technology. Meaning, having a bigger diameter so area of surface and interface interacting with the sample, leads to more sensitive measurement results.

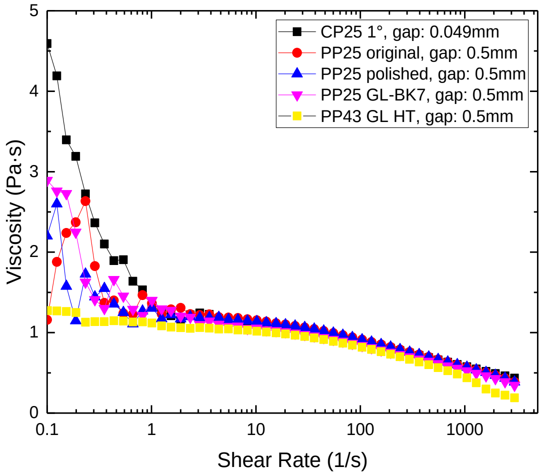

Figure 105: Overview of all rheological geometries tested and plotted for comparison over increasing shear rate.

However, comparing all the plates again, the shear rate regime of interest, which is set to be between 10 s^{-1} and 3000 s^{-1} gives a comparable result for the 25 mm diameter plates. Therefore, it can be confirmed that for these experiments the plate material has no influence on the results as the glass plates give similar values for the viscosity curves as well like Figure 105 shows in comparison.

5.0.2 Real temperature in the sample, its extrapolation and control

It can be that the temperature differs to the set values of the rheometer control as it could be influenced by the modifications of the housing of the MCR302 rheometer, which are necessary to gain optical access. To control the temperature in the sample more precisely, a hood (H-PTD200 from Anton Paar) is installed. The hood is purged with air at a flow rate of 180 l/h. In order to find the conditions for reliable temperature measurements a PT100 temperature probe is introduced into the sample. Figure 106 gives a picture from below, where the temperature sensor is visible and besides, a sketch of the H-PTD200 hood and set-up (also depictured in Figure 26).

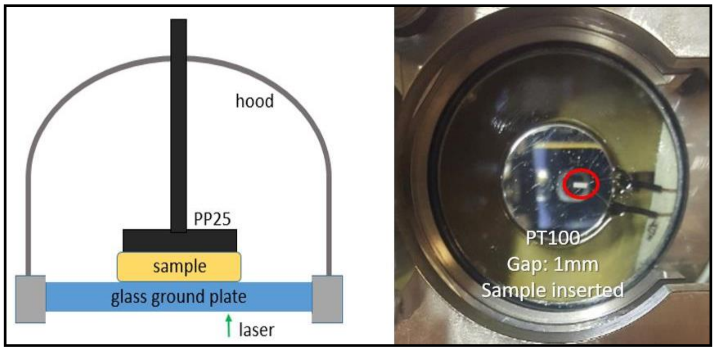

Figure 106: Left, illustration of the sample stage with H-PTD200 hood. Right, view of the sample stage from below. The top plate PP25 is set at a gap size of 1 mm to the lower glass plate. The transparent sample with the additional temperature sensor (marked with red circle) is in between.

Figure 107 shows an overview of the dependencies of two measured temperatures from the set temperature while the rheometer was set to a shear rate of 3000 s^{-1}.

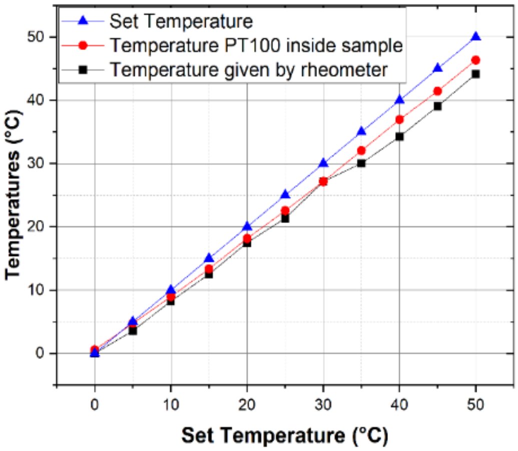

Figure 107: Comparison of temperatures. Blue triangles: set temperature in the rheometer software. Black squares: temperature measured inside the sample after the rheometer control indicates a stable temperature. Red circles: temperature measured inside the sample after 20 minutes.

It turns out that the sample temperature differs from the temperature indicated by the rheometer software and that a waiting time of about 20 minutes is needed to guarantee steady conditions in the temperature range used. Therefore, for all measurements presented in the latter, a correction of the temperature indicated by the rheometer software has been done and a waiting time of 20 minutes after changing the sample temperature has been respected. All rheological measurements have been performed without the PT100 temperature probe.

While the measurement the laser beam is introduced to the sample to set real experimental conditions. The laser beam is focused by the objective lens L3 (Figure 54). The laser beam enters in one side of the lens and is reflected back by the sensor and PP25 onto the other side of the lens to get lead out of the detection path (Figure 108). The applied laser power is 10 mW.

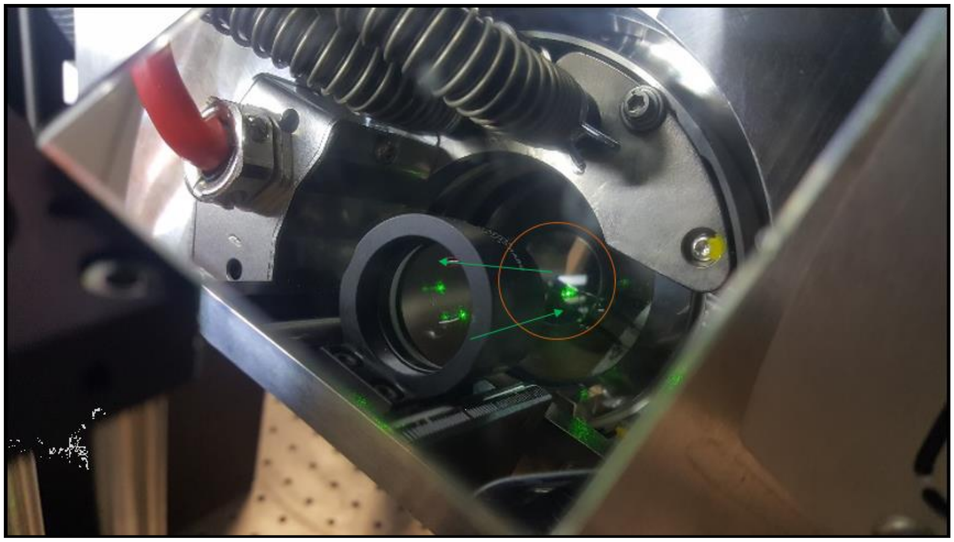

Figure 108: Picture of the objective lens L3 (Figure 54) focusing the laser beam (10 mW) onto the temperature sensor in the 1 mm gap of the rheometer (the PP25 is surrounded by the circle). The beam is send through one half of the lens and directed back through the other side to get the main beam out of the system (indicated with the arrows).

Approaching cold temperatures problems with the spectra occur as the signal strength is decreasing strongly. After researching this issue, it is found that by cooling, the lower glass plate nearly gets frozen, further is fogged and condensed water is attaching to it what also falsifies the rheological values of viscosity (see Figure 157). Figure 109 shows the lower glass plate for temperatures of 0°C, 5°C, 10°C and room temperature of about 23°C (meaning without heating).

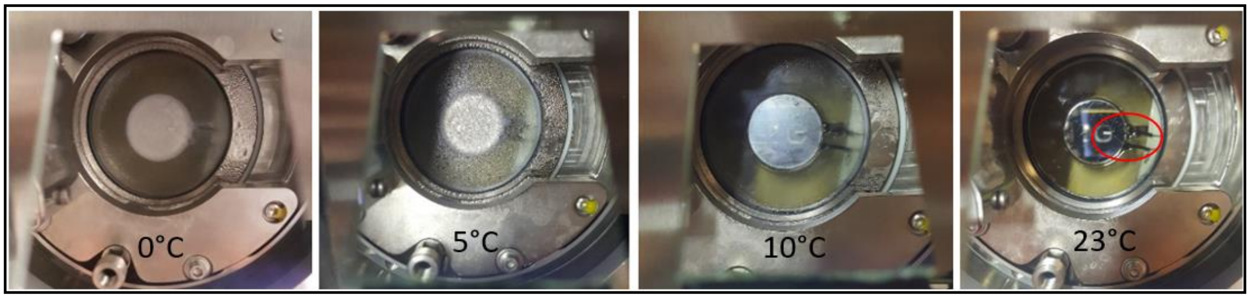

Figure 109: Pictures of the lower glass plate of the rheometer for low set temperatures from left: 0°C, 5°C, 10°C and room temperature of 23°C. Right, indicated with the red circle is the inserted temperature sensor that is only really visible at temperatures over 10°C.

This implies that for further experiments with this set-up a temperature regime over 10°C should be used as the influence of the freezing and fogging of the lower glass plate is too strong and will distort the measurements regarding the frame of this work.

In order to give more precise values for the temperature, measurements with a PT100 temperature element and an Oxford temperature controller are implemented and the values for the temperatures are plotted in Figure 110. An extrapolation is made to apply it to the later experimental results. While testing the extrapolation and compare it with the measured values between 25°C and 40°C it was found that the best extrapolation is extracted with the values of temperature over 20°C (as indicated in Figure 110).

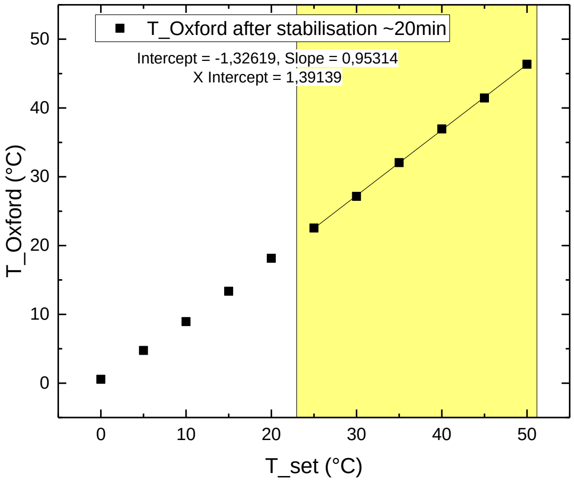

Figure 110: Linear fitting of the temperature values measured with the PT100 sensor and the Oxford controller in the sample stage of the rheometer with the PVP 2.5 mass percent PEG sample.

Giving the values of a linear fit equation (Eq. (44)), m_{lf} being the slope of the function and b_{lf} the interception of the y-axis:

$$y = m_{lf}x + b_{lf} \tag{44}$$

$$y = 0.95x - 1.326$$

This relation now allows us to extrapolate further temperatures (x). Table 10 gives an overview of all measured temperatures (after 20 min.), further, measured viscosities and frequency shifts at 3000 s^{-1} shear rate measured simultaneously with rheology.

Table 10: Overview of temperature measurements from 0°C to 50°C. The temperatures set at the rheometer are shown as the measured ones after a stabilization time of 20 min for each temperature.

T set (rheo.) / °C	**T (Oxford) / °C**	**T extrapolated / °C**
0	0.55	
5	4.75	3.44
10	8.95	8.21
15	13.35	12.97
20	18.15	17.73
25	**22.55**	**22.50**
26		23.45
27		24.41
28		25.36
29		26.31
30	**27.15**	**27.26**
31		28.22
32		29.17
33		30.12
34		31.08
35	**32.05**	**32.03**
36		32.98
37		33.94
38		34.89
39		35.84
40	**36.95**	**36.79**
45	41.45	41.56
50	46.35	46.32

Plotting the viscosity and Brillouin shift frequencies over the temperature it gives following plot (Figure 111), which will be discussed later in detail. For now, the optical parameters of the scattering volume shall be discussed.

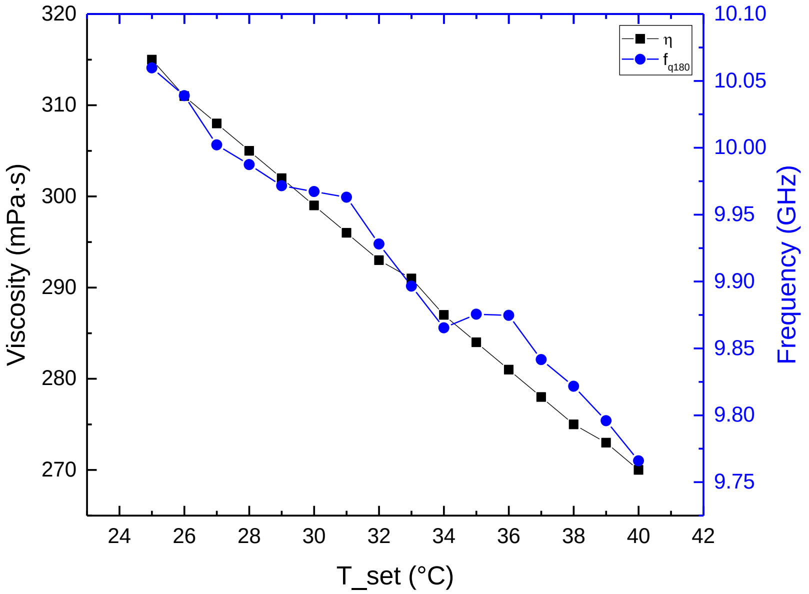

Figure 111: Analog viscosity and Brillouin measurements for 3000 s^{-1} shear rate, plotted over extrapolated values for temperature at the edge of the rheological geometry.

5.0.3 Dimension of the scattering volume, identification of the position of the scattering volume in x-y-z plane and influence of laser power to signal strength

Regarding the sample thickness of 0.5 mm (given by the gap between the rheometer plates), the dimensions of the scattering volume should be just a fraction of this value in order to be able to move it freely inside the sample volume. As the chosen sample thickness is 500 µm, the focal spot length should have a maximum dimension of about 50 µm. In technical optics the focal spot dimensions for a Gaussian beam can be expressed as follows (Eq. (45)). Other approximation equations[7,8] which also are commonly used (where the diameter is been used and k=1) lead to values that differ by about 10%. Here the radius of a focal spot can be formulated as follows [140]:

$$\omega_0 = \frac{\lambda}{\pi * k_{bq} * \Theta_O} \tag{45}$$

---

[7] www.researchgate.net/post/How_to_determine_the_focal_spot_size_of_an_objective/611fa4d30f8ef3651626b990/citation/download

[8] www.newport.com/n/gaussian-beam-optics

where λ is the wavelength, k_{bq} the beam quality factor (1< k_{bq} <1.1 for the Verdi G2) and Θ_O the angle of the beam`s edges to focus (Eq. (46)) on the optical axis:

$$\Theta_O = \arctan(\frac{\omega_{ObjL}}{f_{ObjL}}) \tag{46}$$

with ω_{ObjL} the beam radius of the beam approaching the focusing (objective) lens and f_{ObjL} the focal length of it as illustrated in Figure 112.

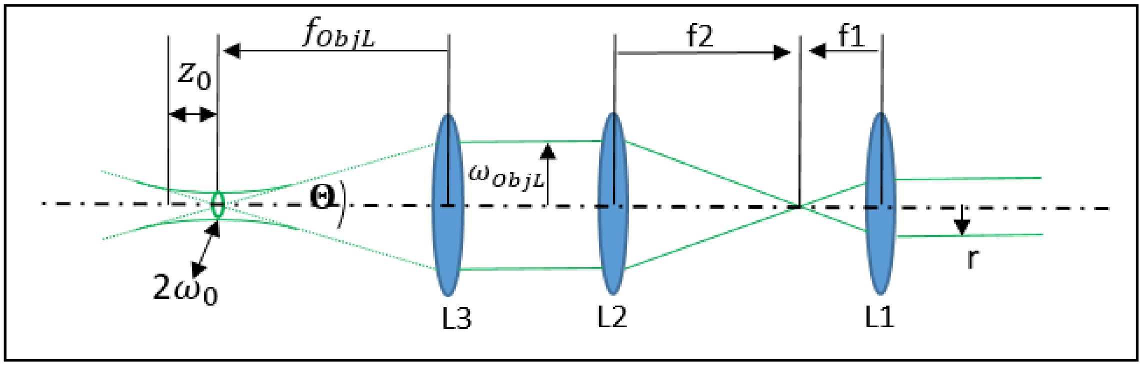

Figure 112: Illustration of the focal spot parameters (left) and the telescope beam expanding optics (right).

The focal spot radius (Eq. (47)) can then be expressed as:

$$\omega_0 = \frac{\lambda * f_{ObjL}}{\pi * k_{bq} * \omega_{ObjL}} \tag{47}$$

and the corresponding focal length z (or Rayleigh length z_R for a Gaussian beam, where z_0 goes from f direction z till it reaches a value of $\sqrt{2}\omega_0$ [45]) shown in Eq. (48):

$$z = 2 * z_0 = 2 * \frac{k_{bq} * \pi * \omega_0^2}{\lambda} \tag{48}$$

Prism P1 (Figure 54) has a reflecting area with the dimension of 3 mm * 4.2 mm, whereas the given laser beam radius is 2.3 mm, so the maximum radius of the beam after the prism is about 1.5 mm (r in Figure 112). A widening of the beam diameter in front of the objective lens is required to achieve smaller focal parameters. Two lenses (telescope optics L1 and L2) are set in front of the objective lens (L3). Due to the 1" optics used in the set-up, the aperture of the lenses is limited to 25.4 mm. The beam radii and focal lengths are illustrated in Figure 112 and the relation between them (Eq. (49)) can be formulated as follows:

$$\omega_{ObjL} = r * \frac{f_2}{f_1} \tag{49}$$

The combination of an f = 25.4 mm optics (L1) and a f = 140 mm lens (L2) gives a beam radius ω_{ObjL} of 6.2 mm, which corresponds to a diameter of 12.4 mm and fits the condition. Having the maximum beam radius before focusing and the minimal focusing length of 60 mm for the objective lens (due to construction of the rheometer) as well as the laser beam parameters of quality (k_{bq} = 1.05 as middle value), an estimation of the focal length can be given (Eq. (50)) as follows:

$$z_0 = \frac{\lambda * f^2}{\pi * k_{bq}} * \frac{1}{\omega_{ObjL}^2} = \frac{1}{\omega_{ObjL}^2} * \frac{532 * (10^{-9})\ \mathrm{m} * 0.06^2\ \mathrm{m}^2}{\pi * 1.05} = \left(\frac{1}{\omega_{ObjL}^2\ (\mathrm{m}^2)} * 0.58059 * 10^{-9}\ \mathrm{m}^3\right) \tag{50}$$

The formulation Eq. (50) now can be used to calculate the focal spot length for the used set-up by setting the beam radius ω_{ObjL} before focusing. This leads to a focal length z of **32.23 µm** for a beam radius of 6 mm, before focusing, which is sufficient for the following experiments. The corresponding focal diameter $2\omega_0$ is **3.2 µm**. For the measurements presented here, no slit or pinhole has been used in the set-up shown in Figure 54. Therefore, the focal length of 32 µm is not equal to the dimensions of the scattering volume. It moreover indicates the region where most of the information is gathered from. The samples investigated are expected to show heterogeneities due to shear induced structuring on length scales far below the phonon wave length. Therefore, we do not expect a falsification of phonon frequencies by the fact that Eq. (37) no longer holds as e.g. discussed in [138].

The positioning of the focal spot in the xy-plane is realized by setting the focus to the outer diameter (edge) of the plate geometry and visually position it from the outside direction to the center, as the beam is not going through the sample (in z-direction) anymore (indicated in Figure 113) it gets reflected from the PP25.

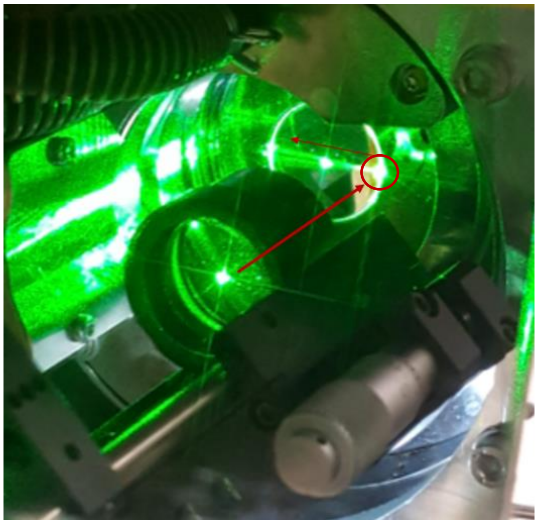

Figure 113: Picture showing the lower glass plate of the rheometer. The objective lens (L3) focus the beam into the sample volume. The laser beam was translated in xy-plane to the edge of the geometry. At the very end of the PP25 edge the laser beam gets reflected in the trim belly and lead over the PP25 plate as visible in the picture. Focal spot position indicated with red circle.

Now with spectroscopic measurements the region of the boarder and the trimming sample belly at the edge of the geometry can be examined. With comparison of the signal height fitting values to the ones inside the sample, one gets the quite exact position at the edge of the geometry. From this position the objective lens is moved with an opto-mechanical element (translation stage) in direction center of the PP25 (so the sample stage) as depicted in following sketch (Figure 114).

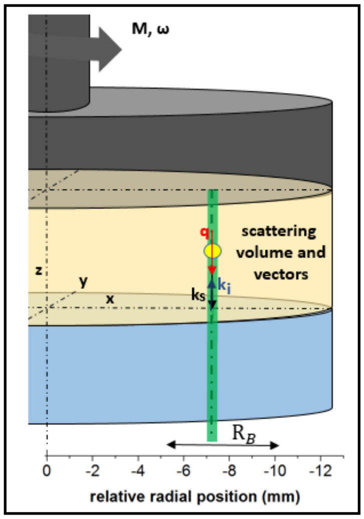

Figure 114: Schematics of the focal spot position and the movement in radial direction (x) as well as the incoming photon wave vector k_i*, the reflected wave vector* k_s *and the wave vector of the measured acoustic wave vector* q*. This is just a simplified view, as* k_i*,* k_s*and* q *are tilted about an certain angle, due to the set-up (explained in the text below and illustrated in Figure 115.)*

The 180° backscattering technique due to the chosen set-up (-using each one half of the objective lens for focusing and leading away the main laser beam) is tilted. The angle of the incoming laser beam to the scattering volume is changed, which is explained in the following briefly.

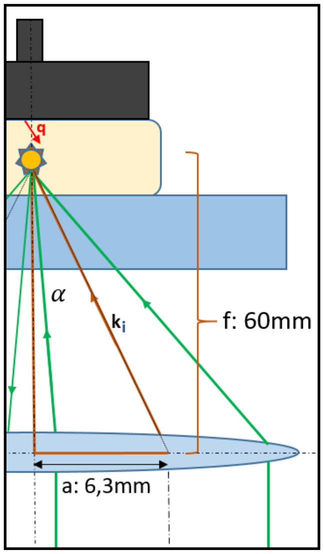

Figure 115: Illustration of the scattering volume, the incoming wave vector k_i *(which lies in the center of the incoming beam, indicated with the green arrows) under angle* α *and the position where the beam center hits the lens as well as the focal length of the objective lens L3. The orientation of the acoustic wave vector* q *is in opposite direction as* k_i*.*

The beam with a radius ω_{ObjL} is focused by the lens L3 as the beam`s center hits the lens at a distance a_i of 6.3 mm away from its center (Figure 115 and Figure 108). The angle of incidence α_i can be calculated with trigonometrical formulas (Eq. (51)) as follows:

$$\tan \alpha_i = \frac{a_i}{f} \tag{51}$$

The angle of incidence α_i is calculated and appears to be 5.99°. To be exact, the q-vector in the scattering volume of the 180° backscattering is deviated plus or minus 6° by the chosen beam path.

To be more precise, there are at least two different refractive indices and interfaces, so there will be some refraction that changes the angle of incidence further (Figure 116).

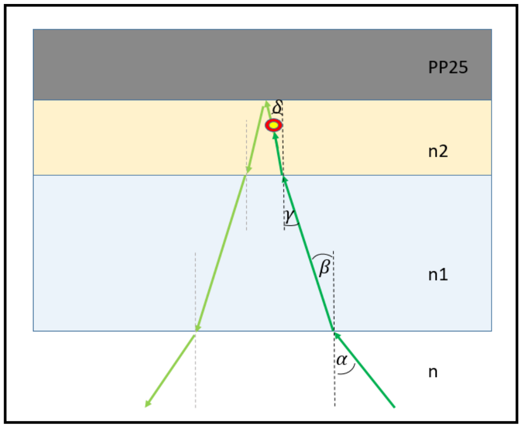

Figure 116: Sketch of the sample (yellow, refractive index: n2) and the scattering volume inside (red dot) in between the PP25 and the bottom glass plate (n1). The laser beam (green) coming from air (n) gets refracted two times, till the scattering volume is reached and further gets reflected at the PP25 and is lead out of the sample area (light green). For this case n < n1 < n2.

With Snell's law of refraction [55]

$$n_1 * \sin(\alpha_i) = n_2 * \sin(\beta_i) \tag{52}$$

it can be calculated how much the beam deviates due to the different refractive indices (Eq. 51). Previously shown, the angle of incidence $\boldsymbol{\alpha}$ is 5.99° in air. The angle β_i is in quartz glass (refractive index n_1 = 1.46) and calculated with Eq. (52) to be 4.098°, rounded to 4.1°. As γ_i and β_i are corresponding angles they have the same value. The angle δ is inside the sample volume at 22.5°C (extrapolated temperature) with a refractive index n_2 of 1.4705 and follows to be 4.0706°, rounded to be still 4.1°. Regarding the sample and its refractive index, which also depends on the temperature, the two maximal values are discussed. At a temperature of 22.5° the angle will change to 4.08° whereas at a temperature of 52.5° the angle will be 4.11°.

That means, for a temperature difference of 30°C there can be a shift in angle of incidence (q-vector) due to refractive index variation of 0.03°. Therefore, it can be stated say that the q vector is tilted 4.1° to the optical z-axis. This has no major effect on the measurements as the very small tilt in angle, due to change of temperature of the sample for 30°C, implies as well. Nevertheless, this shall be mentioned to keep the precision of this work.

As shown in Figure 54 the scattering volume can be translated vertically between the rheometer plates by moving lens L3. In order to calibrate the position of the scattering volume, Brillouin spectra have been recorded for different vertical positions *z* of the scattering volume.

Figure 117 shows the measured Brillouin frequency shifts as well as the signal heights as a function of *z* – both for no shear (0 s^{-1}) and high shear (3000 s^{-1}).

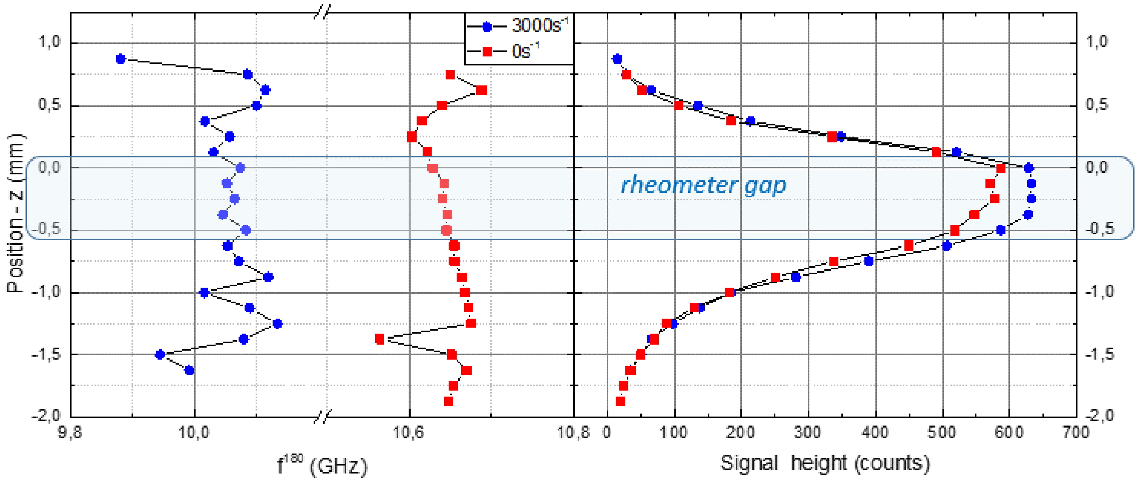

Figure 117: Brillouin spectroscopic measurements during vertical movement of the scattering volume. Left: Brillouin frequencies f^{180}. Right: corresponding signal height values.

Even when the scattering volume lies mainly outside the sample, e.g. mostly in the lower glass plate, the Brillouin frequencies attributed to the smaller sample volume remain the same. The Brillouin frequencies for the glass plates lie outside the chosen FNR of the spectrometer so they do not interfere with the measurement. Therefore, the frequency shifts give no precise information about the position of the scattering volume (Figure 117, left). In contrast to this, the signal height is directly proportional to the amount of sample material, which lies inside the scattering volume. This means that the evaluation of the signal heights allows ensuring a more precise positioning of the focal spot in z-direction. For the measurements discussed in this work, the focal position is set to the middle of the gap between the rheometer plates, so 250 µm above the glass ground plates' upper surface. It should be emphasized that the application of shear has no major influence on the signal heights and the position of the scattering volume (Figure 117, right). The recorded frequencies (Figure 117, left) differ to each other with and without shear what is an indication that Brillouin scattering is sensitive to shear thinning. Therefore, this method allows having a precise positioning of the focal spot in z-direction.

To investigate the connection of induced laser power to the scattering process in the sample to the acquired signal quality, the signal height values are recorded for increasing laser power. This is measured with a power meter (from Coherent) in front of the sample stage and is plotted in following Figure 118 (maximum signal height counts (red) – underground counts (blue)). Each spectrum was recorded for 4 min. The sample material, depending on the gap size, is put with a pipette on the middle of the rheometer ground plate with just a tiny bit more material as the calculated sample volume of the cylinder (space between the rheometer plate-plate geometry and the ground plate) so the trimming-belly will apply. The PP25 geometry gap size is fixed at 0.5 mm and the hub is closed. The air circulation is set to 180 l/h as given from the manufacturer (Anton Paar).

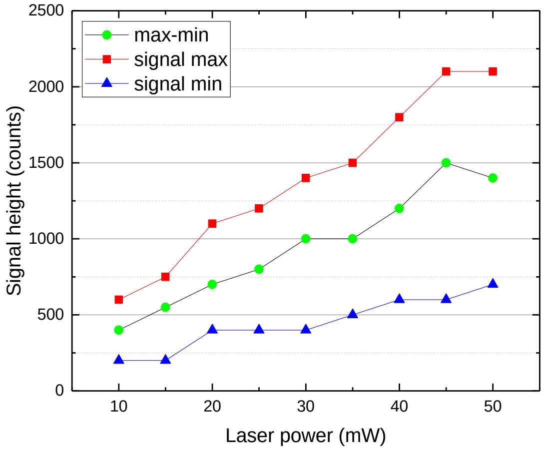

Figure 118: Plot of signal, noise and its difference, over increasing laser power. The laser power is measured with a power meter (Coherent) in front of the sample stage. Red dots indicate the Origin fit data for signal height, as blue, the noise or background signals and green, the difference of both as indicated in Figure 23.

The fit height of the signal is increasing with temperature, as it is the case for the signal and noise counts. The colors of the plot (Figure 118) coincide with the ones indicated in Figure 23. To make it more visible, the spectra collected are depictured as waterfall plot in the Figure 119. The figure implies the raising of signal height with increasing laser power.

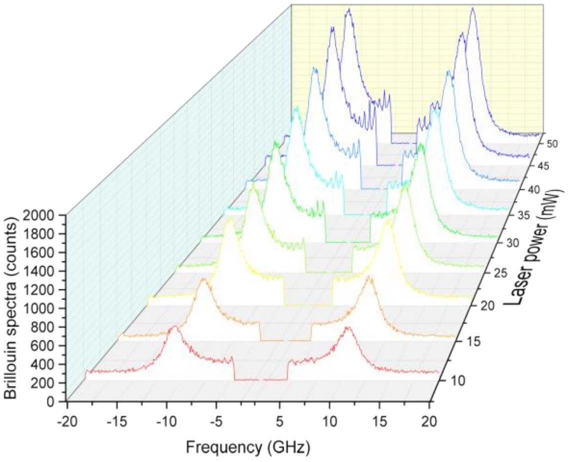

Figure 119: Waterfall plot of collected Brillouin shift spectra for increasing laser power introduced into the sample volume. The frequency range (Rayleigh peak) from -1.8 GHz to 1.8 GHz is cut out to better illustrate the spectra.

Nevertheless, there is an increase in spikes around the Rayleigh peak (in the central area) that can lead to problems in signal evaluation. Further, the photon counter (detector) has always to be used in care of not damaging it. The choice of laser power used for the scattering process falls to 25 mW. It is in a good Signal to Noise regime. Smaller powers are hard to evaluate and higher ones not necessary and wanted. Small invasive energies are chosen to keep the door to biological applications open and further security and safety issues small.

5.0.4 Brillouin shifts for temperature change and applied shear field

A simultaneous rheology and Brillouin scattering measurement as a function of temperature for a constant shear rate $\dot{\gamma}$ of 3000 s^{-1} has been performed. The change of temperature follows a change of refractive index, which was measured with a refractometer and is plotted additionally as blue dots in Figure 120 (data shown in Figure 111 previously).

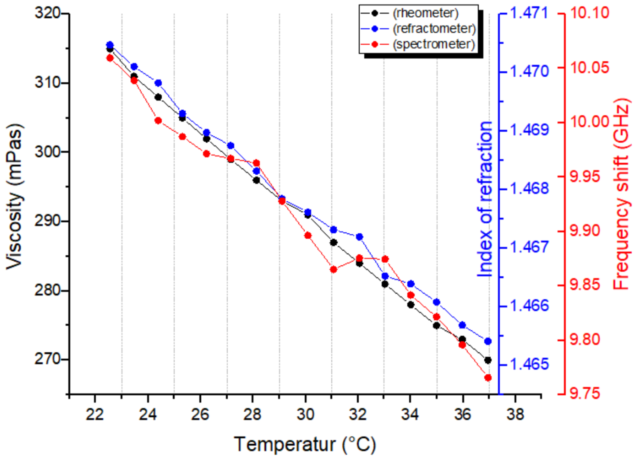

Figure 120: Viscosity recorded with the rheometer plotted over increasing temperature. Blue, the index of refraction measured with a refractometer and red, the frequency shift gathered with the Brillouin spectrometer.

Starting from 37°C downwards, the spectra are collected, each for 4 min and the frequency shifts are additionally plotted (red dots) in the graph. At last, the viscosity measured with the rheometer is plotted as black dots.

Figure 120 indicates that the built set-up is able to picture quite small changes of index of refraction n as well as the viscosity. With rising temperature, the viscosity, index of refraction and the Brillouin frequency shifts are decreasing constantly. The change of the refractive index n is not that high that it is the reason for the Brillouin frequency change what was shown previously with the change of index with temperature and related derivation of the laser beam entering the sample. The change of viscosity is the major effect leading to the shifts, which is going to be shown in the following.

At a temperature of 22.5°C the frequency shift is about 10.05 GHz whereas it is 9.85 GHz at a temperature 10°C higher (32.5°C), which gives a frequency shift of about 0.3 GHz for 10°C temperature difference.

With the formula of the hyper-sound velocity (Eq. *(38)*) having the measured refractive indices n of 1.4705 at 22.5°C and 1.467 at 32.5°C, calculating the hyper-sound velocities for the two temperatures in example.

@ 22.5°C: $\frac{532\,nm}{2*1.4705} = 180.9\,nm * 10{,}05\,GHz = \mathbf{1817.9\,m/s}$

@ 32.5°C: $\frac{532\,nm}{2*1.467} = 181.3\,nm * 9{,}85\,GHz = \mathbf{1786\,m/s}$

This gives a delta of sound velocity of 31.9 m/s for 10°C temperature shift.

So the shift of sound velocity per 1°C is about 3.19 m/s.

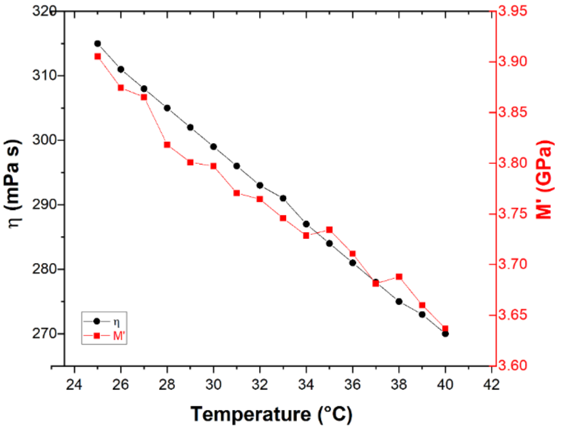

Figure 121: Simultaneous measurement of η and M' as a function of sample temperature. Shear rate $\dot{\gamma}$ = 3000 s^{-1}. The scattering volume of the Brillouin measurements is situated close to the edge of the rheometer plates

This indicates the sensibility of the Brillouin spectroscopy to change of temperature and viscosity. Plotting the values for viscosity and the longitudinal rigidity modulus *M'* gives Figure 121, which shows η measured by rheology (macroscopic value) and *M'* (Eq. 38, 39) measured by Brillouin spectroscopy (scattering volume near the edge of the rheometer plates as indicated in Figure 33).

As expected, both elastic susceptibilities diminish with increasing temperature. It should be emphasized that the viscosity reflects the answer of the system to pure shearing whereas M' is the susceptibility related to a purely longitudinal elongation [141]. Moreover, the viscosity is a quasi-static quantity whereas the longitudinal modulus has been measured at frequencies in the GHz range where the system is dynamically clamped. As discussed in the introduction, the modulus measured by Brillouin spectroscopy at high frequencies detects the effective "spring constants", which determine the propagation of the longitudinal, thermally induced sound waves. It also contains the temperature dependency of the mass density (Eq. 38, 39).

The temperature dependent measurement shown in Figure 121 shows that both elastic susceptibilities show a similar behavior. We must emphasize that there is no direct causal relation between both susceptibilities. Figure 121 demonstrates that the temperature dependency of both susceptibilities can be resolved by the presented set-up. The combined technique shall now be applied to a measurement where the shear rate is varied in the range where shear thinning can be detected for the system under study.

5.0.5 Brillouin Rheology and its shear field sensitivity

To investigate the shear field dependency, the rheometer is set to increasing shear rates, each set for 20 mins, then the Brillouin spectroscopic measurements are started (for each data point there are three measurements for 14 mins).

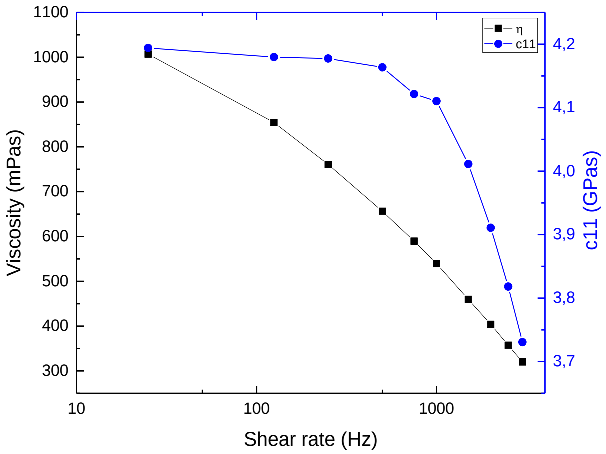

Figure 122: Plot of viscosity (rheometer) and c11 (Brillouin spectrometer and density meter) over increasing shear rate.

The gap size is set to 0.5 mm and the temperature to 25°C which corresponds (as discussed previously) to 22.5°C and before the experiments are started a minimum of 1 hour tempering is executed. The room temperature is 23°C so the influence of temperature from outside to the sample is minimized. The laser is set, so the beam entering the sample volume is 25 mW and the focal spot position is at the edge of the rheo-geometry. The average values of the three spectra are calculated and the longitudinal component c_{11} of the elastic modulus is plotted in Figure 122 (blue dots) over the shear rate (logarithmically) as the rheologically measured values for the viscosity are plotted as well (black squares). The longitudinal component of the elastic modulus c_{11} shows a softening only at shear rates higher than 500 s^{-1}. It can only be speculated if this is due to the fact that the q-vector of the longitudinal wave is perpendicular to the normal of the rheometer plates and that ordering of molecules parallel to the rheometer plates occurs only at higher shear rates. This interesting scenario can be investigated with an improved set-up, which allows to record all components of the elastic stiffness tensor by using different scattering geometries.

5.0.6 Comparison of different radial positions of the scattering volume

The shear field inside a sample that is measured with a plate-plate geometry is inhomogeneous (as introduced in the rheometry section). Having acquired and discussed a measurement at the outer radial position (at the edge of the rheo-geometry) the investigation leads to two further experiments at a central position inside the sample as well as a relative middle (between center and edge) position. However, as the shear field is not homogeneous, the measured viscosity values are fitted, to be able to plot the relative viscosity for the three positions over the shear rate, which is produced by the different relative angular velocities of the rheo-geometry at different radii.

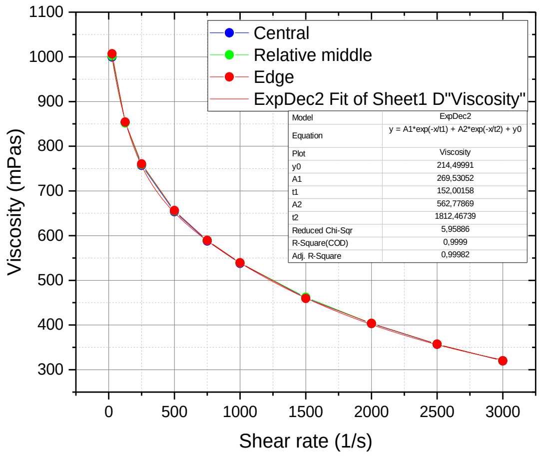

Figure 123: Exponential fitting of viscosity values (rheological) over shear rate for three measurement sequences (Brillouin spectroscopy at different radial positions of the scattering volume in the sample).

The dynamic viscosity values for the three measurement series (for Brillouin spectroscopy at the different radial positions) are plotted over the increasing shear rate (Figure 123) and an exponential fitting is evaluated. The plotted graph indicates that the rheometer always measures the same average values of the viscosity at each shear rate. This implies a good repetition accuracy and that the laser radiation has no (rheological educible) influence to the outcome over time.

To acquire the relative shear rates for each radial position the curve is fitted (Eq. (53)) exponentially, which gives the corresponding equation:

$$y = A1 * e^{\frac{-x}{t1}} + A2 * e^{\frac{-x}{t2}} + y_0 \tag{53}$$

Calculating the relative shear rates at each of the measurement positions with their different radial distances, the relative viscosity for each radial position and rate can be derived and plotted. The positions of measurements are indicated with colored circles at different radial “positions” and coincide with the colored graphs in the latter.

The plot (Figure 124) shows that for the different radial positions of the plate-plate geometry, different values for the viscosity appear. As introduced (in the rheometry part of this work) the local shear rate at a radial position depends on the angular velocity applied by the rheometer and the gap size. Therefore, the change of this position leads to a change in the relative viscosity.

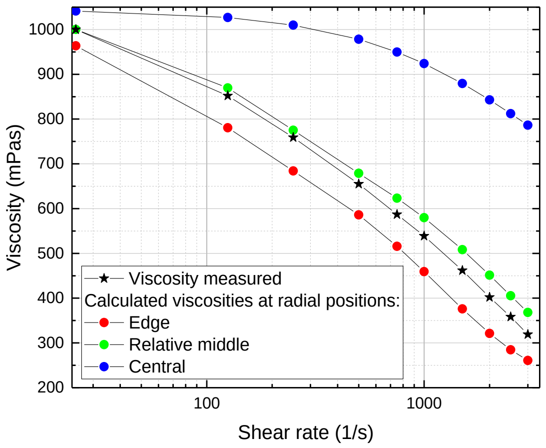

Figure 124: Plot of viscosity measured with the rheometer and a PP25 geometry. Colored the derived values for viscosity due to the radial positions as there are different relative angular velocities the curves depart from each other as depicted in Figure 125.

To give a better understanding Figure 125 shows the different radii and indicates the scattering volume in the sample.

The calculated viscosity values indicate that the shear rate has the highest effect on the sample at an outer radius than at the near center of the sample stage. The relative velocities at those positions are increasing to the outer diameter, respectively.

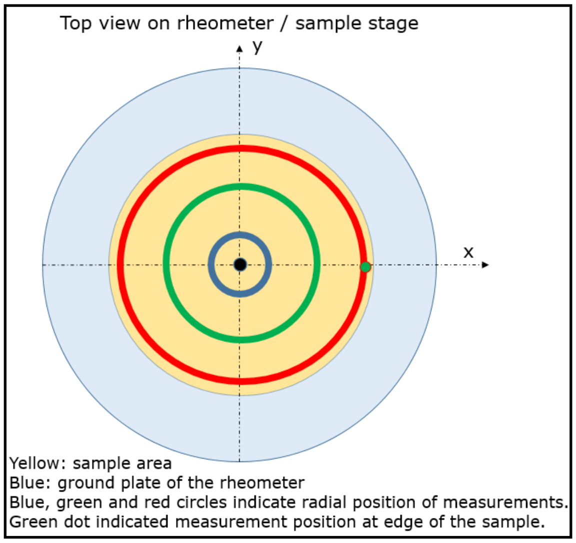

Figure 125: Sketch of the rheometer sample stage, the lower glass plate with sample loaded. The three different circles indicate the radial positions of the scattering volume as the calculated values of relative velocities.

The Brillouin Rheology measurements at three different radial positions are plotted as hyper-sonic modulus c11 and viscosity over increased shear rate. Interestingly it pictures the same behavior of the Brillouin measurements for high shear rates over 1000 s^{-1}. The calculated relative viscosity at the edge is smallest and increase to the edge position as it is pictured by the Brillouin spectral analysis.

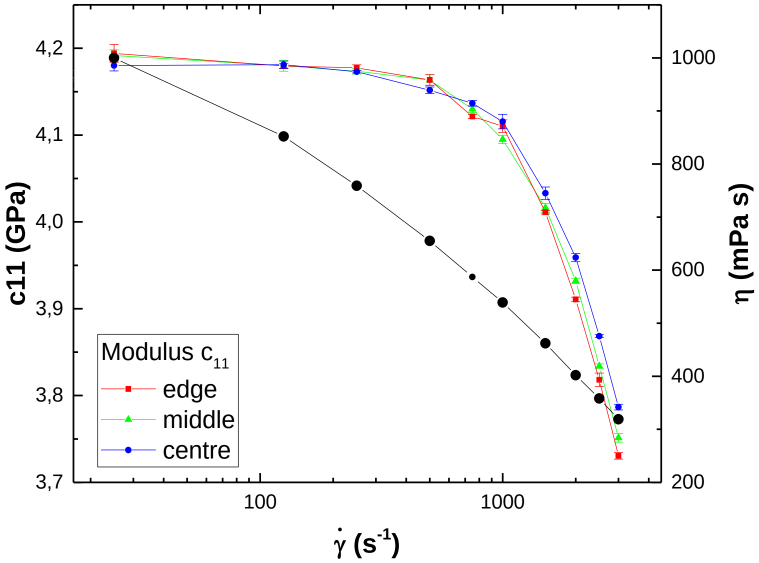

Figure 126: Viscosity and elastic moduli at different radial positions as a function of shear rate and for three different radial position of the scattering volume.

The most surprising result from the investigations with Brillouin spectroscopy can be seen when comparing measurements of c_{11} (or *M')* at different radial positions *r* (illustrated in Figure 125) in the gap between the rheometer plates. The three curves (open symbols in Figure 126 are measurements of *M'* at the center (*r* = 0.5 mm, blue dots); at the middle (*r* = 6.5 mm, green triangles) and near the border of the plate/plate geometry (*r* = 12 mm, red squares). All measurements show nearly the same dependency on the shear rate. This means that when the shear thinning, i.e. orientation of molecules starts at the extremities of the rheometer plates where the local shear rate has the highest values (Eq. 29), it influences also the parts of the sample with locally lower shear rates. If this effect is due to a different influence of the molecular orientation on the hyper-sound modulus than to the quasi-static viscosity deserves further investigations.

To conclude one can say that the hyper-sonic modulus shows same shear rate dependency at the different radial positions of the plates (plate-plate geometry), so the molecular alignment with respect to the plane normal is the same. Nevertheless, the difference in relative viscosity inside the sample can be pictured with Brillouin Rheology. The c_{11} values for the inner position are slightly higher in the area of interest (over about 1000 s^{-1}) than the ones for the middle position and the edge position, respectively. The Brillouin Rheology approach is also able to picture the small difference in relative viscosity and slightly different orientation of the molecules due to that.

Chapter 6: Conclusion and Outlook

A new method for mechano-spectroscopic rheology which combines a commercial rotational rheometer with Brillouin light scattering technology was developed. This method makes it possible to perform simultaneously both rheological and spectroscopic measurements of polymeric and soft matter materials, acquiring information about the viscosity and about hypersonic velocity or the longitudinal rigidity modulus M' of the elastic stiffness tensor for temperature variance, applied shear forces and different radial positions of the scattering volume (the spatial position of the measurement).

For this proof of concept, different materials have been tested regarding their rheological behavior to achieve a shear thinning with increased shear rate so that it is predictable that the molecule arrangement in the material will change. Further, a good scattering cross section is desired so that a good spectroscopic signal can be detected. Having found such a material in the polymeric compound of PVP with 2.5 mass percent PEG as a non-toxic easy to handle sample, analysis of the index of refraction and the density have been performed (Figure 38) with a refractometer and densitometer to acquire clear values for the sample material for the later evaluation of the elastic modulus.

The influence of different rheological geometries (Figure 105), their materials and surface structure/treatment have been compared to the rheological measurement values, and a polished PP25 plate-plate was chosen as it gave the best signal quality for the spectrometry and is not distorting the viscosity values in the shear rate regime of interest (Figure 104). The shear rate regime of interest for the PVP with 2.5 mass percent PEG sample material was found and set to be between 10 s^{-1} and 3000 s^{-1}.

During the investigation of the rheological behavior of the sample material, it was found that there are relaxation effects, which are hardly observable with the rheometer. Brillouin Rheology experiments are shown to be able to picture those relaxation effects at 25°C (Figure 94) and 40°C (Figure 96) after shearing the sample and stopping the rheometer while further observing and measuring the Brillouin shift frequencies spectroscopically. It was found, that the relaxation times are similar for the both temperatures, which is unexpected and should to be studied further.

Due to the changes of the hard cover of the rotational rheometer the temperature which is given by the rheometer has been audited. This was realized by putting a PT100 temperature probe into the sample volume and tempering it with the internal control of the rheometer (Figure 106). By implementing these experiments it was found that there is a derivation from the temperature control and the real temperature behavior is shown in Figure 107. It was also found that a tempering time of 20 min is needed so that a temperature is reached and stays constant (even the rheometer control suggests quite fast a constant temperature). Being under room temperature (about 20°C) brings some problems (having set the glass ground plate into the rheometer to have optical access) as it starts to show condensation-related effects until even freezing as pictured in Figure 109. These effects on the glass disturb the passage of the laser beam and hinder the collection of spectra with the Brillouin spectrometer, so a fixed temperature for most experiments of 22.5°C was chosen.

This is near room temperature, so there should be just very small, negligible temperature gradients from the outside to the sample.

The dimensions of the scattering volume (the focal spot of the incoming laser beam to the sample) was designed to be small enough to “scan” the sample volume even at the height of 500 µm (gap size of the rheometer plates). A technique was developed to position the focal spot (so the scattering volume) inside the *xy* plane of the sample volume as well as in the height of the sample (z-plane) by a combination of visual tests (Figure 113) and by using the signal height values of the collected peaks in the spectra (Figure 117).

The influence of the laser power applied to the sample regarding the signal quality has been tested (Figure 118) and a relative small power of 25 mW was chosen to be sufficient. This power was selected to not influence the molecules by the laser beam itself and allow for future measurements of biological samples. Further, attention was put in order to keep effects regarding the spectra collection small, which are spikes around the Rayleigh shift (Figure 119) due to an optical feedback in the system. These interfering effects can make the measurements useless as the stabilization of the spectrometer is stressed so much, that it loses its reference value and regulates wrong. So the experiment has to be stopped and the spectrometer calibrated to work proper again. A solution for an improved set-up is to take another laser light source with the equal parameters (like wavelength and bandwidth) for the use of the alignment beam path of the spectrometer (Figure 45). This would imply that the spectrometer can be used without having interfering effects, which means that no optical feedback is coming from the experimental beam path into alignment beam path.

The sensitivity of the created method for temporal change could be proven with experiments at a constant applied shear rate (3000 s^{-1}) while changing the set temperature and maintaining the scattering volume positioned at the edge of the sample (the plate-plate geometry). As expected, the viscosity measured with the rheometer as well as the longitudinal rigidity modulus M` of the elastic stiffness tensor (gathered by spectroscopic measurements and calculated with the measured density of the sample material) both decrease with increasing temperature (Figure 121). The longitudinal rigidity modulus is the susceptibility related to the purely longitudinal elongation, as the viscosity is a quasi-elastic quantity. The modulus measured with the Brillouin spectroscopy thus detects the effective “spring constants” that determine the propagation of the longitudinal thermally induced sound waves. Even if there is no direct causal relation between those two susceptibilities, the temperature dependency can be resolved by the presented method.

The sensitivity of the created set-up regarding an applied shear field could also been proven by experiments with increased shear rates while the longitudinal part of the elastic modulus c_{11} (or the longitudinal rigidity modulus M´ of the elastic stiffness tensor) was measured with Brillouin spectroscopy. It shows a distinct decrease in the modulus starting with shear rates of about 500 s^{1} up to 3000 s^{-1}. This shows that it is possible to picture on one hand, the shear thinning of the sample material and on the other hand, the structural change or texturing within. To obtain more distinct information about the texturing, a combination of this method with Shear-Induced Polarized Light Imaging (SIPLI) technique is recommended.

Finally the longitudinal rigidity modulus M` of the elastic stiffness tensor was measured at three different positions in the sample, namely the edge position, the relative middle and at the center, as a function of the shear rate. It was found that this new method is able, to even resolve the difference of modulus of rigidity for those positions. Nevertheless, as the behavior of the modulus is quite the same, it suggests that the sample, as soon as a critical shear rate has been reached, orient homogeneously. By combining this technique with other optical technologies, like SIPLI, a microscopic optical set-up for picturing live videos, and the combination with Raman spectroscopy [142], it could be studied better and in more detail. One would be able to find out if there are further explanations for the behavior, e.g. the rheometer plate causing an in or outflow of water that changes the hydration level of the gel, which would be the reason of the slight differences in the three measured curves we can see in Figure 126.

Based on the current work, measurements with different (rheometer) geometries (especially cone-plate geometry) and different light scattering geometries are expected to give more information about the complete elastic tensor with a spatial resolution of about 50 µm inside the gap of a rotational rheometer. This should shed more light on local causes of e.g. shear thinning, shear banding, hydration effects in the sample and interfacial effects. Further, the combination of different scattering geometries will give more insight of the orientation and structuring of the molecules inside the sample volume and even could measure the refractive index by using 90A scattering, simultaneously.

The approach of applying RIΘA scattering is presented in the Appendix, as it is beyond the scope of this work, but it shows that it is possible to measure samples in the rheometer with such a geometry. The use of fiber optics might be a better approach, though, as, due to the construction of the rheometer, it is hard to obtain good optical access with common mechano-optical set-ups (lenses and mirrors). The angles of incidence are kept quite small, which decreases the effectivity and sensitivity of the measurements. However, it is success that we were able to record spectra of the wave vector in the horizontal plane of the sample in 360° orientation inside the rheometer sample stage while shearing. The potential of this new approach could be shown and it is expected a new field of research in rheology.

Appendix

The research of Brillouin Rheology with the RIΘA scattering geometry (Figure 43) set-up is shown here for future projects and to visualize that this developed technology also has the potential to be a novel method in the research of texturing of complex fluids under shear. However, some optimization regarding the opto-mechanical set-up is supposed to be necessary, like the use of fiber optics to reach the scattering volume in a better way and to ease the application and combination of different scattering geometries. The material of choice in this experimental series was the liquid crystal 5CB. A created set-up to apply the RIΘA *scattering is introduced. Rheology with different gap sizes is shown and compared. Brillouin Rheology experiments with a rotation of the q-vector in the horizontal plane of the sample are shown and interpreted lightly, as there is much research to do to give full explanations of the effects, which were found.*

The Material 5CB

The liquid crystal 5CB (4-pentyl-4`cyanobiphenyl) is a well known material and finds use in a variety of applications as e.g. Liquid Crystal Displays (LCD). It is introduced and described in detail in following articles [143-165] and books [166-173] as for rheological and flow studies in [148, 149, 155, 161, 174-184]. The 5CB is investigated with the refractometer and an analysis of the refractive index is implemented over a temperature regime of 10°C to 70°C. This is the maximum temperature regime used in this work, which the set-up with the rheometer allows, due to construction boundaries. However, the measurements to acquire the refractive index of the 5CB over temperature is two-parted, namely, once, the temperature is increased and secondly, it is decreased. It appears that there is a difference in the transition temperature, pictured in Figure 127.

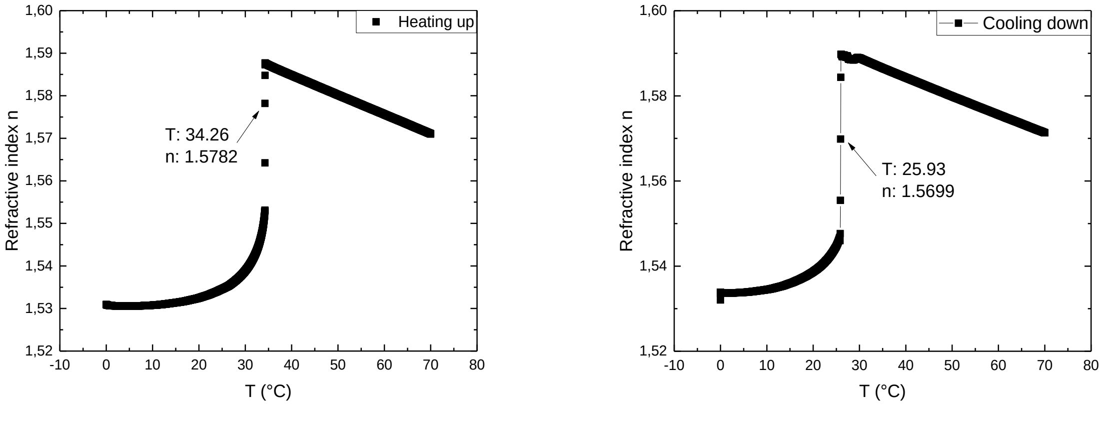

Figure 127: Refractive index of 5CB over temperature, left increasing temperature, right decreasing.

The 5CB sample that we use reacts to the increase of temperature so that it is increasing with the temperature gradually, then at about 34°C there is a sudden increase of n of about 0.05. For decreasing temperature, the refractive index n is increasing with decreasing temperature until about 26°C then it drops about 0.05 and decreasing slowly further.

The RI$\boldsymbol{\Theta A}$ scattering Set-up inside the rheometer

The application of the RIΘA scattering in the rheometer would give an interesting view of the sample material as one q-vector will give the backscattering signal and the second q-vector that is lying in the horizontal plane of the sample volume, could give information about the orientation or structuring of the molecules in that plane as well. (By giving information about the elastic components in those orientations). This means, horizontal and vertical plane of the sample volume could be observed at once. Albeit, the realization of this idea with opto-mechanics is a quite difficile contemplation. The principle set-up is sketched in the following illustration (Figure 128). The optical elements are marked with new descriptions to make the experimental set-up clearer.

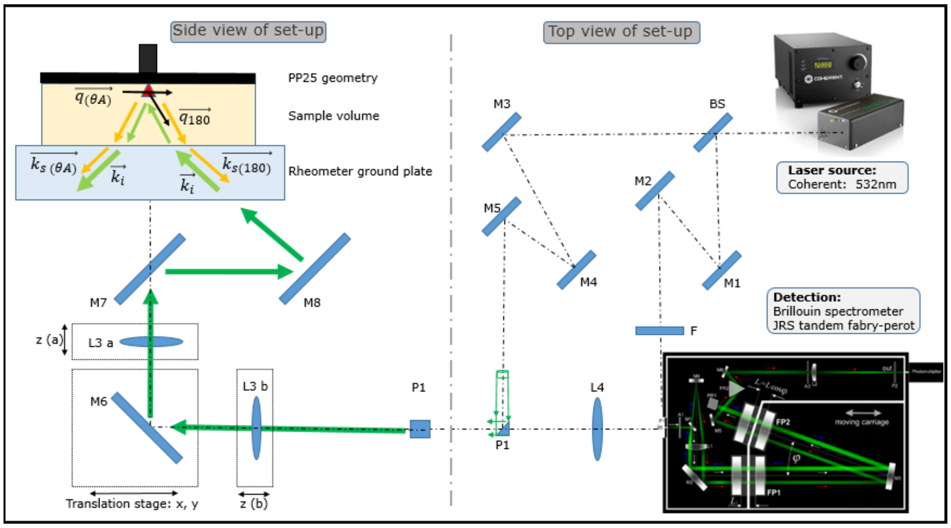

Figure 128: Illustration of realization of the optical beam path for $R\Theta TA$ scattering. Right part, the top view of the laser source and detection unit, the spectrometer, with corresponding optics for the reference and target path. The target path is shown, left, in side view. The laser beam is either focused by L3a or L3b due to the set-up at time, and lead up into the rheometer sample stage. The mirror M6 and M7 build a periscope while the mirror M8 is used to determine the angle of incidence and apply the $R\Theta TA$ scattering geometry. Latter, is visualized with corresponding wave vectors as introduced with the scattering geometries.

The development of the set-up was on the fly so slight changes occur over time to improve signal strength and repeatability. In the beginning, the lens L3a is used to focus and collect the light, while the tower is rotated around its vertical (z) axis. In progress of development, the lens is put in front of the periscope (indicated as L3b) and fixed with additional mounts to the tower for stabilization.

An opto-mechanical tower has to be developed, which can hold the periscope mirrors as well as the mirror M8 for setting the angle of the scattering volume. Further, it has to be able to translate in x-y plane underneath the rheometer and rotate around its own vertical axis, to be able, to get the information from the $\overrightarrow{q_{(\theta A)}}$ vector in horizontal plane and the backscattering vector $\overrightarrow{q_{180}}$, which is not that sensitive to detect. All the translation and rotational movements have to be achieved without tilting or changing the position of the scattering volume, as this is the most important and crucial point. Figure 129 gives a picture of first design drawings to create such an opto-mechanical tower with corresponding part numbers from Thorlabs and mechanical parts that would have to be built, additionally.

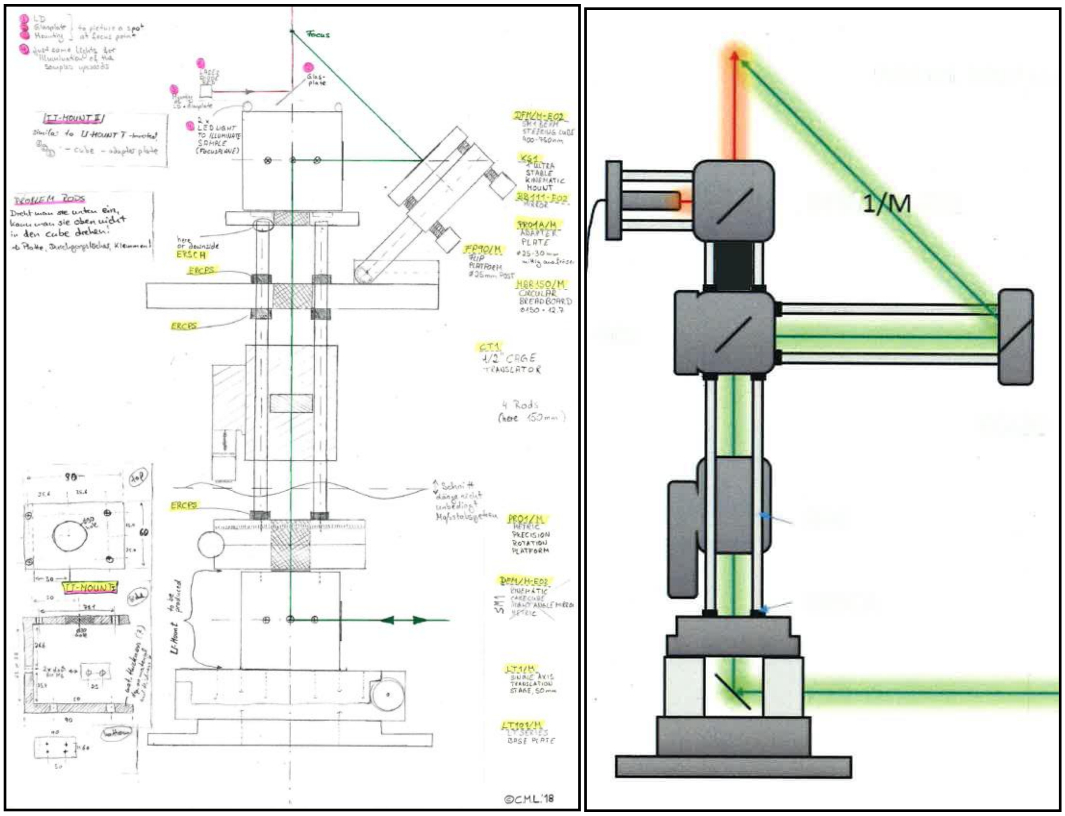

Figure 129: First concept; construction drawing and design of an opto-mechanical tower to apply a $R\Theta TA$ scattering geometry inside the rheometer sample stage, for illustration of complexity. This approach has a red laser diode using as target beam.

The main idea is to lead the laser beam from the optical axis of the table, upwards, in direction of the rheometer, with a mirror. The vertical axis then has an opto-mechanical translation stage for the objective lens. A second mirror, building a periscope, leads the light over a third mirror to the sample stage. To be able to steer and to fine adjust, most of the holders have to be able to translate and rotate the optics. An idea to send a laser spot (red in Figure 129) up to the image plane to identify and picture the area of interest, where the measurement is made, is an additional application, but is not used here in the latter.

Nevertheless, the construction is being changed while the research and development on the fly. The tower built and used in the end for the study of $R\Theta TA$ scattering, is pictured and described in the following Figure 130. Left, the opto-mechanical parts from Thorlabs are pictured, next to them, their order of freedoms of translation, rotation and tilting are indicated. The block diagram gives the order and the part numbers (from Thorlabs) of the parts used for construction and the beam path is sketched into it. At the right side, there are two pictures showing the tower in use as the beam paths are sketched into it for illustration as well. The pictured tower is in all three illustrations oriented in direction of the spectrometer, which is called *0° rotation of tower* in the following work, depiction and discussion of results.

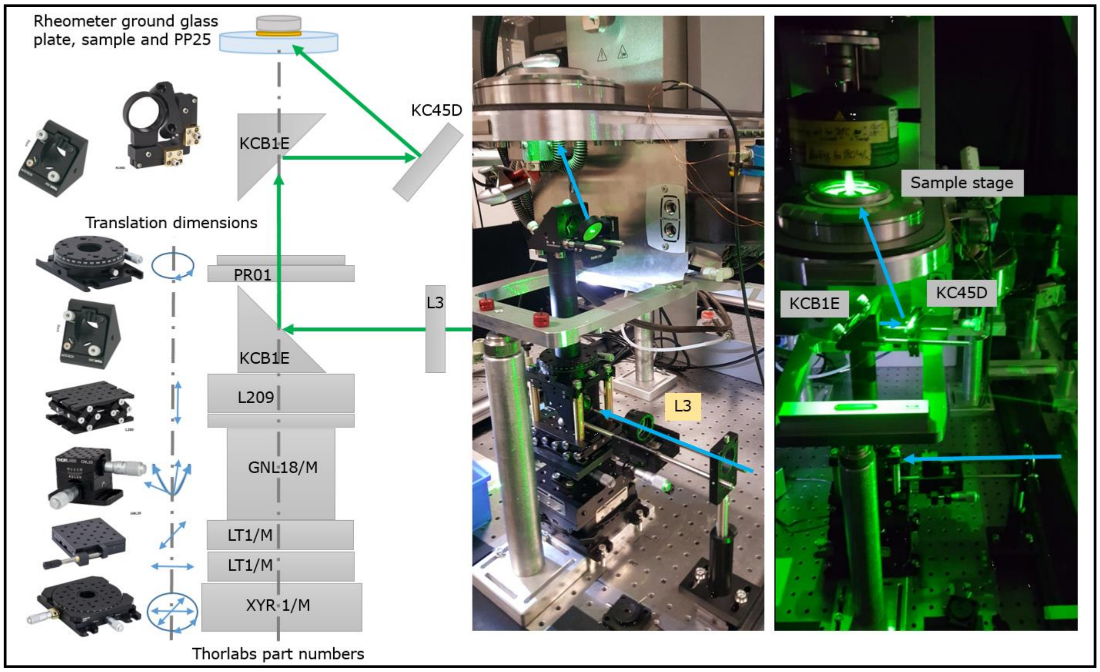

Figure 130: Illustration of the created tower for the application of Brillouin Rheology with RΘTA scattering. Left, the parts with corresponding part numbers from Thorlabs and a block diagram of the assembly of them, as well as the dimensions of freedom of the translation, rotation and tilt movements of the opto-mechanical parts. Middle and right are pictures to illustrate the beam path.

Starting from below, the XYR1/M rotation and x-y-translation module is used as the foundation as it can be used to set very small translations and keep it fixed with a clamp. The two LT1/M linear translation stages (50mm) are set 90° oriented to each other, to give a coarse translation in x-y-direction. The goniometer GNL18/M is set on top to be able to tilt angular misalignments. The vertical translation stage L209 is used to set the optical axis, which enters the mirror in KCB1E central position. The objective lens L3 is set into a translation stage CT1 for fine adjusting the focal position. The rotation module PR01 is used to do the rotation for the main experiment, namely, the rotation of the q-vector in the horizontal plane of the sample stage. The second KCB1E cube with internal mirror and the gimbal mount KC45D is rotating with the rotation module. The angle of incidence of the laser to the sample is set with the gimbal mount KC45D so the alignment is crucial at this point. The laser beam has to be set through the periscope, as such, that it will not deviate in any direction around the optical axis over rotation of the tower. This has to be set with the KCB1E modules and in worst case with the prism P1 (or the mirrors M3-M5), but due to proper alignment beforehand, this should not be necessary. A simple fix to do so is to set an aperture in front of the gimbal and check the spot while rotating PR01. The gimbal, which angular alignment can be set before mounted (e.g. with a small set-up to determine the certain angle of transmission as there is no scale on it) leads the laser beam to the sample stage. With proper alignment, the laser beam shall hit the center of the sample stage (which is also on the vertical axis of the periscope) and while rotating PR01 the spot is not deviating from this central position. The ring pattern, (Figure 52) introduced before, can now further be used for a fine opto-mechanical adjustment. If the focal spot is set to the center position of the ring pattern so that it stays there over rotation of the periscope and so that a sharp image is imaged on the U-eye window (CCD at the entrance aperture of the spectrometer) while rotating, it is proper adjusted to start first experiments.

The plot (Figure 131) shows the measurement of rotation of the q-vector for *distilled water* for calibrating the system. It looks quite promising as both peak values appear to be stable (or linear) over the rotation. The exception is that at four positions the values are nearly 0 GHz. A test is made at 45° rotational position over long time (about an hour), which gives results marked as blue triangles (as well for the signal heights) in the plot, confirming, that the values can be measured, one needs just much higher acquisition times. The average value of Brillouin frequency shifts for the q_{180} peaks is 7.317 GHz +- 0.053 GHz and for $q_{\Theta A}$ it is 1.602 GHz +- 0.0046GHz.

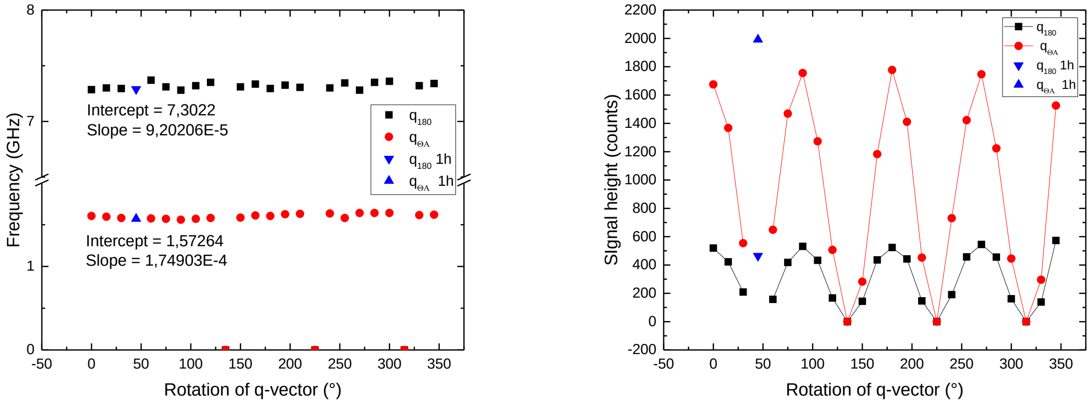

Figure 131: Brillouin frequency shifts for $q_{\Theta A}$ (inner) and q_{180} (outer) peaks average values over rotation of distilled water at 10°C with polished plate-plate geometry PP25. The acquisition time is 4 min per spectra. At 4 rotational positions the values are nearly 0. An additional measurement at 45° rotation of tower over nearly an hour gives a value that fits the curve (indicated by blue triangles).

The behavior of the signal height values that seem to correspond to polarization effects, which may influence the measurements, are investigated in the following.

Nevertheless, another experimental sequence is implemented with a newly adjusted tower and 10 min acquisition time for each spectra. All other parameters stay same. The tower was not rotated in order, meaning in 15° steps one after each other, -they were randomly applied to assure the stability of the tower and opto-mechanical construction (e.g. 15°, 225°, 45°, 345°,..).

The last opto-mechanical adjustments lead to a stable course for the $q_{\Theta A}$ peaks average frequency values over rotation as for the q_{180} peaks average values, they seem more variating now. The average value for the $q_{\Theta A}$ over the rotation is 1.625 GHz +- 0.008 GHz and for the q_{180} it is 7.386 GHz +- 0.045 GHz.

The sensitivity is now set to the $q_{\Theta A}$ peaks as they are quite smooth in average over rotation and it is expected to get some inside in structural behavior of materials under flow. The liquid crystal 5CB is chosen as the rod-like structure, which might orient under high shear rates quite well. This we then may can able picture with the Brillouin spectra.

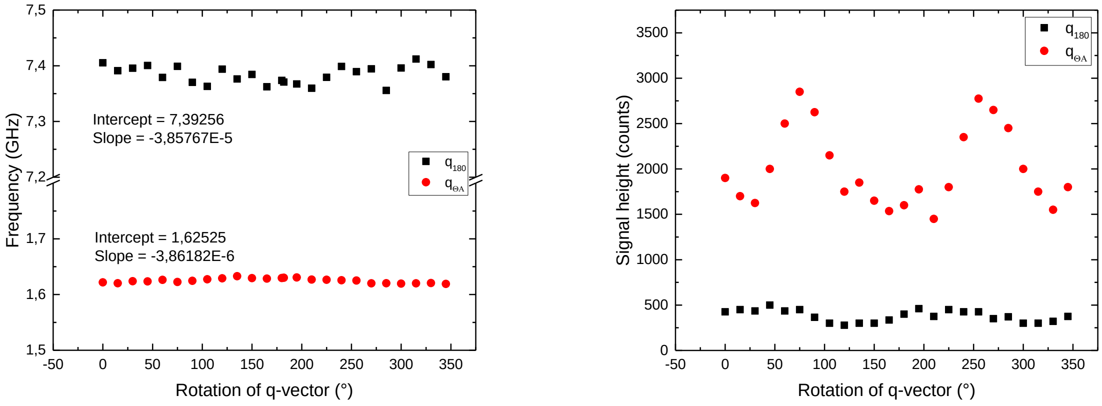

Figure 132: Left, Brillouin shift frequencies (the $q_{\Theta A}$ *(inner) and* q_{180} *(outer) peaks average values) over rotation of the tower for distilled water at 10°C, right, the corresponding signal heights over rotation.*

Influence of applied laser power to the measurements

The temperature is set to 37°C, a shear rate $\dot{\gamma}$ of 1100 s^{-1} is applied to the 5CB sample and spectra are collected for 10 min, then the laser power P is changed, so the experiment starts (Figure 133). For the sake of repeatability, the rheometer was shearing the sample for an hour before starting the measurements. The scattering volume is 2 mm from the edge of the sample, in the middle (z) plane.

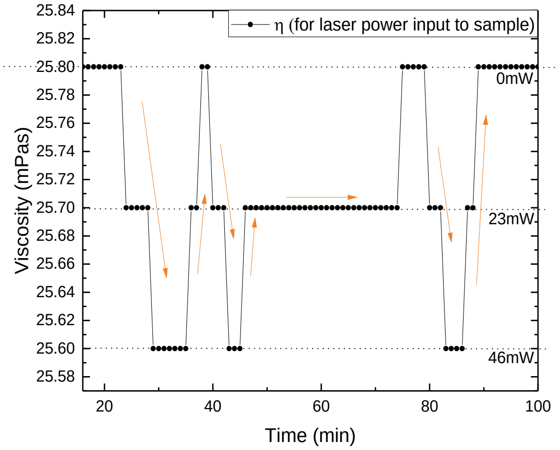

Figure 133: Viscosity η *change due to laser impact into the sample over time for an applied shear rate* $\dot{\gamma}$ *of 1100* s^{-1}*.*

Figure 133 implies that the laser has influence to the rheological measured viscosity η. After 20 min, the laser beam is steered into the sample with a power of 46 mW. The viscosity drops from 25.8 mPas to 25.6 mPas. Blocking the laser beam, the viscosity goes up to 25.8 mPas again, as back to 25.6 mPas after leading the beam back into the sample. The laser power is reduced to 23 mW. The viscosity goes up to 25.7 mPas and stays. Blocking the beam again, the viscosity increases, testing the 46 mW it decreases again and levels back to the starting viscosity value by blocking the beam. Those measurements allow to give an extrapolation of viscosity η over laser input power P (Figure 134) for an applied shear rate $\dot{\gamma}$ of 1100 s^{-1}.

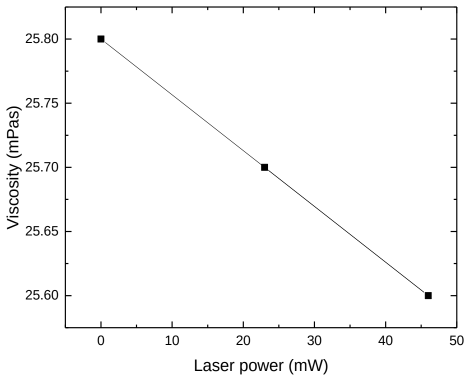

Figure 134: Extrapolation of viscosity η of 5CB to applied laser power P *to the sample.*

The behavior could be confirmed with further repeating measurements and are repeated for the two previously experimentally tested shear rates $\dot{\gamma}$ of 2200 s^{-1} and 3300 s^{-1} to investigate more detailed (Figure 135).

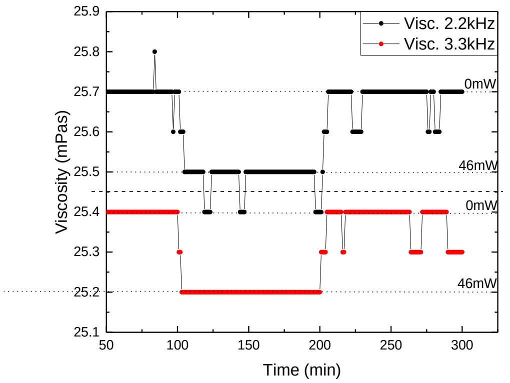

Figure 135: Viscosity η change due to laser impact over time for an applied shear rate $\dot{\gamma}$ of 2200 s^{-1} and 3300 s^{-1}.

The application of 46 mW into the sample and blocking it, has the same effect for the higher shear rates, namely, the decrease of viscosity of about 0.2 mPas. Nevertheless, again, we are at the resolution limit of the rheometer (0.1 mPas). On macroscopic size, this means, that it shall not influence the results in a regard, which concerns us. To trap molecules like a optical trap the powers are too small. Here we seem to have thermal effects, which minimally change the viscosity. However, in future studies, I recommend to research the trapping effect for such measurements more detailed with own experimental series.

Rheology of 5CB for different gaps sizes

<u>1 mm gap size:</u> The viscosity curves are recorded up to a shear rate $\dot{\gamma}$ of 1000 s^{-1} and measured back down. Each temperature measurement is an increasing and decreasing shear rate ramp. All temperatures are applied for 2 min before the measurements are started. The temperature is changed from 40°C down to 34°C and is plotted in colors in Figure 136. The measurement time of each point for the rheometer is set to 30 sec, giving a total measurement time for one temperature of 33 min.

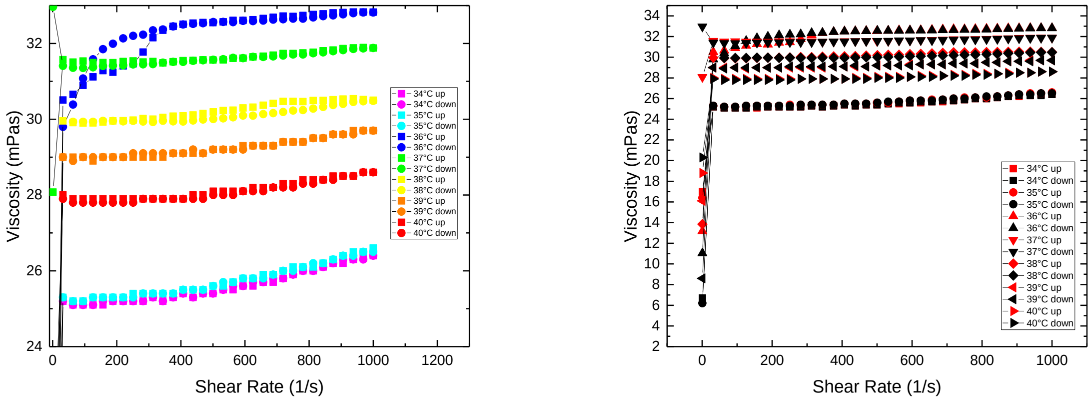

Figure 136: Viscosity curves of 5CB in a 1 mm gap for different temperatures recorded with the MCR302 rotational rheometer.

It´s recognizable that the viscosity values for 35°C (*25.3 mPas* to *26.5 mPas*) are above those of 34°C (*25.1 mPas* to *26.2 mPas*), then, with 36°C, there is a great jump to a higher viscosity values (*29.7 mPas* to *32.8 mPas*). The following temperatures show an inverted behavior as now the higher temperatures lead to lower viscosity values. Plotting the average viscosity values over temperature gives Figure 137.

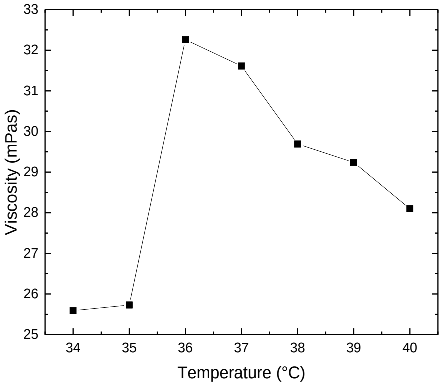

Figure 137: Average values for viscosity over temperature measured with the MCR302 rotational rheometer having the sample in a 1 mm gap.

The plot indicates a certain rise of viscosity at temperatures btw. 35°C and 36°C as it is decreasing again. A second measurement series starting with high temperature of 50°C, then 45°C to 30°C is implemented. The full series is shown in Figure 138 as the colored and zoomed version besides.

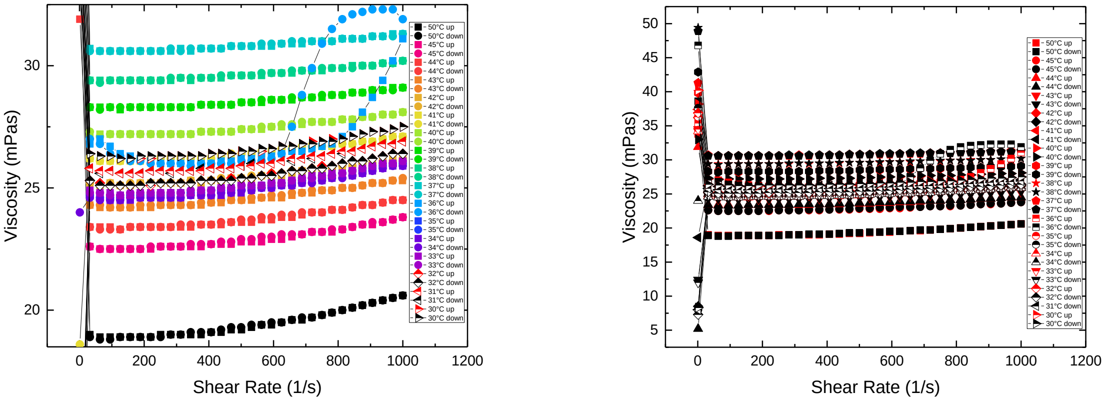

Figure 138: Viscosity curves in a 1 mm gap for 5CB and a temperature regime of 45°C to 30°C.

It gets visible that the PP25 is not appropriate for lower than 20 s^{-1} shear rate measurements (in those experiments). However, the viscosity values for 36°C show peculiar behavior. Showing the plots just from temperature of 45°C to 36°C for more clearance gives Figure 139.

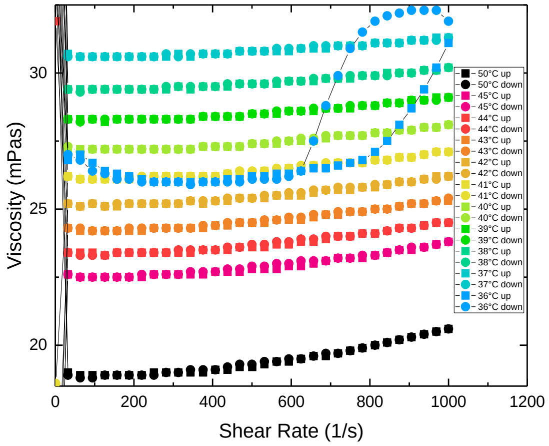

Figure 139: Viscosity curves of 5CB in 1 mm gap, 50°C, 45°C to 30°C.

The viscosity values from 50°C down to 37°C are increasing with temperature, as the viscosity for 50°C over the shear rate regime is from 18.9 mPas to 20.6 mPas, as for the 37°C temperature it increases over the shear rate from 30.6 mPas to 31.3mPas. The viscosity values for 36°C are seated (between 26 mPas and 31.1 mPas) were the 41°C values are (between 26 mPas and 27 mPas) as well. The hysteresis at 36°C appears to show an increasing structural strength when shearing. This topic will be studied further and the latter discussed. Decreasing from this temperature of 36°C down to 30°C the viscosity values again are increasing (Figure 140). However, there is first a drop of the viscosity values for 36°C (26 mPas to 31.1 mPas) to 35°C (24.5 mPas to 25.9 mPas) then it increases to 30°C (26.4 mPas to 27.5 mPas).

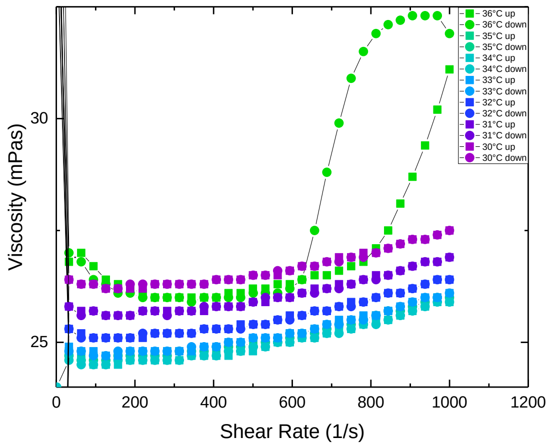

Figure 140: Viscosity curves in a 1mm gap for 5CB and a temperature regime of 36°C to 30°C.

To visualize the behavior of this measurement series better, it is shown in Figure 141, just giving the three temperatures of 37°C, 36°C and 35°C.

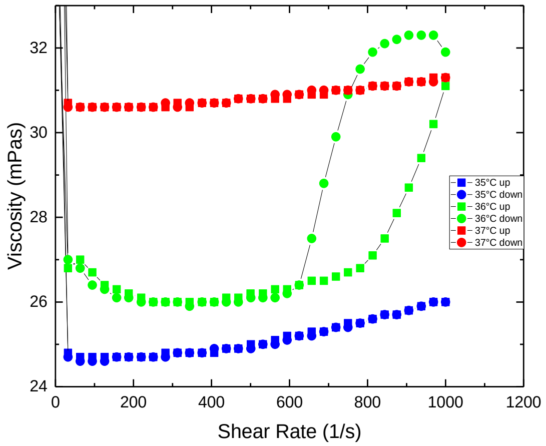

Figure 141: Viscosity curves in a 1 mm gap for 5CB and a temperature regime of 37°C, 36°C and 35°C.

The increase in shear rate $\dot{\gamma}$ at 36°C leads to a sharp increase of viscosity at about 800 s^{-1} to 1000 s^{-1}. Decreasing the shear rate $\dot{\gamma}$ again (green dots) the viscosity values stay up higher till about 750 s^{-1} then decrease till 600 s^{-1} to be on the same row again. This second plot of viscosity over temperature shows the same behavior than bevor just more distinct.

Plotting the average values of those experimental series show again a decrease in viscosity from 30°C to 35°C as it suddenly increases and with 36°C it starts to continuously decrease again

(Figure 142). The plot indicates a certain rise of viscosity at temperatures btw. 35°C and 36°C as it is decreasing again.

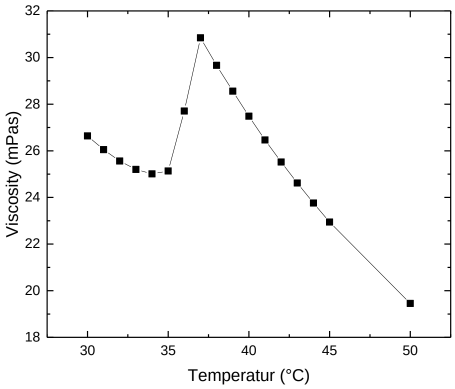

Figure 142: Average values for viscosity over temperature measured with the MCR 302 rotational rheometer having the sample in a 1 mm gap from a temperature of 30°C up to 50°C.

To study higher shear rates the experiment is set to a maximum shear rate $\dot{\gamma}$ of 2000 s^{-1} it gives following plot (Figure 143).

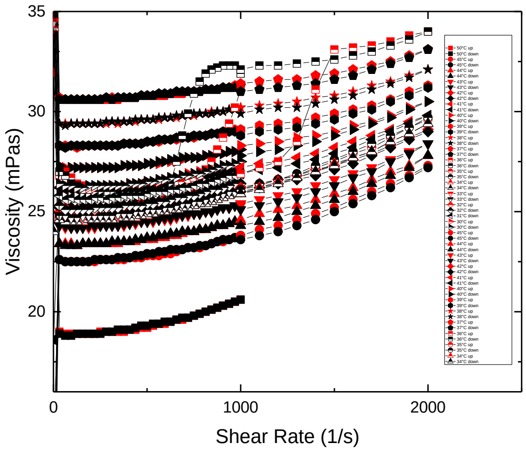

Figure 143: Viscosity curves in a 1 mm gap for 5CB and a temperature regime of 50°C, 45°C to 30°C up to a $\dot{\gamma}$ of 2000 s^{-1}.

The behavior of the flow curves is complementary to previous measurements as they are all increasing and showing a shear thickening behavior. Finding the relative shear rate maxima to apply, regarding different gap sizes, following measurement of viscosity over shear rate with a 1 mm gap is implemented at 38°C and plotted in Figure 144.

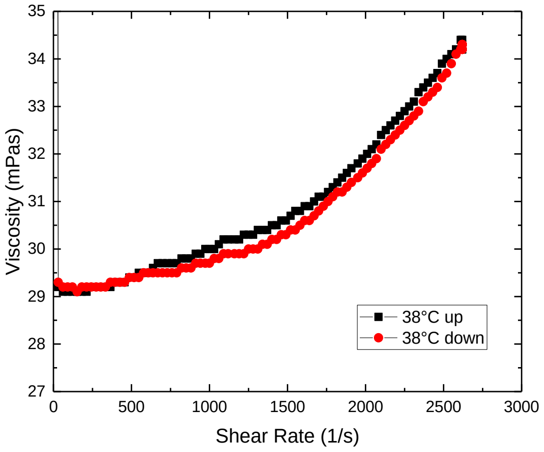

Figure 144: curve of 5CB in a 1 mm gap at 38°C for increasing (up) and decreasing (down) shear rate.

The rheometer is programmed to go up to 10000 s^{-1} shear rate $\dot{\gamma}$ and it stops at 2620 s^{-1}, then it goes down with the shear, so the maximum is found. A shear thickening behavior is recognizable as the values for the viscosity increase from 0 to maximum shear from 29.1 mPas to 34.3 mPas.

<u>0.5 mm gap size:</u> To get a comparison of rheological data of the 5CB, the rheometer is set to a 0.5 mm gap and the experiment is repeated (Figure 145).

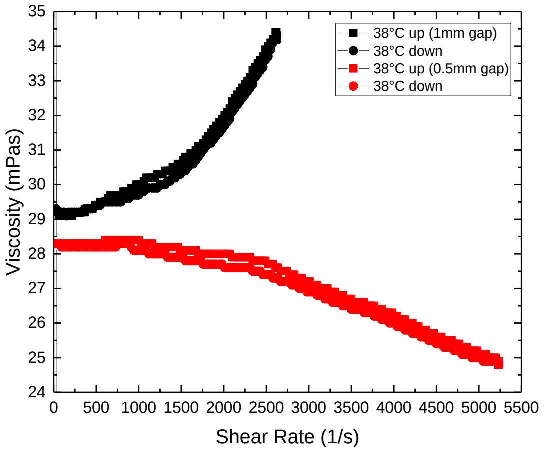

Figure 145: Comparison of viscosity curves for 5CB with a 1 mm (black) and 0.5 mm (red) gap size for increasing (up) and decreasing (down) shear rate at 38°C.

A distinct difference is getting visible having the same temperature, just a smaller gap size, namely, the viscosity values for a smaller gap are decreasing from 0 to 5000 s^{-1} shear from 28.3mPas to 24.8 mPas, while with a gap size of 1 mm the values increase over shear. So on one hand there is a shear thickening for a 1 mm gap and a shear thinning effect for a 0.5 mm gap, even all other parameters stay same. This leads to a further investigation of the 0.5 mm gap.

The viscosity curves are recorded with the same parameters as before just the smaller gap size of 0.5 mm is applied. The shear rate $\dot{\gamma}$ is set to its maximum of 5000 s^{-1} and the temperature regime of 42°C to 36°C is studied and shown in Figure 146.

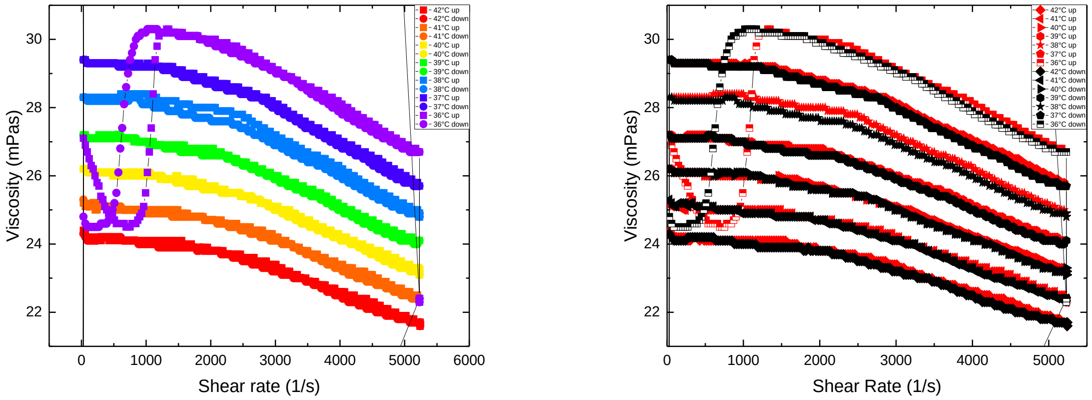

Figure 146: Viscosity curves for 5CB with a 0.5 mm gap in the temperature regime of 42°C to 36°C.

It is recognizable that the values for viscosity are increasing with decreasing temperature (42°C gives viscosity over shear of 24.3 mPas to 21.7 mPas as at 36°C from 30.1 mPas to 26.7 mPas). Further, shear thinning behavior is visible. At a temperature of 36°C, again, there is a peculiar behavior of the viscosity in the shear range before 1200 s^{-1} as it drops and rises again. The temperature regime experiment is repeated and further studied from 42°C to 30°C as plotted in Figure 147.

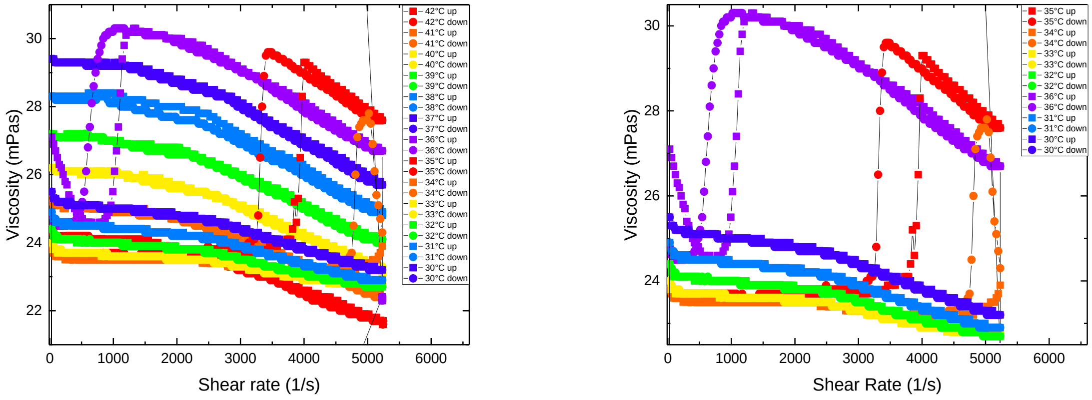

Figure 147: Viscosity curves of 5CB in a 0.5 mm gap, temperature regime of 42°C to 30°C left, right 35°C to 30°C.

Again, peculiar behavior of the viscosity values at 36°C happens, now compared to the 1 mm gap, there are three such series that show this behavior. The viscosity values are decreasing with temperature increase until 34°C. At high shear rate $\dot{\gamma}$ of about 5000 s^{-1} the viscosity curve has a steep increase. Showing it more clearly in Figure 148.

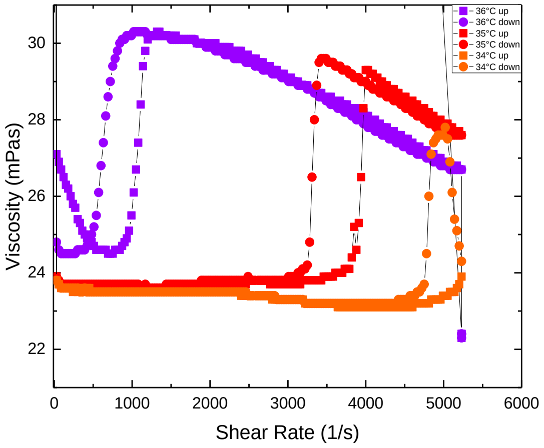

Figure 148: Viscosity curves of 5CB in a 0.5 mm gap in the temperature regime of 36°C to 34°C.

The average viscosity over temperature for the 0.5 mm gap size is plotted in Figure 149 and shows the same behavior as the experiment with the 1 mm gap, namely, a transition at 36°C. The viscosity increases fast and decreases further again.

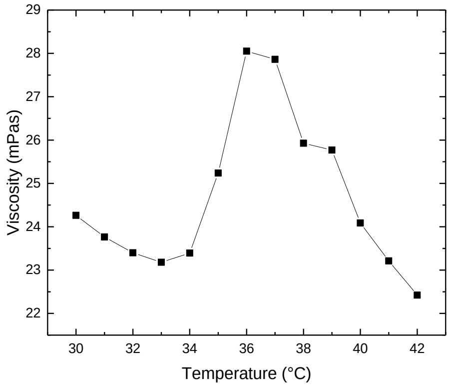

Figure 149: Average values for viscosity over temperature for 5CB and a 0.5 mm gap.

To get a better picture the comparison of the gap size of the rheometer is set further smaller to 0.25 mm and the experiments are repeated.

0.25 mm gap size: A last comparison regarding the investigation of 5CB rheology is implemented with the gap size set to 0.25 mm. The shear rate $\dot{\gamma}$ is set to a maximum of 5000 s^{-1} and the temperature regime is from 45°C to 37°C. Figure 150 shows the measurement sequence.

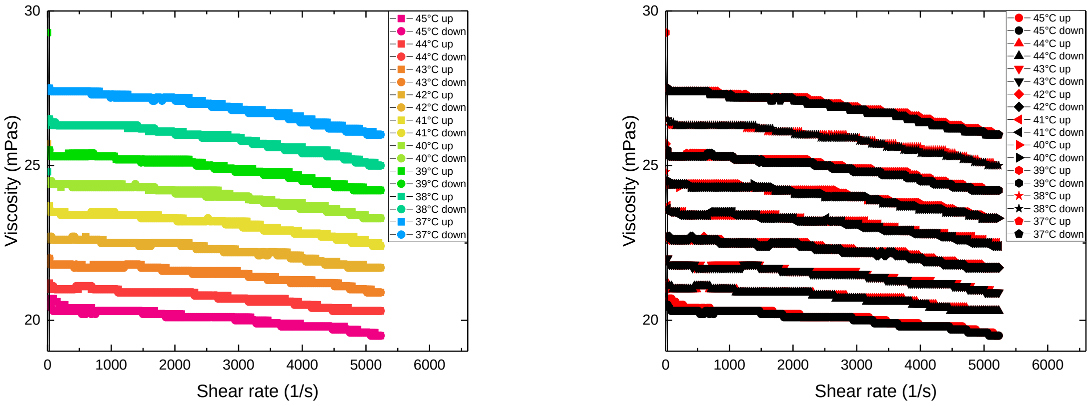

Figure 150: Viscosity curves for 5CB in a 0.25 mm gap and a temperature regime of 45°C to 37°C.

The viscosity is increasing with decreasing temperatures from 45°C (20.5 mPas) until 37°C (19.5 mPas) also for the 0.25 mm gap. Still, there is a shear thinning behavior, but not as clearly as with the 0.5 mm gap size. Introducing the measurement series of 36°C the peculiar behavior shows up again, but this time the viscosity will stay higher at shear rates $\dot{\gamma}$ over 2000 s^{-1}, not as before, drops down (indicated in Figure 151).

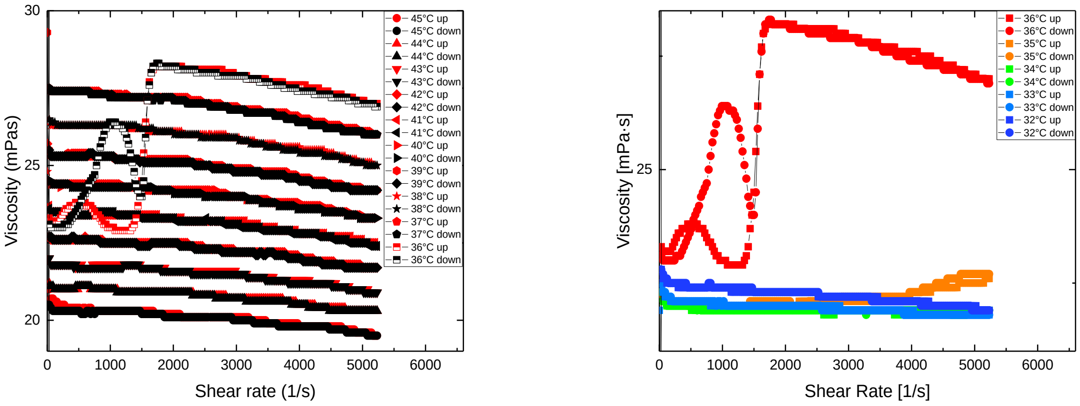

Figure 151: Left; viscosity curves for 5CB in a 0.25 mm gap and temperature regime of 45°C to 36°C, right colored 36°C to 32°C.

Showing the in-/decrease of the shear rates $\dot{\gamma}$ in single plots, left up, right downwards shear rate ramps in the following (Figure 152) for comparison.

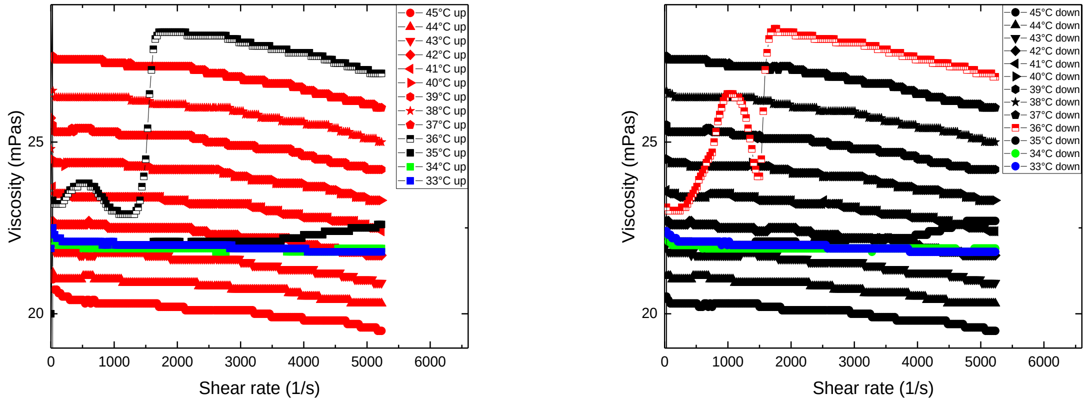

Figure 152 : Left; viscosity curves for 5CB for increasing shear rate in a 0.25 mm gap and temperature regime of 45°C to 36°C, right, decreasing.

The behavior of the viscosity values for 33°C, 34°C and 35°C seem to stick out, so are going to looked at, in more detail, in Figure 153.

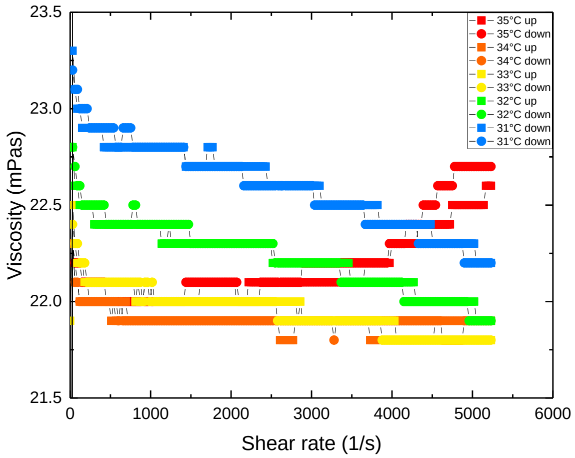

Figure 153: Viscosity curves of 5CB in a 0.25 mm gap for the temperatures 33°C, 34°C and 35°C. The resolution limit of the rheometer is reached so the curves cannot be pictured smoothened.

It shows, that the viscosity values decrease from 31°C (23.2 mPas over shear rate down to 22.2 mPas) to a temperature of 34°C (22.3 mPas to 21.8 mPas). The latter one is showing more stable viscosity values over shear and with the 35°C, the shear thinning behavior swaps to a shear thickening behavior (from 22 mPas to 22.7 mPas).

The viscosity plotted over temperatures for a 0.25 mm gap size follows in Figure 154.

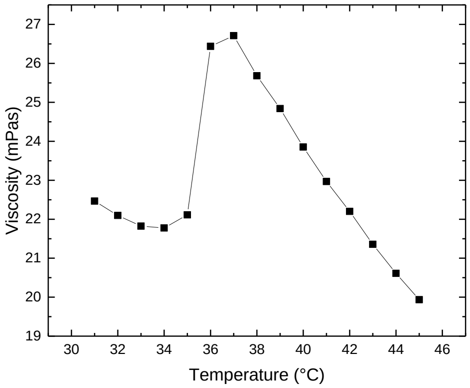

Figure 154: Average values for viscosity over temperature for 5CB in a 0.25 mm gap.

To research the temperature regime further at a gap size of 0.25 mm, temperatures of 80°C to 40°C are implemented and shown in following graphs (Figure 155).

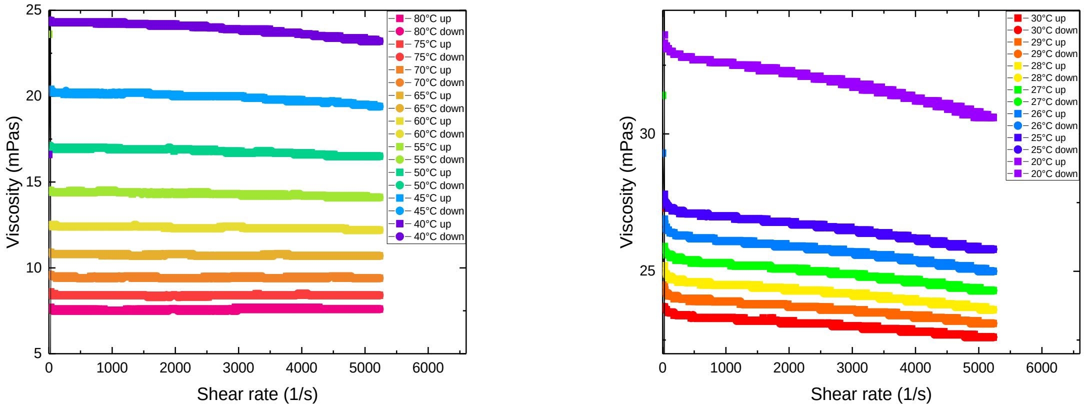

Figure 155: Viscosity curves of 5CB in a 0.25 mm gap for a temperature regime 80°C to 40°C, left; right 30°C to 20°C.

The viscosity values increase for decreasing temperatures (80°C the viscosity is 7.6 mPas to 7.5 mPas over the shear rate $\dot{\gamma}$ regime and at 50°C it is between 17.1 mPas and 16.5 mPas). Starting with 45°C (20.3 mPas to 19.4 mPas) and 40°C (24.4 mPas to 23.2 mPas) shear thinning at high shear rates starts getting visible.

However, more viscosity curves are shown for temperatures of 30°C (23.7 mPas to 22.6 mPas) to 20°C (33.6 mPas to 30.6 mPas). The behavior stays the same for the viscosity values under 30°C.

The shear thinning behavior increases with decreasing temperature.

The plot of the average values for viscosity over temperature are plotted in Figure 156 (left and the combination with previous measurements right).

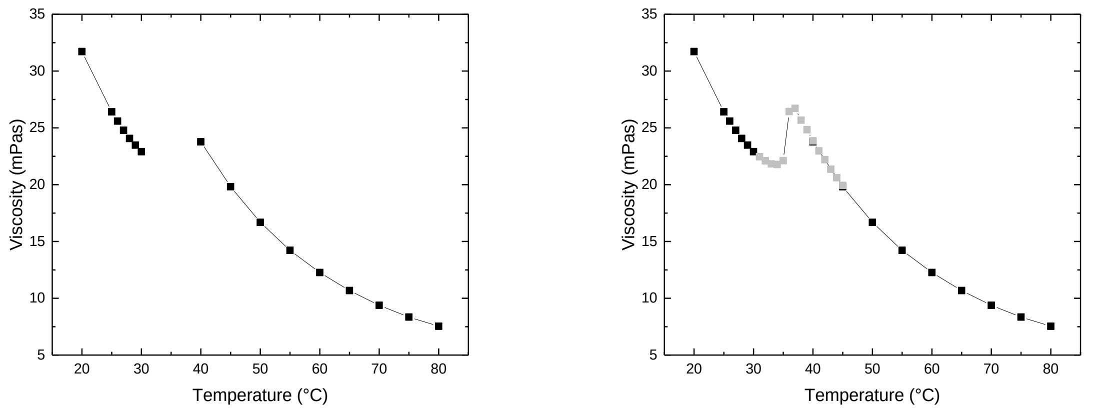

Figure 156: Average values for viscosity over temperature of 5CB in a 0.25 mm gap, left; right the combination with previous gathered measurement values.

The plots imply, as before, that there is a transition point at 36°C as the viscosity decreases before, increases at 35°C and decreases with higher temperatures of 36°C again.

To fill the gap of applicable temperatures further and to be able to apply a zero shear fit, the temperatures of 15°C down to 0°C are executed, flow curves collected and plotted in the following Figure 157.

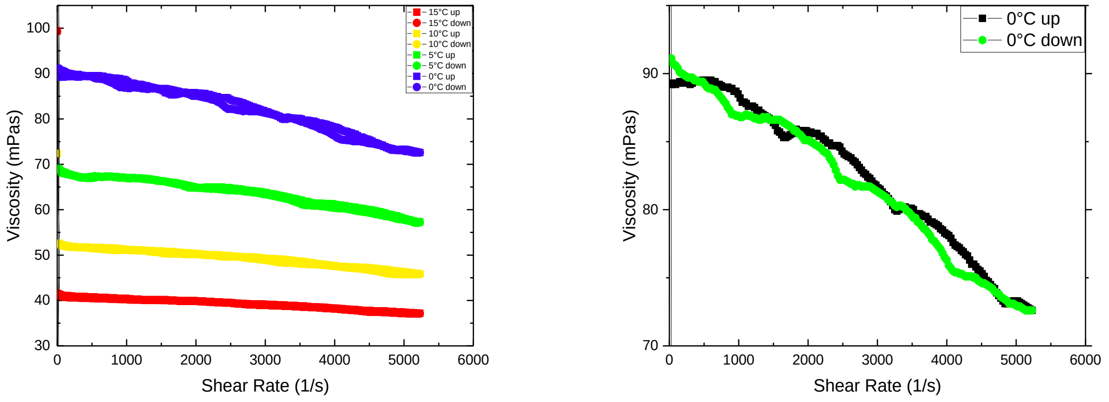

Figure 157: Flow curves of 5CB in a 0.25 mm gap for a temperature regime of 15°C down to 0°C, right for 0°C shear rate going up and down.

Like before, the values of viscosity for this temperature regime is increasing with decreasing temperature. At 15°C the viscosity is between 41.1 mPas, for the 0°C experiment it follows to be between 91.1 mPas to 72.6 mPas. The shear thinning behavior is visible and strongest as depicted in Figure 157 at 0°C. Nevertheless, effects like slip (at interfaces) could be a reason for this strong behavior and will be commented in the discussion section the latter in more detail.

Putting all data together, the viscosity curve over temperature (Figure 158) looks now as follows (left and middle), the zero shear fit (right).

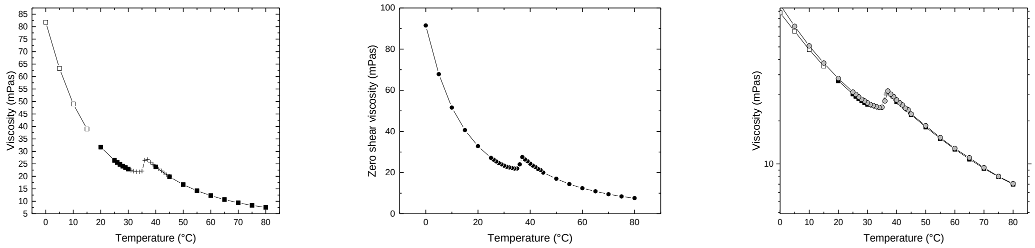

Figure 158: Average values for viscosity over temperature of three experimental series combined (left and middle) and a zero viscosity fit (right) for 0.25 mm gap.

The rheology of 5CB is executed to find interesting shear rate regimes and temperatures to implement experiments with the Brillouin Rheology approach, applying the $R\Theta TA$ scattering geometry.

As a result, in the following experiments, high shear rates are applied as the shear thinning behavior is visible at those. Further temperatures around the transition temperature 36°C, 37°C are investigated.

Picturing the viscosity curves of the measurement sequences (Figure 136 to Figure 157) only at the temperature of 36°C in comparison of the three different gap sizes (1 mm, 0.5 mm and 0.25 mm) in following Figure 159 over the whole shear rate regime (left) and just the area of interest (until a $\dot{\gamma}$ of 2000 s^{-1}, right).

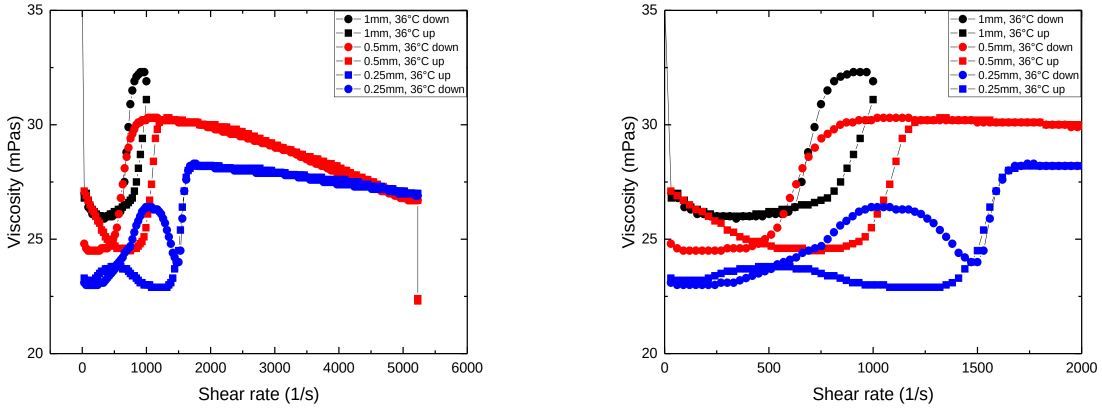

Figure 159: Viscosity over shear rate for 5CB at 36°C for three different gap sizes (1 mm, 0.5 mm and 0.25 mm).

The behavior shows in all three cases an increasing structural strength with shearing.

Plotting the average values of viscosity over the temperature for the three different gap sizes giving Figure 160. At a temperature of 37°C the highest viscosity values are reached in all three gap sizes as marked in the figure.

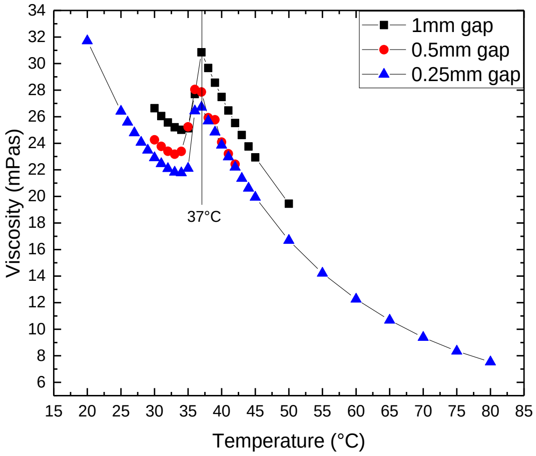

Figure 160: Comparison of viscosity over temperature of 5CB for the three different gap sizes.

Even the absolute values of the viscosity curves for 5CB are slightly different due to the different gap size, the transition temperature between 35°C and 37°C are the same. The divergence from references and tests shown in the material section seem to occur due to the different set-ups and amounts of sample (for the sample volume).

360° rotational Brillouin Rheology of 5CB

The rotation of the q-vector in horizontal plane of the 5CB sample for different shear rates at 36°C are plotted in polar plots (Figure 161 and Figure 162) for a qualitative discussion.

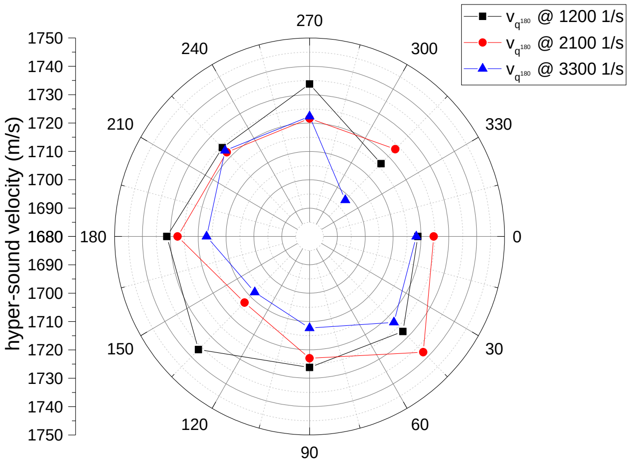

Figure 161: Polar plot of hyper-sound velocity of the quasi-longitudinal phonons over rotation of the q-vector in horizontal plane for 5CB at 36°C and three different shear rates.

One can see that there is some kind of symmetry in the quasi-longitudinal as quasi-transversal curves for the different shear rates.

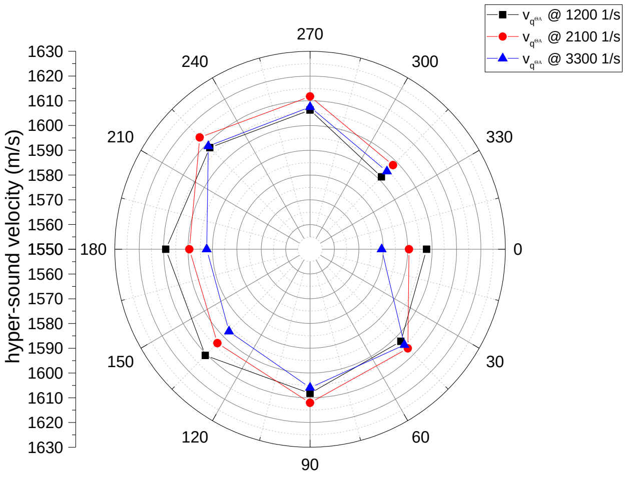

Figure 162: Polar plot of hyper-sound velocity of the quasi-transversal phonons over rotation of the q-vector in horizontal plane for 5CB at 36°C and three different shear rates.

The higher shear rates seem to have more impact as they seem to be more in the middle of the plots. The lower high shear rates at the outer radial positions having the higher relative velocities seem to show more effects.

Figure 163 is a sketch to give a better understanding of the acquired experimental data. In the middle, the rheological ground plate is picture (blue) from top view. The sample volume is marked yellow and rod like particles are drawn as they could be arranged while shearing. The different colors shall show the different radial positions (red outer diameter, green in the middle and blue central).

The shear field inside the sample is not homogeneously distributed, the real spinning velocity of the plate-plate geometry is higher at the outer diameter (indicated red) than in the central position (marked blue). The green dot indicates the position of the Brillouin spectroscopy measurements at the radial edge position. The polar plot besides now pictures the measurement what can also be seen as top view. The sketch at the top left of the figure shows the side view of the rheological geometry, the sample volume and the glass ground plate. The scattering vectors are indicated as well as the direction of the x-axis. This helps now to picture the situation more clearly. The q-vector for the backscattering is "looking" in downward direction, where the beam is coming from. The vector of the RIΘA scattering is oriented in the horizontal plane and in the direction where the beam is coming from. So having an angle of 0° rotation in the polar plot the q-vector of the RΘTA scattering is oriented in that direction (marked as positive x-direction).

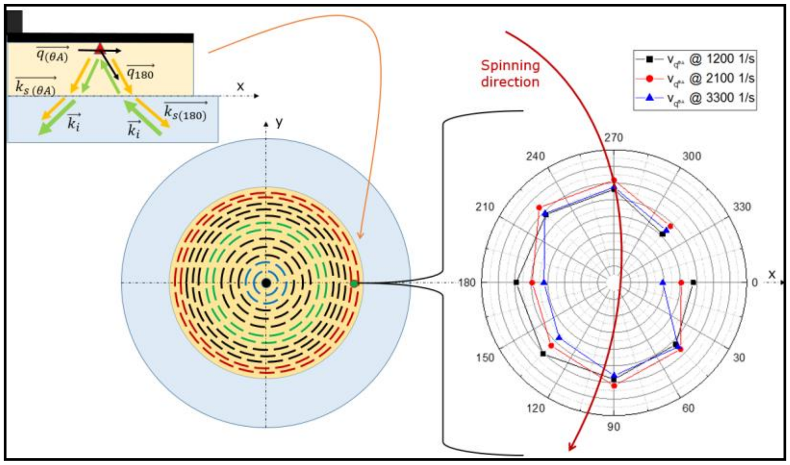

Figure 163: Illustration of the sample volume (yellow) in top view and side view (middle and top left) as well as the scattering volume (green dot). The polar plot is placed besides to give a better understanding of the evaluation. The direction of spin of the rheological geometry is indicated with the red arrow. The orientation of the q-vector for the backscattering signal is in downward direction as the R$\Theta T A$ scattering vector is oriented to the outer diameter for 0° rotation of the tower.

Now there is a symmetry visible which seem to indicate that orienting to the outer radial position (0° rotation of the tower) the hyper-sound velocity decreases while being oriented to the inner side (180° rotation of the tower) it increases again. To investigate this behavior, smaller rotational steps are implemented and shown in a polar-plot style in Figure 164 and Figure 165 for the 5CB at 37°C for a shear rate of 1100 s^{-1} and a maximum rate of 3300 s^{-1} in 15° steps of rotation of the q-vector in horizontal plane. The acquisition time is set to 5 min as the laser to 46 mW power after the prism and the gap size is still 0.25 mm.

Figure 164 shows the quasi-longitudinal phonons that are not very expressive over rotation, yet, only the values are as usual, quite evenly distributed over the rotation.

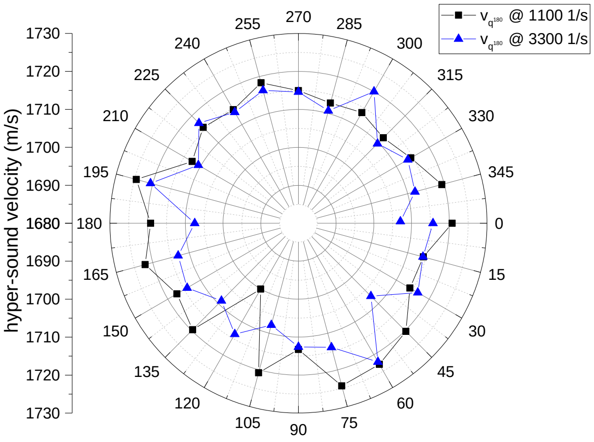

Figure 164: Polar plot of hyper-sound velocity of the quasi-longitudinal phonons over rotation of the q-vector in horizontal plane for 5CB at 37°C and two different shear rates.

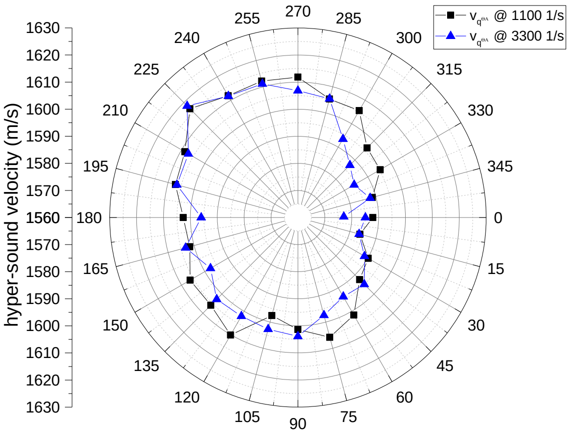

Figure 165: Polar plot of hyper-sound velocity of the quasi-transversal phonons over rotation of the q-vector in horizontal plane for 5CB at 37°C and two different shear rates.

Figure 165 might give more information. As the flow of the sample and the liquid crystals inside should go in principle from 270° rotational position to about 90° that is maybe what one can see here. The applied shear rate in the sample stage and the resulting revolutions of the plate-plate geometry is clockwise. As the scattering volume is placed at the boarder to the edge (for comparison lets say at 3 pm for a common watch) the orientation of the material and particles inside would be in this direction as well as one would think (indicated in Figure 163). Therefore, the difference in symmetry one can see might be the orientation of the liquid crystals in direction of flow with the RIΘA scattering.

A last measurement sequence with 5° steps of rotation of the q-vector is implemented and shown in the following polar plots (Figure 166 and Figure 167).

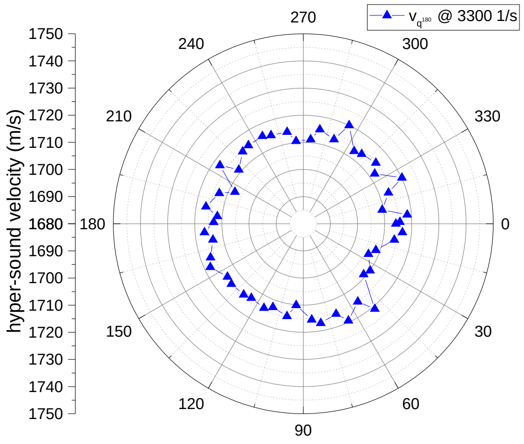

Figure 166: Polar plot of hyper-sound velocity of the quasi-longitudinal phonons over rotation of the q-vector in horizontal plane for 5CB at 3300 s^{-1} *shear rate at 37°C in 5° rotational steps.*

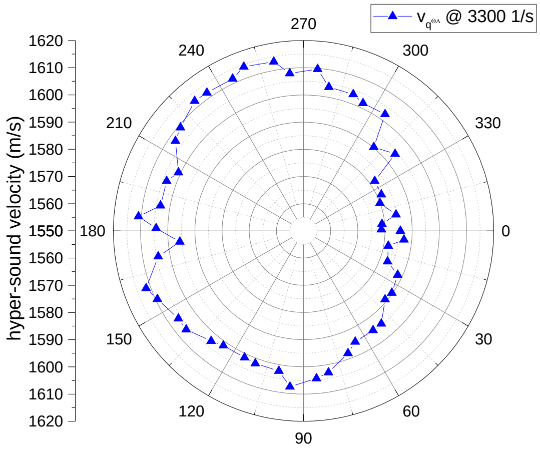

Figure 167: Polar plot of hyper-sound velocity of the quasi-transversal phonons over rotation of the q-vector in horizontal plane for 5CB at 3300 s^{-1} *shear rate at 37°C for 5° rotational steps.*

The finer resolution of the measurement steps indorse the idea that the internal orientation or a texturing of the 5CB under flow is depictable with this new Brillouin Rheology technology. Anyhow there has to be done a lot of further investigations and improvements as automatization of the set-up. Due to the set-up of the rheometer, the optical path could have been cut of partly, what would mean, that the result shown here is a wrong interpretation and comes from the cutting of and bending of the scattered light, which is detected. To minimize this effect the angle for the RIΘA scattering was made small in the last experiments shown here. Nevertheless, it is not clear, what is the real reason for the previously shown effects, so they are attached in the appendix and the interpretation is let open for further discussion and research.

References

1. Krüger, J. K. et al., *About The Nature Of The Structural Glass Transition: An Experimental Approach*. Lecture Notes in Physics, (2007), **716**, 61-159.
2. Mouis, M., et al., *Thermal Energy Harvesting*. Beyond-CMOS Nanodevices, (2014), **1:** p. 135-219.
3. Marqusee, J.A. and J.M. Deutch, *Brillouin light scattering from polymer gels.* The Journal of Chemical Physics, (1981), **75**(11): p. 5239-5245.
4. Rouxel, D., et al., *Brillouin spectroscopy of polymer nanocomposites.* Spectroscopy of Nanocomposites, (2016), Chapter **12**: p. 362-392.
5. Lindsay, S.M., M.W. Anderson, and J.R. Sandercock, *Construction and alignment of a high performance multipass vernier tandem Fabry–Perot interferometer.* Review of Scientific Instruments, (1981), **52**(10): p. 1478-1486.
6. Kane, K.I.W., et al., *Determination of the rheological properties of Matrigel for optimum seeding conditions in microfluidic cell cultures.* AIP Advances, (2018), **8**(12): p. 125332.
7. Fuller, G.G., *Optical rheometry of complex fluids*. Oxford Press, (1995).
8. Smoluchowski, M., *Molekular- kinetische Theorie der Opaleszenz von Gasen im kritischen Zustande, sowie einiger verwandter Erscheinungen.* Annalen der Physik, (1908), **25,** 205.
9. Einstein, A., *Theorie der Opaleszenz von homogenen Flüssigkeiten und Flüssigkeitsgemischen in der Nähe des kritischen Zustandes.* Ann. Phys., (1910), **33**: p. 1275-1298.
10. Brillouin, L., *Diffusion de la lumière et des rayons X par un corps transparent homogène.* Ann. Phys., (1922), vol. **9**, N°17, pp. 88–122.
11. Mandel’shtam, L.I., Zh. Russ. Fir. Khim. Ova., (1926), **58**, 381.
12. Gross, E., *Über Änderung der Wellenlänge bei Lichtzerstreuung in Kristallen*. Z. Phys., (1930), **63**, 685.
13. Gross, E., *Change of wave-length of light due to elastic heat waves at scattering in liquids.* Nature Materials, (1930), vol. **126**, 201, 400, 603.
14. Leontovich, M.A., *Towards a kinetics of fluctuations.* Z. Phys., (1931), **72**, 247.
15. Leontovich, M.A., *Some problems of sound absorption in polyatomic gases.* Izv. Akad. Nauk SSSR, (1936), Volume **5**, p. 633-643.
16. Fabelinskii, I.L., *Some questions of molecular light scattering in liquids.* Usp. Fir. Nauk, (1957), **63**, 355.
17. Pesin, M.S., and Fabelinskii, I. L., Sov. Phys. Dokl, (1959), **3**, 974.
18. Molchanov, V.A., and Fabelinskii, I. L., Dokl. Akad. Nauk SSSR, (1955), **105**, 248.
19. Peticolas, W.L., Stegeman, G. 1. A., and Stoicheff, B. P., *Intensity Ratio of Rayleigh to Brillouin Scattering at the Glass Transition in Polyethyl Methacrylate.* Phys. Rev. Lett., (1967), **18**, 1130.
20. Latha, G.D.P.A.J.P., *Brillouin scattering from polymers.* Journal of Polymer Science: Macromolecular Reviews, (1980), **15,** 1-27.
21. Baller, J., et al., *Elastic properties of single-crystalline and consolidated nano-structured yttrium oxide at room temperature.* Journal of Physics-Condensed Matter, (2000), **12**(25): p. 5403-5409.
22. Deshpande, A., J.M. Krishnan, and P.B. KUMAR, *Rheology of complex fluids*. (2010), New York: Springer.

23. Janeschitz-Kriegl, H., *Polymer Melt Rheology and Flow Birefringence*. Polymers - Properties and Applications, ed. J. Meissner. (1983), Berlin Heidelberg: Springer.
24. Macosko, C.W., *Rheology. Principles, Measurements and Applications.* (1994), VCH, New York.
25. Somani, R.H., et al., *Shear-induced precursor structures in isotactic polypropylene melt by in-situ rheo-SAXS and rheo-WAXD studies.* Macromolecules, (2002), **35**(24): p. 9096-9104.
26. Philippe, A. M., et al., *Rheo-SAXS investigation of shear-thinning behaviour of very anisometric repulsive disc-like clay suspensions.* Journal of Physics-Condensed Matter, (2011), **23**(19): 194112.
27. Meins, T., et al., *New Insight to the Mechanism of the Shear-Induced Macroscopic Alignment of Diblock Copolymer Melts by a Unique and Newly Developed Rheo-SAXS Combination.* Macromolecules, (2012), **45**(1): p. 455-472.
28. Kume, T., et al., *Rheo-optical studies of shear-induced structures in semidilute polystyrene solutions.* Macromolecules, (1997), **30**(23): p. 7232-7236.
29. Van Puyvelde, P., et al., *Rheo-optical probing of relaxational phenomena in immiscible polymer blends.* Journal of Colloid and Interface Science, (1998), **200**(1): p. 86-94.
30. Yang, H., et al., *Rheo-optical investigation of immiscible polymer blends.* Polymer, (1998), **39**(23): p. 5731-5737.
31. Eberle, A.P.R. and L. Porcar, *Flow-SANS and Rheo-SANS applied to soft matter.* Current Opinion in Colloid & Interface Science, (2012), **17**(1): p. 33-43.
32. Andriano, L.T., et al., *Microstructural characterization of a star-linear polymer blend under shear flow by using rheo-SANS.* Journal of Rheology, (2020), **64**(3): p. 663-672.
33. Mykhaylyk, O.O., et al., *Applications of shear-induced polarized light imaging (SIPLI) technique for mechano-optical rheology of polymers and soft matter materials.* Journal of Polymer Science Part B-Polymer Physics, (2016), **54**(21): p. 2151-2170.
34. Prevedel, R., et al., *Brillouin microscopy: an emerging tool for mechanobiology.* Nature Methods, (2019), **16**(10): p. 969-977.
35. Palombo, F. and D. Fioretto, *Brillouin Light Scattering: Applications in Biomedical Sciences.* Chemical Reviews, (2019), **119**(13): p. 7833-7847.
36. JRS Scientific Instruments, M., Switzerland, *High contrast tandem Fabry-Perot interferometer TFP-2HC*. Operator Manual, ed. J. Sandercock.
37. Anton Paar, *MCR, Application-specific Accessoires for structure analysis.* Brochure.
38. Anton Paar, *Abbemat HP/WR/HT/MW automatic refractometer.* Instruction Manual.
39. Sandercock, J.R., *Structure in the Brillouin Spectra of Thin Films.* Physical Review Letters, (1972), **29**(26): p. 1735-1738.
40. Sandercock, J. R., *Some recent applications of Brillouin scattering in solid state physics*, in *Festkörperprobleme 15: Plenary Lectures of the Divisions "Semiconductor Physics", "Low Temperature Physics", "Metal Physics" of the German Physical Society Münster* (1975), H.J. Queisser, Editor. 1975, Springer Berlin Heidelberg: Berlin, Heidelberg. p. 183-202.
41. Sandercock, J.R., *Some recent developments in Brillouin-Scattering.* Rca Review, (1975). **36**(1): p. 89-107.
42. Lindsay, S.M., M.W. Anderson, and J. Sandercock, *Construction and alignment of a high performance multipass vernier tandem Fabry-Perot interferometer.* Rev. Sci. Instrum, (1981), **52**(10): p. 1478-1486.

43. Sandercock, J.R., *Trends in Brillouin-Scattering studies of opaque materials, supported films and central modes.* Topics in Applied Physics, (1982), **51**: p. 173-206.
44. Mock, R., B. Hillebrands, and R. Sandercock, *Construction and performance of a Brillouin-Scattering set-up using a triple-pass tandem Fabry-Perot interferometer.* Journal of Physics E-Scientific Instruments, (1987), **20**(6): p. 656-659.
45. Eichler H. J., Eichler Jürgen, Lux Oliver, *Lasers Basics, Advances and Applications. Springer,* (2018), Band **220**.
46. Eichler J., Eichler H. J., *Laser Bauformen, Strahlführung, Anwendungen. Springer.* Vol. **7**, *(*2010).
47. Tao Li, et al., *Analysis and design of imaging Fabry-Perot interferometers for measurement of Rayleigh-Brillouin scattering spectra in gas flows. Proc. SPIE* ***8910***, International Symposium on Photoelectronic Detection and Imaging Spectrometer Technologies and Applications, (2013), 89101E.
48. Ranade, J.D., *Part I. Applications of the Fabry-Perot interferometer for high resolution studies. Part II. Hyperfine structure in Bromine.* PHD thesis, University of London. 1950.
49. Kaminow I. P., *A Tunable Vernier Fiber Fabry-Perot Filter for FDM Demultiplexing and Detection.* IEEE Technology Letters Vol **1**, Issue 1, (1989), p.24-26.
50. JRS Scientific Instruments - The table stable; Mettmenstetten, S., *Brillouin Scattering by means of the JRS TFP-1 tandem multi-pass Fabry-Pérot interferometer.* Instruction maual.
51. Akitoshi K., S.S., *Note: Higher resolution Brillouin spectroscopy by offset stabilization of a tandem Fabry-Pérot interferometer.* Review of scientific instruments, (2011), **82**(12), 126103.
52. JRS Scientific Instruments - The table stable; Mettmenstetten, S., *Manual, contrast in the new TFP-2 HC.*
53. Hecht, E. P., *Schaum`s outline of theory and problems of optics.* Schaum's outline series, McGraw-Hill, (1976), **535**, 74-32228
54. Chipman R. A., W.-S.T.L., and Garam Young, *Polarized Light and Optical Systems*. (2019), CRC Press, Taylor & Francis Group.
55. Bass M., et al., Optical society of America, McGraw-Hill. *Handbook of optics*. **3** ed. Vol. I-V, (2010).
56. JRS Scientific Instruments - The table stable; Mettmenstetten, S., *Manual, TFP I.*
57. Coherent, *Operator's Manual Verdi G-Series.*
58. Coherent, *Datasheet, Verdi G-Series.*
59. Chilla J. L. A., et al., *High-power optically pumped semiconductor lasers.* SPIE Proceedings Volume **5332**, Solid State Lasers XIII: Technology and Devices, (2004).
60. Coherent, *Datasheet, Verdi G SLM-Series, High-Power Optically Pumped Semiconductor Lasers (OPSL).*
61. Coherent, *Advances in Laser Diode and OPSL Technologies Render Ion and Metal Vapor Lasers Obsolete.* (www.*content.coherent.com/legacy-assets/pdf/Advances-in-Laser-Diode-and-OPSL-Technologies.pdf)* -White paper. (**408**) 764-4983
62. Coherent, *Optically Pumped Semiconductor Lasers.* Brochure.
63. JRS Scientific Instruments - The table stable; Mettmenstetten, S., *Manual, alignment of optics.*
64. JRS Scientific Instruments - The table stable; Mettmenstetten, S., *Manual, alignment and calibration of a suitable light source.*

65. JRS Scientific Instruments - The table stable; Mettmenstetten, S., *Manual, alignment of reference beam.*
66. JRS Scientific Instruments - The table stable; Mettmenstetten, S., *Manual, calibration of mirrors in the TFP-HC2.*
67. JRS Scientific Instruments - The table stable; Mettmenstetten, S., *Manual, Ghost version 6.75.*
68. JRS Scientific Instruments - The table stable; Mettmenstetten, S., *Manual, Ghost software version 7.*
69. Origin Lab Coorporation, USA. *Tutorials for Origin 8.5 SR0*. Instruction Manual (2010).
70. Anton Paar, *Temperature Control for MCR Rheometers.* Brochure.
71. Kane, K.I.W., et al., *Determination of the rheological properties of Matrigel for optimum seeding conditions in microfluidic cell cultures.* AIP Advances, (2018), **8**(12).
72. Honorato-Rios, C., et al., *Fractionation of cellulose nanocrystals: enhancing liquid crystal ordering without promoting gelation.* NPG Asia Materials, (2018), **10**(5): p. 455-465.
73. Steffe J. F., Ph.D., P.E., *Rheological Methods in Food Process Engineering,* Second Edition. Freeman Press. (1992), **96**-83538
74. Macosko, C.W., *Rheology. Principles, Measurements, and Applications*. Willey VCH. (1994).
75. Deshpande A. P., J.M.K., P. B. Sunil Kumar, *Rheology of Complex Fluids*. Springer, (2010).
76. Malkin A. Y., A.I.I., *Rheology Concepts, Methods, and Applications*, (2017).
77. Larson, R., *The Structure and Rheology of Complex Fluids*. Oxford University press, (1999).
78. Shenoy A. V., *Rheology Of Filled Polymer Systems.* Springer Science+Buisness Media B.V., (1999), **XII**, 476
79. Schramm, G., *A Practical Approach to Rheology and Rheometry*. Vol. **2**nd. Gebrueder Haake GmbH, (2000).
80. Malkin, A.Y., *Rheology Fundamentals*. ChemTec Publishing, (1994).
81. Mezger, T.G., *The Rheology Handbook*, ed. 4th. Vincentz Network, (2014).
82. Giacomin, A.J., & Dealy, J. M., *Using large-amplitude oscillatory shear*, in *Rheological Measurement*. SpringerScience+Buisness Media Dordrecht, (1998), p. 327-356.
83. Jaeken, J.W. and S. Cottenier, *Solving the Christoffel equation: Phase and group velocities.* Computer Physics Communications, (2016), **207**: p. 445-451.
84. Liu, P., et al., *Lubricant shear thinning behavior correlated with variation of radius of gyration via molecular dynamics simulations.* J Chem Phys, (2017), **147**(8): p. 084904.
85. Ahmed, R.M., A.A. Ibrahiem, and E.A. El-Said, *Effect of Cobalt Chloride as Filler and PVP on the Optical Properties of PVA/PEG/PVP Blends.* Optics and Spectroscopy, (2020), **128**(5): p. 642-655.
86. Back, J.O., et al., *Parameter Screening of PVDF/PVP Multi-Channel Capillary Membranes.* Polymers (Basel), (2019), **11**(3).
87. Singh, P., et al., *Vibrational, thermal and ion transport properties of PVA-PVP-PEG-MeSO4Na based polymer blend electrolyte films.* Journal of Non-Crystalline Solids, (2018), **494**: p. 21-30.
88. Agool, I.R., K.J. Kadhim, and A. Hashim, *Fabrication of new nanocomposites: (PVA-PEG-PVP) blend-zirconium oxide nanoparticles) for humidity sensors.* International Journal of Plastics Technology, (2017), **21**(2): p. 397-403.

89. Wu, Y.-H.Y., Deng-Guang; Li, Hai-Peng; Wu, Xiang-Yang; Li, Xiao-Yan, *Medicated structural PVP/PEG composites fabricated using coaxial electrospinning.* e-Polymers, (2017), **17**(1): p. 39-44.
90. Hayat, M.D., et al., *Modification of PEG/PMMA binder by PVP for titanium metal injection moulding.* Powder Technology, (2017), **315**: p. 243-249.
91. Liu, M., et al., *PVP immobilized SiO2 nanospheres for high-performance shear thickening fluid.* Journal of Nanoparticle Research, (2017), **19**(7).
92. Song, G., et al., *Rheological Behavior of Tough PVP-in Situ-PAAm Hydrogels Physically Cross-Linked by Cooperative Hydrogen Bonding.* Macromolecules, (2016), **49**(21): p. 8265-8273.
93. Hayat, M.D., T. Li, and P. Cao, *Incorporation of PVP into PEG/PMMA based binder system to minimize void nucleation.* Materials & Design, (2015), **87**: p. 932-938.
94. Acosta, M., et al., *Effect of Polyvinylpyrrolidone Additions on the Rheology of Aqueous, Highly Loaded Alumina Suspensions.* Journal of the American Ceramic Society, (2013), **96**(5): p. 1372-1382.
95. Chao, Y.-C., et al., *Preparation and Application of PEG/PVP Copolymers.* Journal of Polymers and the Environment, (2012), **21**(1): p. 160-165.
96. Dhakal, T.R., et al., *Synergistic effect of PVP and PEG on the behavior of silver nanoparticle-polymer composites.* J Nanosci Nanotechnol, (2012), **12**(8): p. 6389-96.
97. Labuschagne, P.W., S.G. Kazarian, and R.E. Sadiku, *In situ FTIR spectroscopic study of the effect of CO2 sorption on H-bonding in PEG-PVP mixtures.* Spectrochim Acta A Mol Biomol Spectrosc, (2011), **78**(5): p. 1500-6.
98. Labuschagne, P.W., M.J. John, and R.E. Sadiku, *Investigation of the degree of homogeneity and hydrogen bonding in PEG/PVP blends prepared in supercritical CO2: Comparison with ethanol-cast blends and physical mixtures.* The Journal of Supercritical Fluids, (2010), **54**(1): p. 81-88.
99. Adichtchev, S.V., et al., *Brillouin spectroscopy of biorelevant fluids in relation to viscosity and solute concentration.* Phys Rev E, (2019), **99**(6-1): p. 062410.
100. Traverso, A.J., et al., *Dual Raman-Brillouin Microscope for Chemical and Mechanical Characterization and Imaging.* Analytical Chemistry, (2015), **87**(15): p. 7519-7523.
101. Bechekh, K. and N. Ghaouar, *Rheological Properties of Polyethylene Glycol (PEG 35000): An Interpretation of a Negative Intrinsic Viscosity and a High Huggins Coefficient Value.* Journal of Macromolecular Science, Part B, (2014), **53**(3): p. 391-397.
102. Singh U., *Peg 400.* Synlett, (2012), **23**(18): p. 2721-2722.
103. Cormier C.A. and M.N. Neuman, *Frequency stabilization of a Rayleigh-Brillouin spetrometer.* Review of Scientific Instruments, (1993), **64**(1): p. 91-94.
104. Young A.T., *Rayleigh scattering.* Physics Today, (1982), **35**(1): p. 42-48.
105. Raman, C.V., *The molecular scattering of light. Nobel Lecture Delivered at Stockholm,.* (1930).
106. Schaefer B., *Lehrbuch der Experimentalphysik*. **Vol. 1-7**. (2008), Walter de Gruyter.
107. Bahaa E. A. Saleh, M.C.T., *Fundamentals of Photonics* 3ed. (2019), Wiley.
108. Brüesch P., *Phonons: Theory and Experiments II*. (1986), Springer.
109. Kopitzki K., P.H., *Einführung in die Festkörperphysik*. **Vol. 5**. (2004), Teubner.
110. Baller J., *Untersuchungen zum intrinsischen Glasubergang.* Dissertation, Universität des Saarlandes, (2003).

111. Muanenda, Y., C.J. Oton, and F. Di Pasquale, *Application of Raman and Brillouin Scattering Phenomena in Distributed Optical Fiber Sensing.* Frontiers in Physics **7**, (2019).
112. Marx A., J.K.K., and H.-G. Unruh, *Brillouin Spectroscopy on Monodomains of Thin Polycrystalline Layers of Molecular Crystals.* Appl. Phys. A, **47**, (1988), p. 367-371
113. Müller, U., et al., *Acoustic profilometry of interphases in epoxy due to segregation and diffusion using Brillouin microscopy.* New Journal of Physics, (2008), **10**(2): p. 023031.
114. Krüger J. K., C.G., K. Stockem, R. Zietz, and M. Dettenmaier *Nonlinear elastic properties of solid polymers as revealed by Brillouin spectroscopy.* Colloid & Polymer Science, (1991).
115. Krüger, J. K., et al., *Simultaneous determination of elastic and optical properties of polymers by high performance Brillouin spectroscopy using different scattering geometries.* Colloid & Polymer Science, (1986), **264**(5): p. 403-414.
116. Jimenéz Riobóo R. J, J.K.K., K-P Bohn and C Fischer, *Surface-induced organization of n-alkanes on nanostructured PTFE: I. Brillouin spectroscopic investigations on pentacosane.* J.Physics: Condensed Matter **8**, (1996).
117. Jimenéz Riobóo R. J, E. Rodríguez-Cañas, and C. Prieto, *High Resolution Brillouin Spectroscopy and Determination of Elastic Properties of Ferroelectric and Piezoelectric Films.* Ferroelectrics, (2010), **272**(1): p. 93-98.
118. Jimenéz Riobóo R. J and M.A. Ramos, *Brillouin spectroscopy experiments on polymorphic ethanol.* Philosophical Magazine, (2007), **87**(3-5): p. 657-663.
119. Matsukawa, M., et al., *Brillouin scattering and ultrasonic study on an epoxy prepolymer.* Japanese Journal of Applied Physics, Part 1: Regular Papers and Short Notes and Review Papers, (1997), **36**(5 SUPPL. B): p. 2976-2980.
120. Kriegs, H., et al., *The effect of intramolecular relaxations on the damping of longitudinal and transverse phonons in polysiloxanes studied by Brillouin spectroscopy.* J Chem Phys, (2008), **128**(1): p. 014507.
121. Sanctuary R., R. B., Ulrich Müller, W Possart, P Alnot and J. Krüger, *Acoustic profilometry within polymers as performed by Brillouin microscopy.* J. Phys. D: Appl. Phys., (2003), **36**: p. 2738–2742.
122. Krüger, J. K., et al., *A new Brillouin scattering technique for the investigation of acoustic and opto-acoustic properties: Application to polymers.* Journal of Physics D: Applied Physics, (1998), **31**(15): p. 1913-1917.
123. Krüger, J. K., et al., *Spatial and angle distribution of internal stresses in nano- and microstructured chemical vapor deposited diamond as revealed by Brillouin spectroscopy.* Journal of Applied Physics, (2000), **87**(1): p. 74-77.
124. Krüger, J. K., et al., *Brillouin microscopy on microwave-induced phonons in LiNbO3.* New Journal of Physics, (2004), **6**: p. 57-57.
125. Krüger, J. K., et al., *A versatile method to characterize the mechanical and opticla properties of nano-and micro-structured CVD-diamond : Brillouin microscopy.* Vide-Science Technique Et Applications, (2001), **56**(300): p. 375-393.
126. Wolinski, W., et al., *Brillouin spectroscopy investigations of poly(ethylene glycol) water and organic solvent mixtures.* Laser Technology VIII: Applications of Lasers, (2006), Proc. of SPIE Vol. **6598**. 65980X-65980X-10.
127. Krüger, J. K., *Brillouin Spectroscopy and its Application to Polymers.* Optical Techniques to Characterize Polymer Systems, (1989), Elsevier. **5**: 429.

128. Ng, S.C., et al., *Determination of the Sol-Gel transition temperature abd phase diagram of a glation system by Brillouin SPectroscopy*. Journal of Physics E-Scientific Instruments, (1985), **18**(3): p. 250-252.
129. Fry, E., et al., *Temperature dependence of the Brillouin linewidth in water.* Journal of Modern Optics, (2010), **49**(3-4): p. 411-418.
130. Dil, J.G., *Brillouin-Scattering in condensed matter.* Reports on Progress in Physics, (1982), **45**(3): p. 285-334.
131. Figgins, R., *Inelastic light scattering in liquids: Brillouin scattering.* Contemporary Physics, (1971), **12**(3): p. 283-297.
132. Baller J., K., *Elastic properties of single-crystalline and consolidated nano-structured yttrium oxide at room temperature.* Journal of Physics Condensed Matter, (1999), **12**(25): 5403.
133. Krüger, J. K., *Brillouin Spectroscopy of oriented PMMA.* Polymer, (1982), **23**(1): 3-6.
134. Kruger J. K., L.P.a.M.P., *Brillouin scattering of semicrystalline poly(4-methyl-1-pentene): study of surface effects of bulk and film material.* Polymer, (1978), **19**(12): 1397-1404.
135. Demtröder, P.D.W., *Laser Spectroscopy 1, Basic Principles* 5ed. (2014), Springer.
136. Voigt, W., *Über die Beziehung zwischen den beiden Elastizitätskonstanten isotroper Körper.* Annalen der Physik, (1889), Vol. **274**, Issue 12: p. 573-587.
137. Still, T., *High frequency acoustics in colloid-based meso- and nanostructures by spontaneous Brillouin light scattering.* Dissertation, Springer Thesis, (2009).
138. Mattarelli, M., M. Vassalli, and S. Caponi, *Relevant Length Scales in Brillouin Imaging of Biomaterials: The Interplay between Phonons Propagation and Light Focalization.* ACS Photonics, (2020), **7**(9): p. 2319-2328.
139. Pochylski, M., *Structural relaxation in the wave-vector dependence of the longitudinal rigidity modulus.* Biomed Opt Express, (2019), **10**(4): p. 1957-1964.
140. Eichler, H.J. and J. Eichler, *Laser. Bauformen, Strahlführung, Anwendungen*. Springer Berlin, (2010).
141. Auld, B.A., *Acoustic fields and waves in solids*. New York: John Wiley (1973).
142. Bottani, C.E. and D. Fioretto, *Brillouin scattering of phonons in complex materials.* Advances in Physics: X, (2018), **3**(1): p. 1467281.
143. Chen, Z., L. Jiang, and H. Ma, *Calculation on frequency and temperature properties of birefringence of nematic liquid crystal 5CB in terahertz band.* Chemical Physics Letters, (2016), **645**: p. 205-209.
144. Patrício, P., et al., *Electro-rheology study of a series of liquid crystal cyanobiphenyls: experimental and theoretical treatment*. Liquid Crystals, (2012), Vol. **39**. Issue 1. 25-37.
145. Porter, D., et al., *Temperature dependence of droplet breakup in 8CB and 5CB liquid crystals.* Phys. Rev. E Stat. Nonlin. Soft Matter Phys., (2012), **85**(4 Pt 1): 041701.
146. Kim, J.H., et al., *Acoustic anisotropy in 5CB liquid crystal cells as determined by using Brillouin light scattering.* Journal of the Korean Physical Society, (2012), **61**(6): p. 862-866.
147. Osiński, B. L., *Thermal Characterization of MBBA, 5CB, and 8CB for Thermal Switches Using the 3ω Method.* Undergraduated Honors Thesis, University of New Mexico, (2011).
148. Skarp, K., Lagerwall, S. T., Stebler, B., *Measurements of Hydrodynamic Parameters for Nematic 5CB.* Molecular Crystals and Liquid Crystals, (2011), **60**(3): p. 215-236.
149. Roth, M., et al., *Viscoelastic rheology of colloid-liquid crystal composites.* J Chem Phys, (2010), **132**(12): p. 124702.

150. Ko, J.H., Y.H. Hwang, and J.H. Kim, *Sound propagation in 5CB liquid crystals homogeneously confined in a planar cell.* Journal of Information Display, (2009), **10**(2): p. 72-75.
151. Pan, R.-P., et al., *Temperature-dependent optical constants and birefringence of nematic liquid crystal 5CB in the terahertz frequency range.* Journal of Applied Physics, (2008), **103**(9): p. 093523.
152. Inn, Y.W. and M.M. Denn, *Rheology of a dispersion of low-molar-mass liquid crystal droplets in polydimethylsiloxane.* Journal of Rheology, (2005), **49**(4): p. 875-886.
153. Forest, M.G., Q. Wang, and R.H. Zhou, *The weak shear kinetic phase diagram for nematic polymers.* Rheologica Acta, (2004), **43**(1): p. 17-37.
154. Kempe, M.D., *Rheology and Dynamics of Side-Group Liquid Crystalline Polymers in Nematic Solvent.* PhD Thesis, California Institute of Technology, (2003).
155. Pan, R.-P., *Optical Constants of Two Typical Liquid Crystals 5CB and PCH5 in the THz Frequency Range.* Journal of Biological Physics, (2003), Vol **29**, 335-338.
156. Sperkach, Y.V., et al., *Temperature dependence of acoustical relaxation times involving the vicinity of N-I phase transition point in 5CB liquid crystal.* Molecular Crystals and Liquid Crystals, (2001), **366**: p. 2035-2054.
157. Negita, K., *Frequency dependence of the electrorheological effect in the nematic phase of pentyl cyanobiphenyl.* Liquid Crystals, (1999), **26**(3): p. 383-387.
158. Cui, M., Kelly, J. R., *Temperature Dependence of Visco-Elastic Properties of 5CB.* Molecular Crystals and Liquid Crystals Science and Technology. Section A. Molecular Crystals and Liquid Crystals, (1999), **331**(1): p. 49-57.
159. Soga, I., A. Dhinojwala, and S. Granick, *Direct measurement of fluid mechanical properties in micro space: Liquid crystal orientation under sheer.* Japanese Journal of Applied Physics Part 1-Regular Papers Short Notes & Review Papers, (1999), **38**(10): p. 6118-6122.
160. Pople, J.A. and G.R. Mitchell, *WAXS studies of global molecular orientation induced in nematic liquid crystals by simple shear flow.* Liquid Crystals, (1997), **23**(4): p. 467-473.
161. Mather, P.T., D.S. Pearson, and R.G. Larson, *Flow patterns and disclination-density measurements in sheared nematic liquid crystals .1. Flow-aligning 5CB.* Liquid Crystals, (1996), **20**(5): p. 527-538.
162. Mather, P.T., D.S. Pearson, and R.G. Larson, *Flow patterns and disclination-density measurements in sheared nematic liquid crystals .2. Tumbling 8CB.* Liquid Crystals, (1996), **20**(5): p. 539-546.
163. Hasegawa, M., K. Miyachi, and A. Fukuda, *Accuracy of nematic viscoelastic constant measurement using Rayleigh scattered-light.* Japanese Journal of Applied Physics Part 1-Regular Papers Short Notes & Review Papers, (1995), **34**(10): p. 5694-5699.
164. Gu, D.F. and A.M. Jamieson, *Shear deformation of homeotropic monodomains - temperature-dependence of stress-response for flow-aligning and tumbling nematics.* Journal of Rheology, (1994), **38**(3): p. 555-571.
165. Dolbashian C., et al., *Confinement of 5CB Between Lyotropic Bilayers.* Slippery Rock University, Pensilvania, (2013)
166. Sengupta A., *Topological Microfluidics Nematic Liquid Crystals and Nematic Colloids in Microfluidic Environment.* Springer Thesis book series, PhD Thesis, (2013).
167. Assanto G., *Nematicons Spatial Optical Solitons in Nematic Liquid Crystals.* IEEE Journal of Quantum Electronics, (2003), **39**(1): 13-21.

168. Pasechnik S. C., V.G.C., and Dina V. Shmeliova, *Liquid Crystals: Viscous and Elastic Properties.* Wiles-VCH **1**.ed, (2007).
169. Evangelista, G.B.L.R., *Adsorption phenomena and anchoring energy in nematic liquid crystals*. CRC Press, (2019).
170. Gao, Y., *Liquid Crystals Confined in Nanoporous Silica.* PhD Thesis, University of Tennessee, (2005).
171. Janossy I., *Optical effects in liquid crystals*. Perspectives in Condensed Matter Physics, PCMP, (1991), volume **5**. Springer Science+Business Media Dordrecht.
172. Vicari, L., *Optical Applications of Liquid Crystals*. Institute of Physics Publishing, (2003).
173. Scharf, T., *Polarized Light in Liquid Crystals and Polymers*, Hoboken, New Jersey: John Wiley & Sons, (2007).
174. Mather, P.T., D.S. Pearson, and W.R. Burghardt, *Structural response of nematic liquid crystals to weak transient shear flows.* Journal of Rheology, (1995), **39**(3): p. 627-648.
175. Kempe, M.D., et al., *Rheological study of structural transitions in triblock copolymers in a liquid crystal solvent.* Soft Matter, (2006), **2**(5): p. 422.
176. Castelletto, V., et al., *A SAXS study of flow alignment of thermotropic liquid crystal mixtures.* Liquid Crystals, (2009), **36**(4): p. 435-442.
177. Dong Feng Gu, et al., *Rheological Characterization of Director Dynamics in a Nematic Monodomain Containing Mesogenic Polymers of Differing Architectures.* Macromolecules, (1994), **27**, 2, 337-347.
178. Mather, P.T., et al., *Rheo-optical evidence of a flow-induced isotropic-nematic transition in a thermotropic liquid-crystalline polymer.* Macromolecules, (1997), **30**(25): p. 7977-7989.
179. Sperkach Y. V., V.S.S., Olexandr D. Aliokhin, Anatoly L. Strybulevych and M. Masuko, *Rheological Properties of Liquid Crystal 4-Pentyl 4'Xyanobiphenil.* Molecular Crystals and Liquid Crystals Science and Technology. Section A. Molecular Crystals and Liquid Crystals. (2001), Volume **366**, Issue 1, p.91-100.
180. Boudreau, W., Stein, *Conoscopic observations of shear induced rotations in liquid crystals.* Rheologica Acta (1999), **38**(6): 503-513
181. Karat, P.P. and N.V. Madhusudana, *Elastic and Optical Properties of Some 4′-n-Alkyl-4-Cyanobiphenyls.* Molecular Crystals and Liquid Crystals, (2007), **36**(1-2): p. 51-64.
182. Bailey, C., et al., *Rheological properties of bent-core liquid crystals.* Soft Matter, (2009), **5**(19): p. 3618.
183. Gahwiller, C., *Temperature Dependence of Flow Alignment in Nematic Liquid Crystals.* (1972), Phy.Rev.Lett. **28**, 1554.
184. Silva, B.F.B., et al., *Nematic Director Reorientation at Solid and Liquid Interfaces under Flow: SAXS Studies in a Microfluidic Device.* Langmuir, (2015), **31**(14): p. 4361-4371.